LOCATION OF SUB-FRESNEL SCALE MINERAL
TARGETS IN THE SUBSURFACE

LUCKY MOFFAT

LOCATION OF SUB-FRESNEL SCALE MINE-LIKE TARGETS IN THE SONICON GULF

by

© Emily Michel

A thesis submitted to the

School of Graduate Studies

in partial fulfillment of the

requirements for the degree of

Master of Science

Department of Earth Sciences, Faculty of Science
Memorial University of Newfoundland

January 11, 2012

St. John's

Newfoundland

LOCATION OF SUB-FRESNEL SCALE MINERAL TARGETS IN THE SUBSURFACE
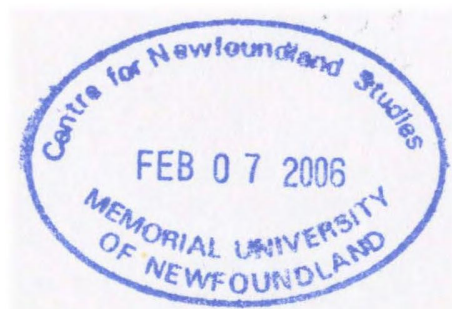
by

© Lucky Moffat

A thesis submitted to the

School of Graduate Studies

in partial fulfillment of the

requirements for the degree of

Master of Science

Department of Earth Sciences/ Faculty of Science
Memorial University of Newfoundland

January 7th, 2004

St. John's   Newfoundland

Abstract

With the decline of already discovered and exploited shallow mineral deposits, the mining industry is intent on finding new techniques that could explore deeper but still be cost-effective. One method that has been considered is the seismic reflection technique which has been very successful in the petroleum industry. This thesis examines one approach, *seismic beamforming*, which can be used in conjunction with the seismic reflection technique for the direct location of massive sulfide bodies. Implementation of the technique could prove successful in reducing exploration costs.

Beamforming can be used to extract a variety of information about a target (e.g. range, angle of emergence, temporal frequency content, power) from a propagating signal. This thesis studies the use of the angle of emergence of wavefronts propagating across a linear array of seismic receivers to assist in location of the wavefront source. The angles are back-projected to a common point which represents the point source or scatterer located at the far-field of the receiver array.

A simple conventional beamformer is designed and tested on data generated from four different geometries of a linear array of receivers and a single source of seismic energy. The intersection of back-projected rays is not tight enough for all four cases but on using a distance-weighting scheme the location of the scatterers is satisfactorily estimated. A number of performance measures are carried out on the beamformer to determine its effectiveness. The beamformer is tested on data subjected to different noise fields, on data decimated in the spatial domain and on data obtained from a geometry that includes the presence of two scatterers which are more than a Fresnel zone apart. The

results indicate that the beamformer is able to localize a scatterer when the data has a signal-to-noise ratio of at least 5 dB. The results also show that spatial decimation of the data has no adverse effect on location estimates. However, to achieve desired beam steering resolution, the data need to be interpolated with more spatial points in the beamformer. The beamformer is not able to distinguish between two scatterers in its vicinity when the source is at a point directly between them. But it is able to detect the two scatterers when the source is moved to a point on the other side of either scatterer.

One main issue that affects the reliability of location estimates is the way the angle of emergence is picked. The angles are handpicked and this has the potential of introducing bias in the estimates which could then affect the overall performance of the beamformer. A computer code can be written to automatically pick these angles. This would improve location estimates and may eliminate the need to use the distance-weighting scheme used in the investigations.

Overall, the results obtained show that if correctly implemented, seismic beamforming together with reflection seismic can serve as a cost-effective method for the location of mineral deposits.

Acknowledgements

First and foremost I would like to thank GOD for giving me the strength and ability to complete this work. I also wish to thank Dr. Charles Hurich first for suggesting the topic for this thesis and secondly for his guidance and support be it financial or otherwise. I appreciate the endless hours of discussions, technical or otherwise, that we had on this research work. These discussions have done a great deal in improving this thesis work.

My sincere gratitude goes to my other supervisor Dr. James Wright for his invaluable advice, help and suggestions. The effort he put in reviewing this thesis work is greatly appreciated. Without him accepting me as his student I would never have ended up at Memorial University.

I also want to thank the Earth Sciences department at Memorial University for introducing me to exploration seismology. The University of Botswana deserves credit for partly funding my studies at Memorial. Without them I would not have had the opportunity to attend graduate school.

Fellow graduate students Kebabonye Laletsang, Rich Wright, Chad Wheaton, Wes Hamlyn and Dave McCallum also deserve mention for their support and encouragement during good and bad times.

Finally, I would like to express my gratitude to my family particularly my mom Batshwana Tsuaneng and my two sisters Dithapelo Moffat and Moselwane Tsuaneng for their love, patience, affection and understanding. Their encouragement provided the most needed support I wanted for finishing my studies at Memorial University.

Table of Contents

List of Tables

List of Figures

List of Appendices

Chapter 1

Introduction

1.1 Application of Seismology in Mineral Exploration.

Seismic reflection techniques have been used extensively for oil and gas exploration in sedimentary basins. Through imaging, these techniques help pinpoint the location and size of oil and natural gas fields. The techniques rely on acoustic impedance contrasts across major lithologic boundaries. When seismic energy encounters such boundaries it is reflected and scattered back up to the surface where it is recorded and analyzed for information about the subsurface.

The possibility of adapting reflection seismic techniques to mineral exploration has recently been explored (Dahle *et al.*, 1985; Eaton *et al.*, 1996; Milkereit *et al.*, 1996; Salisbury *et al.*, 1996; Eaton, 1999 and Laletsang, 2001). This was sparked by the inability of the conventional surface geophysical techniques for mineral exploration, e.g., EM and potential fields methods, to resolve ore body sized targets at depths >500 m even though minerals can be economically recovered from such depths.

Results from the above references indicate that mineral deposits have characteristics that enable the use of seismic reflection techniques in their exploration. Salisbury *et al.* (1996) demonstrated that massive sulfide bodies have high acoustic impedances (ρv), where ρ is the density and v is the compressional velocity, compared to their host rocks. Their acoustic impedances provide good contrasts, a property that is

1

necessary for a body to produce a reflection, across rock boundaries. Milkereit *et al.* (1996) showed that indeed massive sulfides produce a characteristic seismic reflection response and the method could be used to image the deposits in a complex geologic setting. Long before their work, Dahle *et al.* (1985) had applied the technique to data collected in the ore fields of Sulitjelma and Løkken (Orkla), Norway in an attempt to detect known and unknown ore bodies. The ore bodies' ability to produce impedance contrasts across rock boundaries enabled their detection and location. Other research work that applied the seismic reflection method for ore prospecting includes the work of Wright *et al.* (1994) and Eaton (1999). Wright *et al.* (1994) focused on the use of small explosive sources to cut exploration costs and to better seismic resolution. Eaton's (1999) work demonstrated that massive sulfide ore bodies could potentially be recognized and mapped using seismic methods based on their scattering response.

Several approaches can be used in conjunction with the seismic reflection technique to detect and locate mineral deposits. One that is the focus of this thesis, which is extensively used in Sonar and Radar applications, is called *beamforming*. A detailed description of the technique is presented in chapter 3.

1.2 Thesis Objective

The primary focus of this research is to investigate the application of seismic beamforming for exploring for mineral deposits in a cost-effective manner. Beamforming involves the introduction of relative time delays or phase shifts between receivers in an array so that wavefronts from a target appear to arrive simultaneously at the array. The

delays introduced depend on the medium velocity, the separation between the receivers and the orientation of the wavefront. Since the delays introduced are directly related to the direction of propagation of the wavefronts, it is possible to determine the angles of incidence between a line perpendicular to the axis of the array and the wavefront. These angles can then be used in the determination of the location of a target.

Mineral deposits present a tough challenge to seismic exploration. They are generally small (~1-30m thick) and usually have complex geometries and they are often found in a steeply dipping setting. Because of these challenges, exploring for them is difficult and often the costs and risks are high. The cost of a full 3-D seismic survey, for instance, is described in White, (1999) as $50-100k per sq. km and requires a large number of receivers and sources to conduct. Currently exploration for mineral deposits using the reflection seismic method involves directly detecting or imaging them. Detection describes a situation where a seismic response of a deposit is used to infer the presence of the deposit whereas imaging characterizes the deposit, i.e., produces a picture of the geometrical distribution of the reflecting surfaces of the deposit (Robinson and Treitel, 1980). To reduce costs and risks in locating a deposit, detection without imaging may be a desirable option. Given that source effort occupies much of the seismic acquisition budget (30-45%) (private correspondence with Dr. Jim Wright, December 2002), and that production from shallower known deposits already exploited is gradually declining, most companies are seeking a cost-effective method to explore for deeper targets. The mining industry is often focused on drilling targets rather than imaging them, which places emphasis on the need to design methods that will tailor acquisition

3

techniques for detection of these deposits. This thesis proposes one method for an exploration tool to detect deep-seated massive sulfide zones.

The objective of this research can be subdivided into two parts;

1. To explore and assess the possibility of detecting a massive sulfide deposit by illuminating it with a limited number of shots and beamforming using a receiver array. It should be noted that this only involves detecting and not imaging the deposit.

2. To identify procedures in the method that need refining so as to produce accurate and reliable estimates of the parameters of the target (e.g., location in three dimensions).

In order to achieve the objective of this study, a systematic approach was adopted. The following steps were taken to carry out the study:

(a) Software algorithms were developed, using MATLAB®, to carry out the beamforming procedure which was used to provide target parameters such as direction of arrival of the wavefronts and relative scattering power.

(b) Synthetic seismic data were then generated using a finite-difference approach to solve the scalar wave equation.

(c) The results were analyzed and discussed.

(d) Suggestions for refinements and improvements in the approach as well as recommendations for future work are made.

1.3 Literature Review

Most of the literature in exploration seismology focuses on oil and gas exploration (Sheriff and Geldart, 1995; Yilmaz, 2001) as mentioned in section 1.1. The research referenced in that section involved attempts to image the ore deposits. The main focus of this thesis is not in imaging of the deposits but in detecting their presence and their location. A lower cost survey technique that could detect and locate potential deposits could prove to be an attractive alternative. Since I am only concerned with detecting and locating the massive sulfide deposits, one method that could be used for that purpose is beamforming. Beamforming is widely used in SONAR and RADAR signal processing. Van Veen and Buckley (1988) give a very good introduction to this technique and explain that it is a form of spatial filtering that can be used to estimate the direction of arrival of a signal in the presence of noise and interfering signals. Advancement in technology has led to improved and more robust algorithms. Treatment of the conventional beamforming approach is covered in Johnson (1982), Dudgeon and Mersereau (1984), Mucci (1984), Maranda (1989), Nielsen (1991), Johnson and Dudgeon (1993).

There are a limited number of publications in the geophysical literature that pertain to the application of beamforming to mineral exploration. One of a few papers found, Moran and Albert (1996), uses direct transmitted surface seismic waves to locate a military target. Even though these waves have different propagation characteristics compared to reflected ones (body waves), they are subject to somewhat similar noise

fields. Thus, beamforming procedures for them are almost the same as for reflected waves.

Most literature in beamforming covers the general aspects of the method. Less attention is paid to simulation and implementation. This is mainly due to the fact that company patents restrict the publication of new implementation and simulation of beamforming techniques (Hampson, 1997). Hampson (1997) is one of a few available sources that deal with simulation and implementation. His work is based on an introductory chapter that appears in Nielsen (1991). Hampson (1997) uses MATLAB® for implementation of the algorithms.

This thesis describes an implementation procedure that can be used for locating mineral deposits using a conventional beamforming technique.

1.4 Overview of the thesis

This thesis involves the application of one signal processing technique known as beamforming in the location of deposits whose size or width is comparable to or smaller than the diameter of the first Fresnel zone (see section 2.1 for definition of the Fresnel zone). The beamforming process attempts to find the direction of arrival of diffraction wavefronts deposits produce when illuminated with seismic energy. Finding the direction of these wavefronts localizes the scatterers.

Chapter 2 introduces the array model which is central to the background information developed in chapter 3. The array model developed assumes that the host medium and the deposit are both homogenous and isotropic. This is necessary in that a

simple waveform can be developed which only considers the changes in phase of the wavefronts as they propagate across the array.

Chapter 3 presents the theoretical background to the conventional beamforming technique used in this thesis. This technique is known as the *weighted delay-and-sum method*. Rather than attempt to employ one of the more robust approaches in beamforming, I felt it was useful to test the idea using basic theory as no paper in the geophysics literature has attempted to apply this method to reflection seismic data. The weighted delay-and-sum beamformer output is formed by averaging the weighted and delayed versions of the receiver outputs. The delays are chosen in a way that will maximize the wavefronts coming from a particular direction. The directions obtained essentially localize the scatterer responsible for the creation of those wavefronts.

In chapter 4, the theory presented in chapter 3 is used. The theory is applied to synthetic data obtained using a uniform linear array. The performance of the method is evaluated. The results obtained show that beamforming can be an effective method to use for the location of scatterers.

Finally, chapter 5 contains conclusions and implications of what have been achieved in this thesis.

Chapter 2

The Array Model

This chapter establishes a model for the output signal of the *receiving seismic array* that will be used in this thesis. The receiving seismic array consists of geophones or receivers spaced at equal intervals along a seismic line. For a vertically traveling wave that propagates across the array, the outputs from the individual geophones combine constructively when added together. Destructive interference occurs for horizontal waves that propagate across the array since they arrive at each geophone at different times. Thus, the array can be used to discriminate against waves coming from different directions. We will exploit this characteristic in chapter 3.

This chapter begins by presenting assumptions (section 2.1) that are helpful in developing a simplified model equation. A simplified equation enables us to consider only the propagation delays among the receivers and not account for amplitude variations. Section 2.2 gives a development of the waveform model. The waveform model is designed for a single scatterer; the general model for multiple scatterers can be obtained using the linear superposition principle (Stoica and Moses, 1997).

Following the development of the waveform model, the chapter discusses certain requirements (section 2.3) that are necessary for proper sampling of the wavefield. To avoid temporal aliasing the sampling frequency should be at least twice the highest frequency in the data. Similarly, spatial aliasing can be avoided if the spacing between the receivers is set to less than or equal to half the wavelength of the signal.

2.1 Assumptions

This section describes the assumptions that are made in the development of a model for the beamforming process discussed in chapter 3.

(a) The array geometry is linear (i.e., 1-D array).

(b) The array consists of identical omnidirectional transducers uniformly distributed and situated in the same plane as the scatterers (fig 2.1). The scatterers behave like point sources.

(c) The host medium and the deposit are homogenous and isotropic.

(d) The deposit or scatterer at a given depth is assumed to be situated in the far-field. This will fully be explained later in this section.
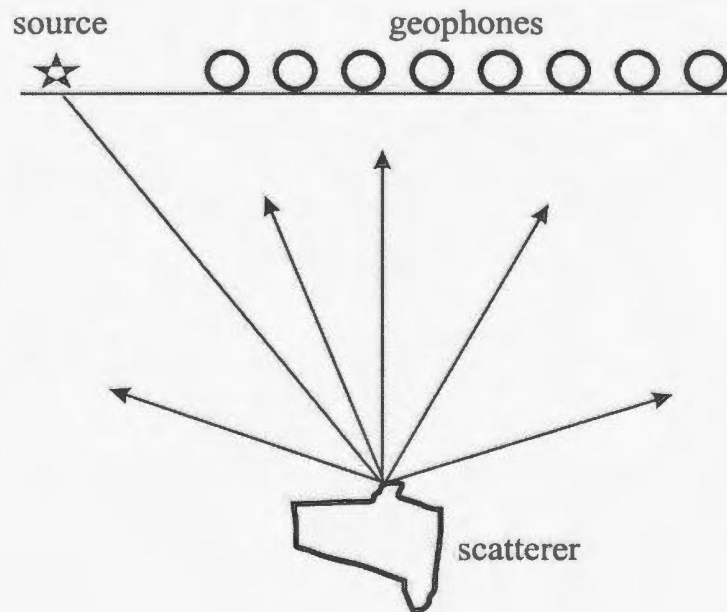
Figure 2.1
Energy radiated or scattered by a massive sulfide body in the subsurface is picked up by a uniform linear array on the earth's surface.

Assumption (c) implies that the propagation medium is not dispersive, and since the deposit is in the far-field we can view the waves arriving at the array as planar. Under

the above assumptions the only parameter that characterizes the scatterer's location is the angle of arrival of the wavefronts emanating from it. It should be noted that the above assumptions could be relaxed but that would significantly complicate the array model. For instance, instead of using a linear array a rectangular array could be used. The rectangular array is a natural extension of the linear array and it has elements lying in the xy-plane. This means instead of just looking for a single incidence angle, both azimuthal and elevation angles are required to characterize the target. If the scatterer is in the near-field, its position would be defined by azimuth, elevation and range.

The array processing method discussed in the coming sections requires plane wave propagation. However, the scatterers described above behave more like point sources since their size is comparable to or smaller than the width of the *Fresnel zone*. The Fresnel zone is the area from which reflected energy arriving at a detector has phases differing by no more than a half-cycle (Sheriff and Geldart, 1995). Since the geophones are in the *near-field* of scatterers, they receive spherical wavefronts. The near-field region (figure 2.2) describes the region of space for which $z < \dfrac{2L^2}{\lambda} = \dfrac{2fL^2}{v}$, where z is the depth of the scatterer from the receiver array, L is the largest dimension of the array, f is the frequency, v is the propagation velocity and λ is the wavelength. This region is also called the Fresnel region (Arnold, 1997). In this region spherical wavefronts dominate. The other radiation region, known as the *far-field* (or Fraunhofer region), is the region of space where the depth of the scatterer from the receiver array is $\geq \dfrac{2L^2}{\lambda}$. This region is dominated by planar wavefronts.

10
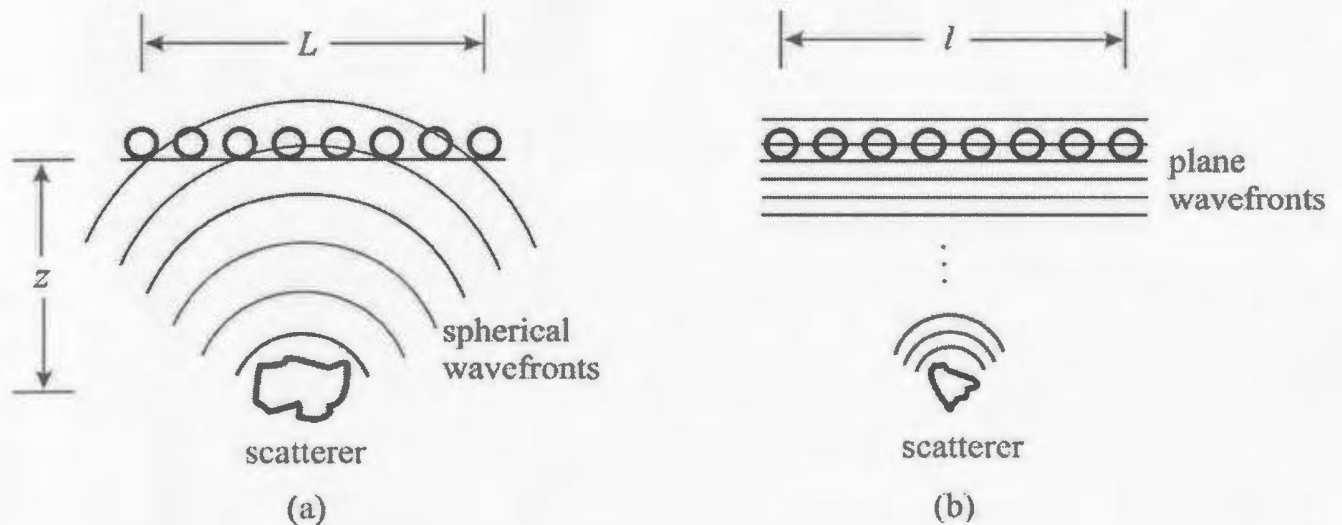
Figure 2.2
Schematic showing types of radiation of energy: (a) the near-field region and (b) the far-field region. A distinction is made between L and l, L represents the aperture of the array whereas l represents a segment of the array.

As an example, assume a wavefront propagates across a uniform linear array of 5 receivers with 20 m spacing, a total length L of 80 m. If the medium velocity is 2000 m/s and the frequency of the wave is 25 Hz, then far-field radiation would be satisfied by a target at a depth of at least 160 m. If the medium velocity is 4000 m/s instead of 2000 m/s, then the far-field radiation would begin at an 80 m depth. If we now consider a different wave with 50 Hz frequency traveling through the same media as the one above we find that for a 2000 m/s propagation velocity the far-field radiation begins at 320 m depth and at 160 m depth if the velocity of the medium is 4000 m/s. The whole scenario is illustrated in figure 2.3 for five different waves that propagate across two arrays of different lengths. As can be seen, the far-field boundary is dictated by the size of the array and the wavelength of the propagating wavefront.

The illustration given in figure 2.3 indicates that normally seismic exploration is conducted in the near-field radiation region. Thus, to satisfy the plane wave condition in

11
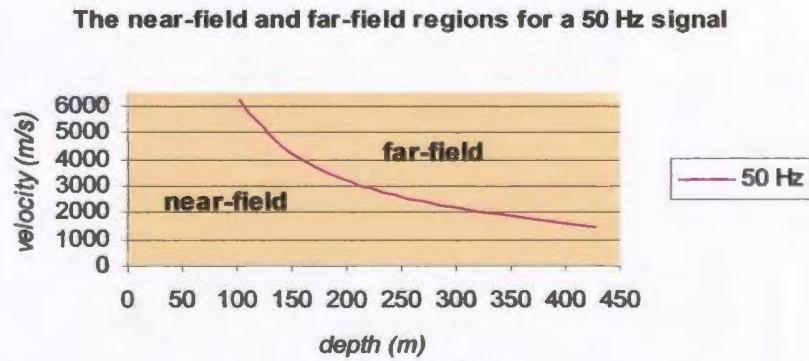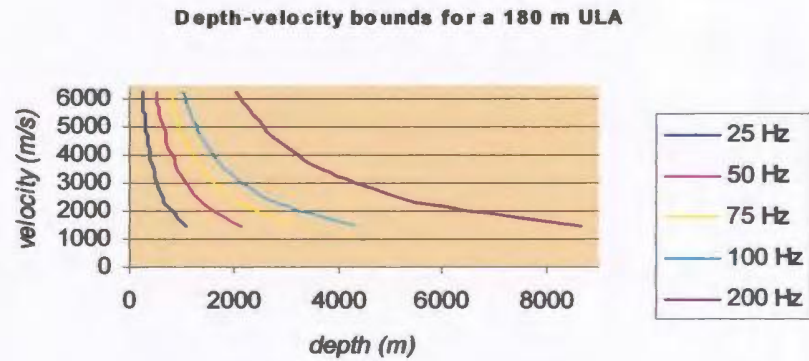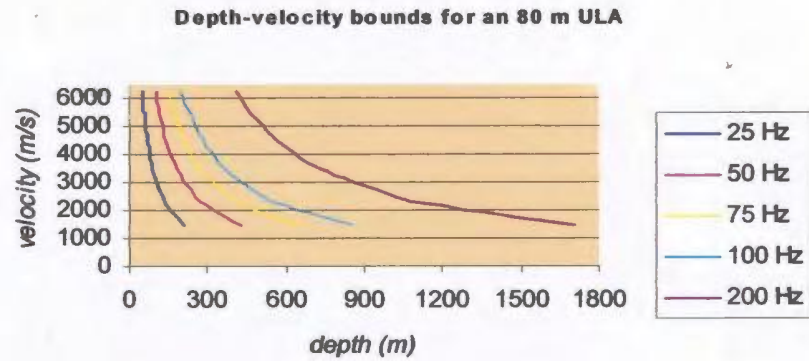
Figure 2.3
Schematic showing depth-velocity bounds for near-field and far-field radiations for two uniform linear arrays (ULA's) of length (a) 80 m and (b) 180 m with 20 m receiver spacing. The diagram in (c) marks the near-field and far-field regions for the uniform linear array in (a) when the dominant frequency is 50 Hz.

these circumstances, the data recorded by the array should be segmented in such a way

that curvature within each segment is negligible, i.e., the condition $z > \dfrac{2l^2}{\lambda}$ is satisfied,

where l, a fraction of L, is the length of each segment. For instance, if we want to detect a

target at a depth of 500 m given a velocity of 4000 m/s and a frequency of 50 Hz, we

need l to be less than 141 m which is about 7 receivers if the receiver spacing is kept at

20 m. If the wave has a frequency of 100Hz and other parameters are the same as used

for a target at 500 m, then the maximum number of receivers that would define each

segment is 5 (i.e., l should be less than 100 m). For a 200Hz wave with the same

parameters, 3 receivers would be required.

2.2 The Waveform

We begin by developing a model for a single plane wave signal that impinges on the

array from the broadside. The general model which involves more than one source (or

scatterer) can be obtained using the superposition principle (Stoica and Moses, 1997). As

we have indicated earlier, the receivers are identical and have the same impulse response.

Thus, the constant responses can be thought to be contained in the signal term $s(t)$. The

output from the mth receiver can then be represented as:

$$x_m(t) = s(t - \tau_m) + n_m(t),$$ (2)

where τ_m is the time delay and n_m the background noise field at each receiver. It should

be noted that τ_m is also a function of apparent wavenumber $k_0 = \omega a_0$ (where ω is the

temporal frequency and a_0 is the apparent slowness vector $(1/v)$), which is directly related

to the angle of propagation φ. The relationship between wavenumber vector k_0 and φ is illustrated in figure 2.4 below. Either one of these two quantities can be used to describe the direction of a plane wave as it reaches the geophone array. The notation describing
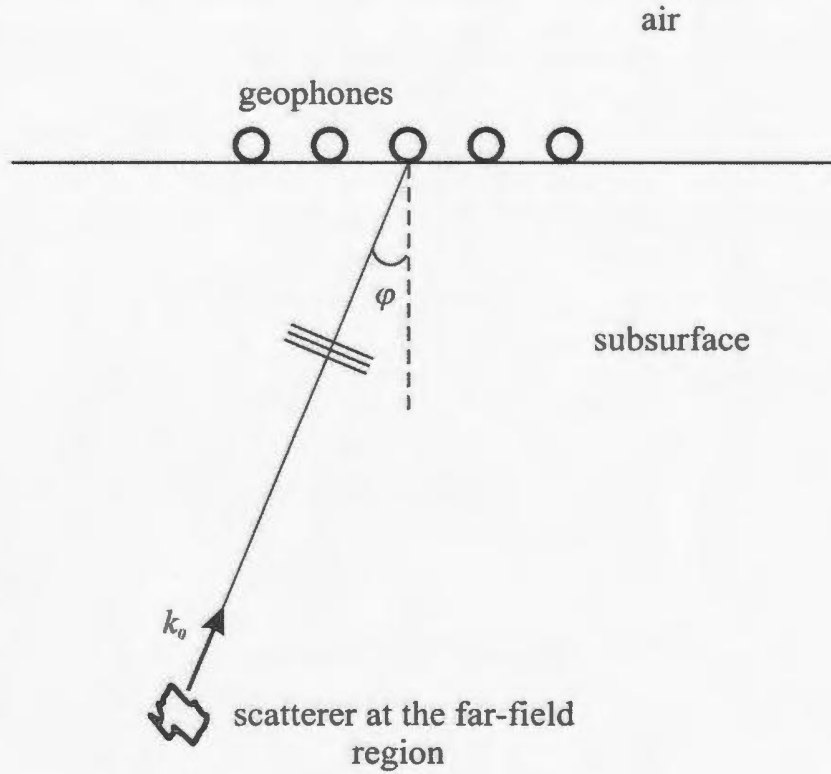
Figure 2.4
Illustration of the relationship between k_0 and φ. The two quantities describe the direction of approach of a plane wave emitted by a scatterer in the far-field. Thus, either one provide a means of locating the scatterer.

the time delays among the receivers can be made simpler by setting the delay at the first receiver to be zero, i.e. $\tau_0 = 0$ (figure 2.5), such that delays at the remaining receivers

$$\tau_0 = 0 \qquad \tau_1 = \frac{d \sin \varphi}{v} \qquad \tau_2 = \frac{2d \sin \varphi}{v} \qquad \cdots \qquad \tau_{M-1} = \frac{(M-1)\,d \sin \varphi}{v}$$

Figure 2.5
Explanation of how the delays among the receivers are set with respect to the first receiver.

would simply be propagation delays with respect to the first receiver.

In the frequency domain, equation 2 can be expressed as

$$X_m(f) = S(f)e^{-j\omega\tau_m} + N_m(f), \tag{3}$$

where $S(f)$ is the ideal Fourier transform of the signal without noise. If the bandwidth of the signal $S(f)$ is small compared to its dominant frequency, i.e. if the signal is narrowband, then the propagation delays between receiver elements can be approximated with a phase shift. This allows us to write equation 3 as

$$X_m(f) = S(f)e^{-j2\pi f_D \tau_m} + N_m(f), \tag{4}$$

where f_D is the dominant frequency of the signal. As stated above in section 2.1 the receivers in the array are the same and thus have an equal, omnidirectional response at the dominant frequency. Thus the constant receiver responses are deemed to be contained in the signal term $S(f)$.

If the signal does not satisfy the narrowband assumption (i.e., if it is broadband), the situation always encountered in seismic exploration, it can be decomposed into multiple narrowband signals and each frequency can then be processed separately. This allows the delays to be approximated with a phase shift for each frequency as in the narrowband case (van Trees, 2002).

Since data from the receivers is digitized, a discrete time version of equation 2 is employed. It is obtained by sampling the inverse Fourier transform of equation 4.

$$x_m(n) = s(n)e^{-j2\pi f_D \tau_m} + n_m(n). \tag{5}$$

Equation 5 is the array signal model that we will use throughout this thesis.

Now let us look at the exponent term in equation 5. We call this term a_m and write it again for illustrative purposes.

$$a_m(\varphi) = \begin{bmatrix} 1 \\ e^{-j2\pi f_D \tau_1(\varphi)} \\ \vdots \\ e^{-j2\pi f_D \tau_{M-1}(\varphi)} \end{bmatrix}. \tag{6}$$

This term is referred to as the array response function (Manolakis *et al.*, 2000). It shows us how the array will respond to incoming signals. As can be seen the array response function is dependent on the angle φ which is the direction of arrival of the signal impinging on the array. For the case of a uniform linear array (ULA) where the receivers are in a line with equal spacing, denoted by d, and where the first receiver is chosen as the reference point, the propagation path between the first receiver and any receiver in the array (see figure 2.6a) results in a time delay of

$$\tau_m(\varphi) = \frac{md\sin(\varphi)}{v}, \qquad \text{for } \varphi \in [\text{-}90^\circ, 90^\circ], \tag{7}$$

where v is the propagation velocity. φ is measured clockwise with respect to the normal of the linear array as shown in figure 2.4 above and figure 2.6 (b) below. φ is restricted to this interval because in the case of this type of array, and where the media of propagation on both sides of the array are the same, a wavefront coming from the south and another symmetrically opposite from the north, as depicted in figure 2.6 (b), yield identical sets of delays (i.e., $\tau_m(\varphi) = \tau_m(\pi\text{-}\varphi)$) and hence are indistinguishable.

2.3 Sampling the wavefield

In order to avoid loss of information from incoming wavefronts certain conditions should be met. To avoid temporal aliasing the temporal sampling frequency should be twice the highest frequency in the signal (Yilmaz, 2001). Since the uniform array samples the incoming wavefronts at discrete spatial locations, the spatial frequency k_s (or precisely the inverse of receiver spacing) should be high enough to avoid spatial aliasing. The spatial frequency is normally set at $k_s \geq 1/d$. To satisfy this spatial condition the sampling interval

(a)   (b)
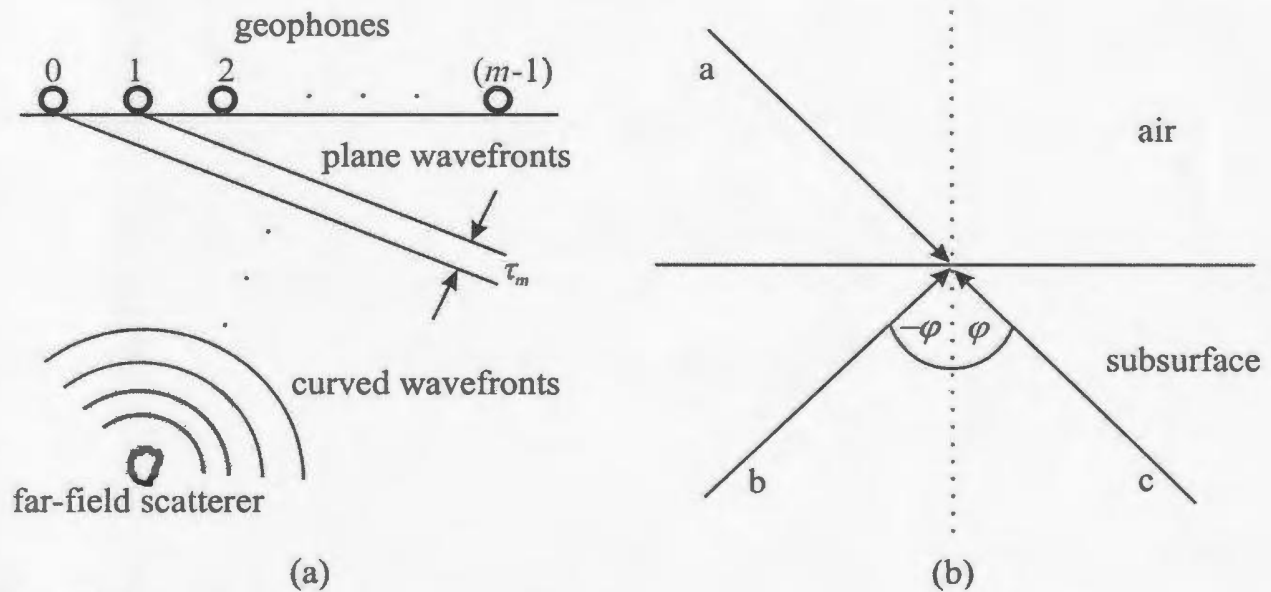
Figure 2.6
(a) *Plane wavefronts arriving from a far-field source into a uniform linear array.* (b) *North-south ambiguity of a uniform linear array. Signal **a** is indistinguishable from signal **b**. But **c** can be distinguished from **b**.*

d is chosen such that it is less than or equal to half the wavelength ($d \leq \lambda/2$) of the waveform propagating past the array. As an example, assume the following set of design parameters: the sample rate $\Delta t = 0.5$ ms, the highest frequency of the propagating waveform is 100Hz, the propagation velocity $v = 4000$m/s and the dominant frequency of

the signal $f_D = 50$Hz. Given this scenario, no temporal or spatial aliasing would occur provided the receiver spacing is equal to or less than 20m.

2.4 Summary

In this chapter we discussed the development of an array model that we will be using in later chapters. We stated the assumptions that are necessary to develop a simplified signal model. The scatterers are assumed to be smaller than the Fresnel zone. As long as it is assumed that the receivers have equal omnidirectional response at the same frequencies and that both the scatterer and the host medium are homogeneous and isotropic, the simplified waveform model in §2.2 can be adopted.

Section 2.2 of the chapter dealt with the development of the waveform model. It starts with the continuous time output waveform from each receiver and transforms it into the frequency domain. Since in practice we work with discrete data, a discrete version of the same waveform is derived.

Finally, the last section of the chapter discusses requirements needed when sampling the wavefield. To avoid temporal aliasing, the temporal sampling frequency should be at least twice the highest frequency in the signal. Similarly, spatial aliasing is avoided when the spatial sampling is high enough ($k_s \geq 1/d$).

Equipped with this information we now briefly introduce the signal processing method that will help us estimate the angles of arrival that appear in equation 7.

Chapter 3

Conventional Beamforming

In this chapter, we present the conventional beamforming technique (section 3.1) used in this study. The chapter examines the response of an array of receivers to signals coming from a particular direction. The beamforming process can be performed in both the time (section 3.1.1) and frequency domains (section 3.1.2). This chapter also discusses the use of the array to determine the angle of emergence of propagating wavefronts. This process is known as array steering; it is covered in section 3.1.3. There are some practical limitations on the choice of parameters used in the determination of angles of emergence of these propagating waves. These are discussed in sections 3.1.4 and 3.1.5. Section 3.2 presents the computer code used in the implementation of the beamforming process discussed in this chapter.

3.1 Theoretical background

3.1.1 The time domain approach

Propagating signals detected by the array may arrive at any angle with respect to the aperture of the array. The receiver outputs obtained from the signals that arrive at $0°$ are in phase and will add up coherently when summed together. Wavefronts arriving from any other angle other than $0°$ are out of phase and thus the receiver outputs will not add coherently when summed together. To determine the angle from which a wave arrives at the array, the receiver outputs are weighted and delayed before summing. The angle of

arrival is identified by a systematic search for the angle that results in the highest power across the array. In essence, this search focuses the array in the direction from which the wavefronts came. This operation, known as weighted delay-and-sum method, is one of the oldest conventional beamforming methods which is also easy to understand. This method is the one in which signal processing algorithms in this research are based upon.

One way to ensure that receiver outputs add up coherently when summed is to apply appropriate time delays at each receiver output and then add. The output will be maximal and appear as though the signals arrived in phase perpendicular to the array's aperture (figure 3.1).
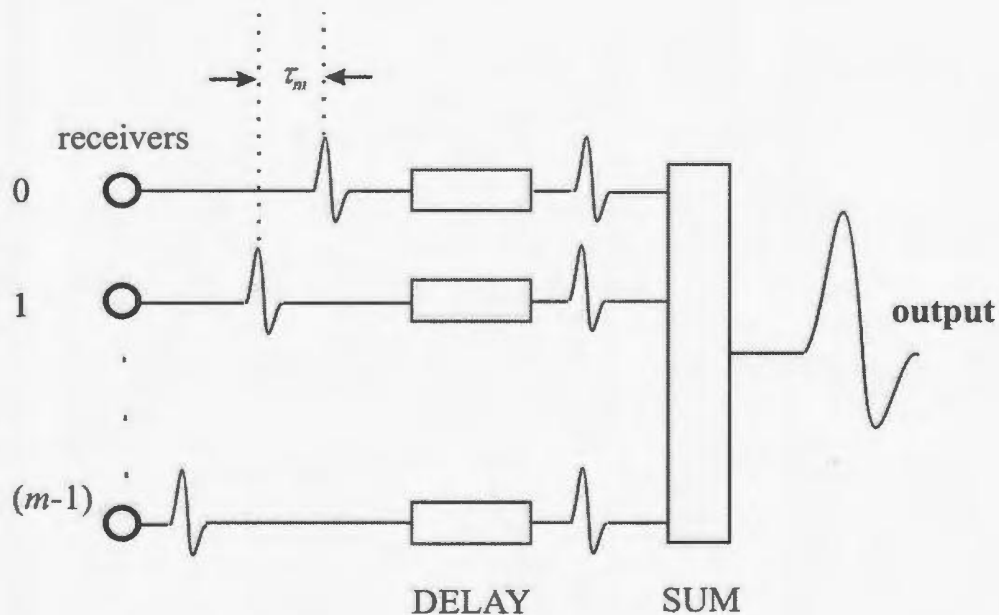
Figure 3.1
Delay-and-sum beamforming concept (modified from Johnson and Dudgeon, 1993).

To illustrate this concept mathematically, we will refer back to equation 2 and assume that the receiver array receives a plane wave coming from a target in the far-field

as depicted in figure 2.6 (a). The waveform $s(t)$ propagates across the array and each receiver samples it yielding

$$x_m(t) = s(t - \tau_m) + n_m(t),\tag{8}$$

where $s(t - \tau_m)$ is the delayed signal term at each receiver and $n_m(t)$ is the background noise field. The background noise field which may be due to scattering from near-surface irregularities or inhomogeneities is assumed to be temporally uncorrelated from one receiver to next. Since the beamformer is very sensitive to noise, it may be useful to prefilter the data as much as possible. Outputs from the receivers are weighted and delayed appropriately and then summed to produce the beam output represented by

$$y(t) = \sum_{m=0}^{M-1} w_m x_m(t - \tau_m),\tag{9}$$

where w_m is the amplitude weight of the mth receiver. The weights are primarily applied to attenuate the sidelobes (smaller peaks appearing on either side of the large lobe) of the beam response function thereby reducing the power leakage. The sidelobe levels indicate the ability of the beamformer to reject other angles but the angle the wavefronts are coming from. The drawback in using weights to reduce sidelobe level is that there is always a tradeoff with the width of the *mainlobe* (the large lobe centered at the angle of incidence) of the beam response function. Reducing the level of sidelobes widens the mainlobe, thus, compromising resolution (see section 3.1.4 for the description). As already pointed out earlier, the receivers are assumed to have the same impulse response, thus, we can consider their outputs to be of equal magnitude. In this sense, they can be uniformly weighted. In this thesis we have used unity weights ($w_m = 1$).

Applying appropriate delays τ_m to the receiver outputs x_m before summing will reinforce plane wavefronts coming from a particular direction φ and tend to cancel those coming from other directions, as they will not be in phase.

Since in practice we deal with discrete data, a discrete version of equation 9 is required. The discrete beam output is given by (Johnson and Dudgeon, 1993)

$$b(n) = \sum_{m=0}^{M-1} w_m y_m (n - \Delta_m),$$ (10)

where Δ_m is the integer delay associated with the mth receiver. The integer delays are discrete multiples of the sample rate and their use means that we may not be able to form the beam exactly since ideal delays are not necessarily integer multiples of the sample rate Δt. This means that it is possible to form a beam only for discrete angles. To illustrate this, we note that permitted receiver delays are given by $\tau_m = \Delta_m \Delta t = mq\Delta t$, where q is an integer (i.e., $q = 0, \pm 1, \pm 2, \ldots$) and Δt is the sample rate of the data. By examining equation 7, propagation directions have the form $\varphi = \sin^{-1}(\frac{vq\Delta t}{d})$. If we consider a seismic system with the following set of design parameters: $v = 4000$ m/s, $\Delta t = 0.5$ ms and $d = 20$ m, we find that q cannot exceed 10. The discrete propagation angles for this system are: $0.00°$, $\pm 5.74°$, $\pm 11.54°$, $\pm 17.46°$, $\pm 23.58°$, $\pm 30.00°$, $\pm 36.87°$, $\pm 44.43°$, $\pm 53.13°$, $\pm 64.16°$ and $\pm 90.00°$. Thus, the response function gives only a fixed number of possible beams. This situation clearly limits the beamformer in practical usage. To form more beams using integer delays the separation distance d needs to be

increased or the sample rate Δt could be reduced within sampling requirements mentioned in section 2.3.

There are other alternative methods such as temporal or spatial interpolation that can be used that place less restrictions on propagation directions. Although interpolation is not being used extensively in this thesis, some spatial interpolation, carried out in the frequency domain, is used where a limited number of receivers are used to find propagation directions.

3.1.2 The frequency domain approach

Frequency domain beamforming involves treating the time delays as phase shifts after application of the Fourier transform to the receiver outputs $x_m(t)$. As already pointed out earlier, in time domain beamforming the receiver outputs are time delayed with respect to the first receiver. In the frequency domain, the time-delayed sequences transform into the phase shifted sequences (i.e. see equation 4 above). The Fourier transform of the beam output (equation 9) is given by

$$Y(f, \varphi) = \sum_{m=0}^{M-1} w_m X_m(f) e^{j2\pi f_D \tau_m(\varphi)}, \tag{11}$$

where $X_m(f)$ is the frequency transformed output, w_m is the amplitude weight, f_D is the dominant frequency and $\tau_m(\varphi)$ is the time delay of the mth receiver. If we assume $\varphi_0{}^\dagger$ is the angle of direction of the propagating wavefronts, using equations 5 and 11, we find

----

† φ_0 should not be confused with φ. φ_0 is the actual direction of the incoming wavefronts and φ is the assumed propagation direction of the wavefronts. The mainlobe's peak occurs when $\varphi = \varphi_0$.

that the beam output can be represented as

$$Y(f,\varphi) = \sum_{m=0}^{M-1} w_m \left[S(f)e^{-j2\pi f_D(\tau_m(\varphi_0)-\tau_m(\varphi))} + \hat{N}_m(f) \right].$$ (12)

The hat on top of $N_m(f)$ indicates that the noise field has been modified by a phase shift of $e^{j2\pi f_D \tau_m(\varphi)}$. Assuming the signal is narrowband and all its energy is concentrated at the dominant frequency f_D, the power of the beam as a function of the φ is evaluated simply by taking the square of the absolute magnitude of the beam output, i.e. $|Y(f_D,\varphi)|^2$ (Johnson, 1982; Maranda, 1989).

Equation 12 applies to the case where we are dealing with continuous time data, however it would not work in a situation where the output from the receivers is discrete. Thus, an appropriate method is used that takes care of the finite time intervals. This method is known as the discrete Fourier transform (DFT). An N-point DFT of a sampled sequence $x_m(n)$ with discrete values of frequency $f_k = kf_s/N$ (where f_s is the sampling frequency) is given as (Nielsen, 1991)

$$x_m(k) = \sum_{n=0}^{N-1} x_m(n)e^{-j\frac{2\pi k}{N}n}, \qquad \text{where } 0 \le k \le N\text{-}1.$$ (13)

Equation 13 represents the discrete frequency transformed data. Using this equation and equation 11, the discrete frequency domain representation of the beam output becomes

$$Y(k,\varphi) = \sum_{m=0}^{M-1} w_m X(k)e^{j\Omega mk},$$ (14)

where $\Omega = 2\pi \delta_s \sin(\varphi)/N$ and $\delta_s = df_s/v$. This can be written compactly as

24

$$Y = X.a \tag{15}$$

where $X = \begin{pmatrix} X_0(k) \\ X_1(k) \\ \vdots \\ X_m(k) \end{pmatrix}$ and $a = \begin{pmatrix} w_0(k)e^{j\Omega mk} \\ w_1(k)e^{j\Omega mk} \\ \vdots \\ w_m(k)e^{j\Omega mk} \end{pmatrix}$. One advantage of this method is that the

sampling frequency, f_s, does not affect arrival angle resolution. It only has to satisfy the

sampling requirements mentioned earlier. Another advantage is that equation 14 can be

computed using the fast Fourier transform (FFT) algorithm (Mucci, 1984). The beam

power output from the DFT approach can be computed by taking the square of the

absolute magnitude of the beam output just like in the continuous time case.

3.1.3 Array steering

Array steering can be achieved by physically changing the orientation of the array or by

electronically (analogue or digital) changing the position of the mainlobe of the array

response output (Burdic, 1991). One example of mechanical steering is found in radar

systems where parabolic dish antennas rotate to scan the wavefield for incoming energy.

In sonar and seismic systems this is not usually done because of the wide aperture

needed, the heavy equipment involved and also because the noise generated by the

rotating array would mask the signal we are trying to detect. Instead, electronic steering is

the preferred method for these types of systems.

We shall focus on digital steering which is the method used in this thesis. Digital

steering involves introducing a set of time delays to each receiver element before

summing. Considering a uniform linear array, for a single-frequency signal, this is

25

equivalent to applying phase shifts to the frequency transformed receiver outputs. Note that this array steering corrects for the phase lag of the incoming wave, arriving from the direction φ_0, due to the position of each individual receiver with respect to the first receiver. Thus, signals coming from φ_0 will be in phase at each receiver and will add coherently.

A schematic representation of this concept is shown below in figure 3.2. Time delays, $\tau_m(\varphi)$, shown are equivalent to a phase shift defined by $\Phi_m = 2\pi f_D \tau_m(\varphi)$. Noting that the first receiver acts as a reference point, τ_1 - τ_4 are added to the outputs of the corresponding elements to align the wavefront with the main axis of the array.

Digital array steering can be performed in two different situations. For systems designed for radiation of energy, the steering direction is known beforehand. Examples of
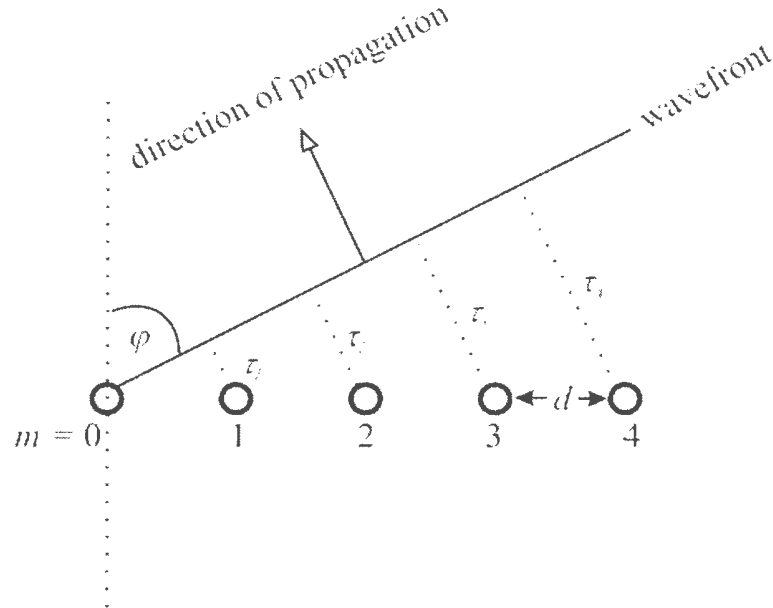
Figure 3.2
Schematic of a plane wave passing across a uniform linear array of receivers.

such an application are tracking of fish using side or multiple scan SONAR, tracking of moving vehicles in RADAR and tracking of mobile phones in communications.

In most seismic situations and other SONAR applications systems are designed for the reception of energy. The target, and hence the wavefield propagation parameters, are fixed. Thus, the direction of propagation is not known. By performing steering in these situations, we systematically vary delays to scan the wavefield which is fixed. The output response will produce a maximum when the trial angle corresponds to the angle of arrival of the wavefield. The above approach is used in this thesis where a shot is fired and the uniform linear array attempts to scan for the energy reflected by a point source (representing a massive sulfide body in the subsurface).

The following discusses the effect of aperture length (array size) on the resolution of the array. As we will see, it is crucial in determining a scatterer's location or direction accurately.

3.1.4 Array resolution

Resolution describes the ability of a beamformer to determine a wave's direction of propagation and to distinguish between closely spaced sources or scatterers. The resolution is determined by the characteristics of the receiving array and the signal. The resolution properties of the conventional beamforming method are generally defined in terms of the Rayleigh criterion (Stoica and Moses, 1997; Van Trees, 2002). According to this criterion, two waves are resolved when the peak of the array response of the first

wavefront falls on or outside the first zero of the array response due to the second wavefront.

We will now look at the definition above in detail. Since the definition of resolution above describes the ability of the receiving array to localize a target or scatterer, it can be described in terms of wavenumber or angle of propagation relative to the array. The apparent wavenumber represents two kinds of information: direction of propagation and wavelength. Thus, propagation direction or wavelength, or both can localize a propagating wave. This localization can be interpreted as a form of wavenumber filtering by the delay-and-sum beamformer. The output response's mainlobe or mainbeam is equivalent to a wavenumber passband, the narrower this band the more selective the filter (Johnson and Dudgeon, 1993). Thus, the width of the mainlobe determines the resolution of the beamformer.

Further insight into resolution is gained by describing it in terms of the angle of propagation. The apparent wavenumber is directly related to the angle of propagation, although nonlinearly. The angular span of the mainlobe is commonly measured at the half-power (-3dB) points or from null-to-null of the mainlobe (Manolakis *et al.,* 2000). Figure 3.3 below shows a beampattern (spatial response of the beamformer) with these points marked.

So far we have not discussed how the total number of receivers and aperture length affect the resolution of the array. In seismic exploration our natural desire is to have as many receivers or sources as possible or to cover as wide an area as possible. As we will see shortly the larger the size of the array the finer the resolution.
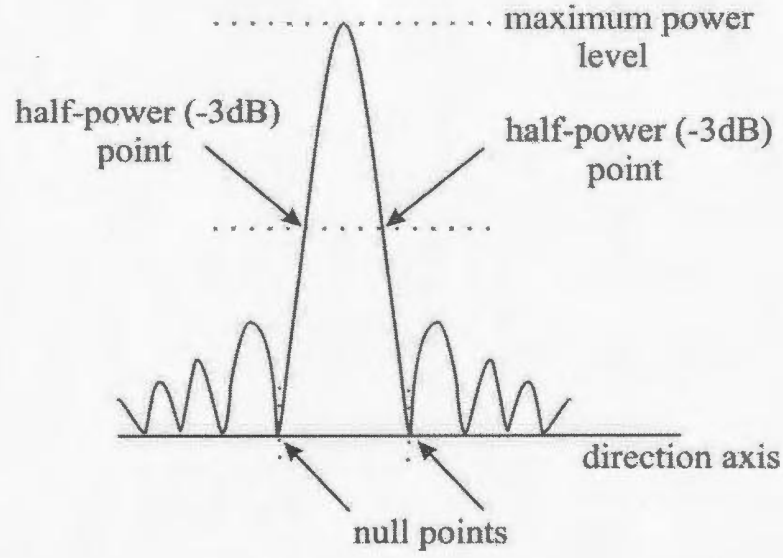
Figure 3.3
Example of a beampattern of a uniform linear array showing the −3dB and null-to-null points.

As pointed out earlier, the resolution of a receiver array is determined by the size of the beamwidth which is measured at half-power or null-to-null points of the main beam. For a uniform linear array this is quoted in radians as (Manolakis *et al.*, 2000)

$$\Delta\varphi_{3dB} \approx 0.89\frac{\lambda}{L}, \tag{16}$$

where, $L = Md$ is the aperture length of the array. We note that if we increase L or equivalently if we increase the total number of receivers M in the array this angular span gets smaller thus resulting in a narrower beam.

The null-to-null beamwidth denoted by (van Trees, 2002)

$$\Delta\varphi_{nn} = 2\frac{\lambda}{L}, \tag{16}$$
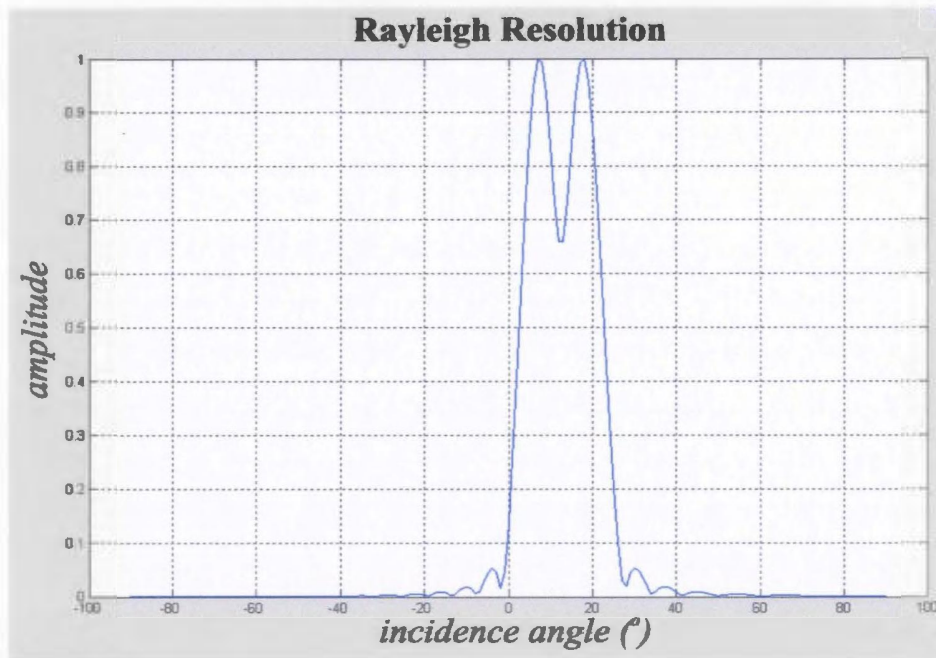
(a)
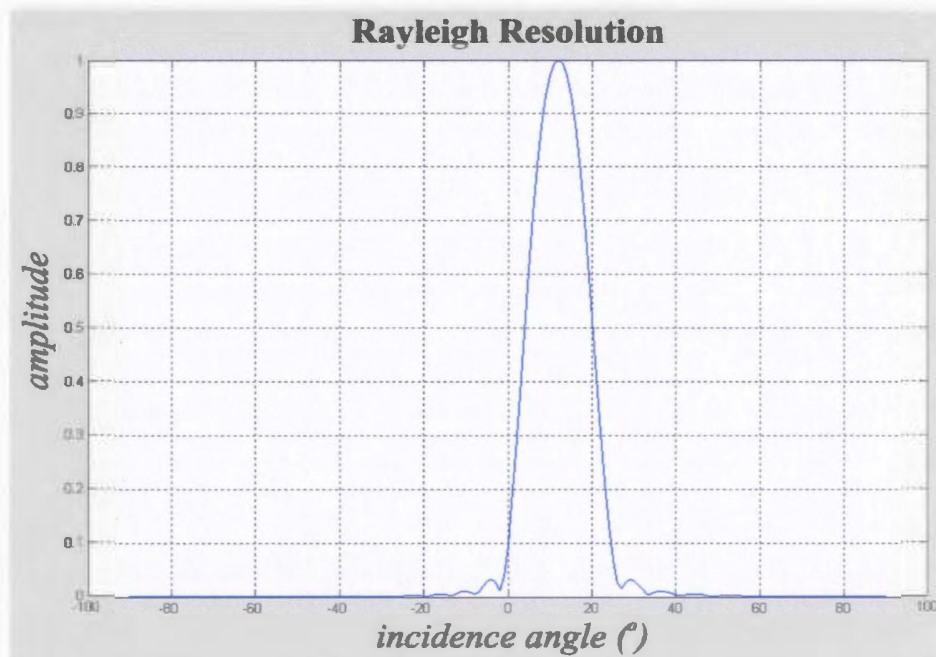
(b)

Figure 3.4
Explanation of Rayleigh resolution criterion. As can be seen waves are clearly resolved in (a) where the criterion is satisfied. In (b) the criterion is violated and the two waves are not resolved.

where L is as defined above provides us with a measure of the ability of the array to resolve two closely spaced scatterers. This quantity, known as the Rayleigh resolution limit (van Trees, 2002), shows that the directions of arrival of two wavefronts should differ by more than $\Delta\varphi_{nn}/2$. Figure 3.4 above gives an example of this scenario. Figure 3.4 (a) shows beam responses of two uncorrelated wavefronts at the same dominant frequency of 50 Hz and medium velocity of 4000 m/s incident at angles $10°$ and $15°$ (or wavenumbers 0.0136 m^{-1} and 0.0203 m^{-1}) on a uniform linear array with 40 receivers and a spatial interval of 20 m. Figure 3.4 (b) shows beam responses of the same wavefronts but with incidents angles $10°$ and $14°$ (or wavenumbers 0.0136 m^{-1} and 0.0190 m^{-1}). In figure 3.4 (b) the limit of resolution is not satisfied since the wavefronts' directions of arrival differ by $4°$which is less than the resolution limit of approximately $5.88°$ of this system. The code, with the M-file name *rayleigh_res.m*, used to generate this example is found in Appendix A.

One other important aspect to obtain a good approximation of the angles of arrival of incident energy is the grating lobes, which is the subject of the next topic. These are additional lobes surrounding the main beam. They can create spatial ambiguities as they look just like the main beam and make it difficult to pick the actual directions.

3.1.5 Grating Lobes

When an omni-directional seismic source radiates energy into the subsurface, a large amount of energy is lost into the grating lobe angle directions. The receiver array response is periodic with a period of 2π. Thus, the mainlobe is repeated at intervals of
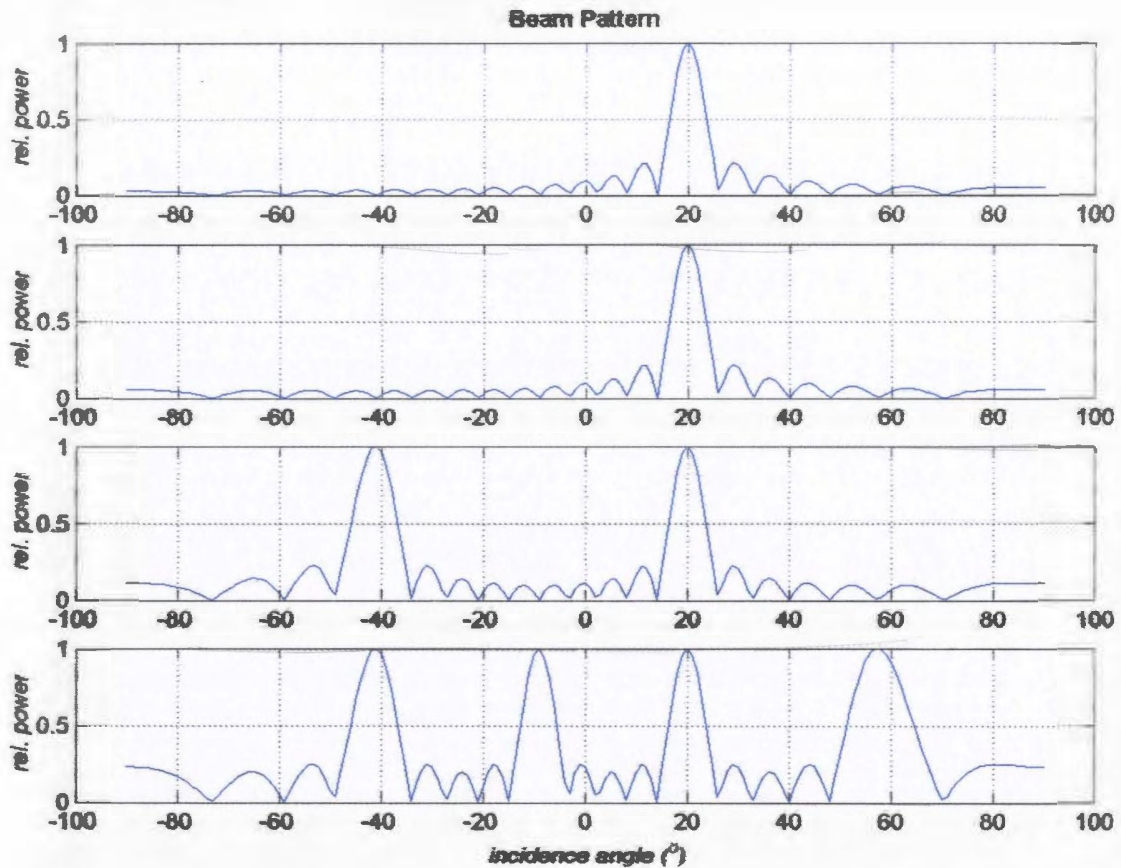
Figure 3.5
Array response function for different element spacings. The receiver spacings are (a) $\lambda/4$, (b) $\lambda/2$, (c) λ and (d) 2λ. Grating lobes occur for $d > \lambda/2$. Aperture length is kept at $L = 100\lambda$.

$2n\pi$ (where $n = 0, \pm 1, \pm 2, \ldots$). These repeated lobes are known as grating lobes. They appear on the same side of the main lobe as the sidelobes discussed earlier. If the receivers sample the reflected energy inadequately (i.e., spatially aliased), the beamformer will not be able to distinguish signals appearing to arrive from these grating lobe directions from those arriving from the direction of interest. The appearance of these ambiguous lobes in the beamformer output simply indicates that spatial aliasing has taken place. In order to avoid this situation the receiver spacing should be chosen such that it is

less than or equal to half the operating wavelength (see section 2.3). If it is not possible to choose a separation that would guarantee no aliasing, angles at which these grating lobes occur can be calculated and avoided. Also, in some situations it is known that certain angles are improbable thus signals from those angles can be ignored. In the above example (figure 3.5) we illustrate how this phenomenon appears in the beamformer output. The direction of arrival of the signal is $20°$. But other lobes occur at $-40°$, $-10°$ and $60°$ if the spacing is greater than $\lambda/2$. In all the examples the array aperture is kept the same. The example is generated by using the MATLAB® script *grat_lbs.m* shown in Appendix A.

3.2 Description of the algorithm

Using the above theoretical background, a MATLAB® code was written to carryout the objectives of this thesis. The program code *center_css.m* in appendix B, which is the main program for this thesis, initially defines parameters for the input data. Most of the command lines have a comment at the end giving more details about the command. The second part of the program gives parameters for windowing or segmenting the data. These parameters are dictated by the characteristics of the input data. The segmentation is made in such a way that it satisfies the planar wave criterion mentioned in section 2.1. The length of each segment should be less than the root of half the product of the depth and wavelength, i.e., $l < \sqrt{\dfrac{z\lambda}{2}}$. It should be emphasized here that in a real situation the depth is not known, which is one of the parameters we would be trying to determine from

the measurements. An alternative to making sure that the plane wave criterion is satisfied is to visually determine the flat portion of the diffraction hyperbola and then segment the hyperbola based on this approximation.

The third part of the program opens the data file and arranges it into rows and columns representing time samples and receivers, respectively. It also counts the number of data points available.

After opening and arranging the data the program calculates a theoretical diffraction moveout curve using either equation 18 or 19 depending on whether the source (note that the source in this thesis refers to the device that produces waves and not the target which reflects them) is coincident with the scatterer. The theoretical solution approximates the diffraction hyperbola appearing in the input data and it helps in segmenting the data. After calculating the theoretical solution, the segment aperture (which should be equal to l) is calculated and then applied to the data to effect segmentation.

The above outlines the procedure followed by the program to prepare the data for beamforming. Each segment is processed separately. The beamforming section begins by bringing the data to zero mean to remove any dc shift in the input data. A discrete Fourier transform is then applied to the data in each segment for frequency domain processing. The beam response is then calculated by steering the array towards possible directions within the (-90°, +90°) interval. The steering is done using the exponential phase shift vector or the ARF shown in equation 6. The power in a particular direction is estimated by taking the complex dot product of the ARF (a^T) and the data matrix (X) and then
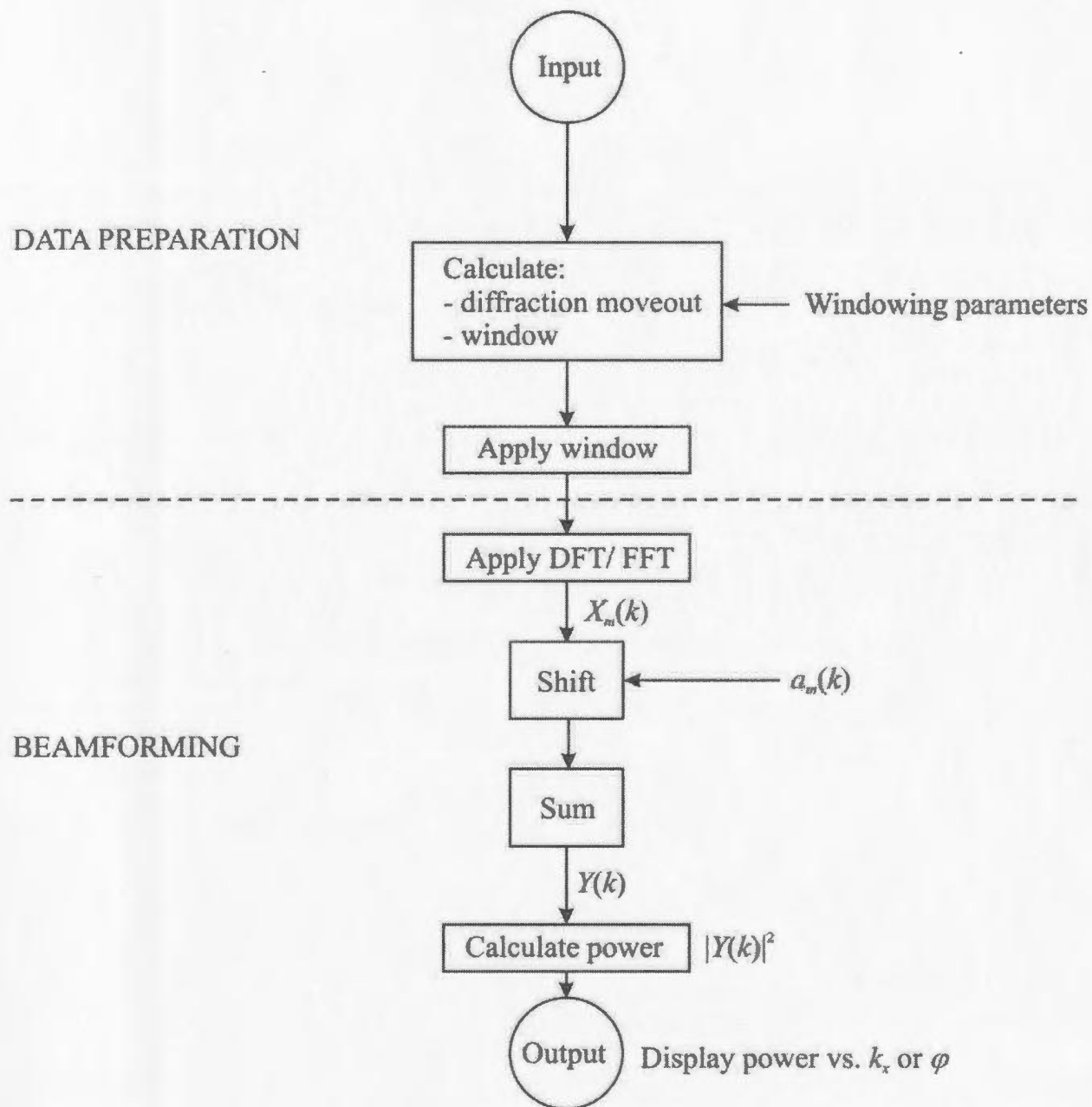
Figure 3.6
*Flow diagram of program **center_css.m**.*

summing the total energy over all receivers, i.e., $B(k,\varphi) = sum\left[Y(k,\varphi)^2\right]$. The results

can then be displayed using a desired scale. This program uses a decibel (dB) down scale

to display the results of the beamforming process. The direction of arrival of the signal is

indicated by the location of the maxima on the power vs. wavenumber or angle plot.

The above description of the source code is shown in the flow chart in figure 3.6.

The source code is for a coincident source and scatterer. For other geometries, the input

parameters as well as windowing parameters would need to be changed. The changes will

be indicated in the next chapter where the performance of the beamformer is assessed.

The results for each segment are displayed one at a time. The angles obtained from each

segment are different from each other since the beamforming is done on different

portions of the hyperbola. This allows us to project the angles back to a reflecting or

diffracting point, hence locating the target.

3.3 Summary

In this chapter, we have covered some important aspects for practical delay-and-sum

beamforming. The delay-and-sum beamforming can be performed in the time domain and

the frequency domain. The frequency domain approach has an advantage over time

domain implementations particularly when dealing with large volumes of data. In the

frequency domain, the beamforming process can be carried out faster using the FFT.

We have also described array steering as the process of maximizing the power of

the beamformer output in the direction from which the energy is coming. It involves

systematically applying phase shifts to each receiver output, provided the propagating signal is narrowband and then beamforming on the whole array. The direction of arrival of energy of the signal is determined at the location of the main beam on the power vs. wavenumber or angle plot.

The resolution of the beamformer is measured at half-power (-3dB) points or from null-to-null of the main beam. It is controlled by the size of the array or the total number of receiving elements in the array. The larger the size of the array the tighter the beam width which implies a better resolution.

Finally, there are some limitations on the choice of receiver spacing d. To completely avoid spatial aliasing or equivalently grating lobes in the beam power response, the receiver spacing should be set equal to or less than half the wavelength. Grating lobe directions can be calculated, in some situations, and be avoided.

The algorithm which was used to carryout the objective of this thesis is presented. The code involves data preparation prior to beamforming. The data has to be segmented to avoid violating the planar wavefront criterion. Beamforming is then done on each segment to look for possible sources of energy. Each angle or direction from each segment provides a means of finding the location of the scatterer.

Chapter 4

Evaluation Of The Beamformer

In this chapter, we apply the concepts discussed in the previous chapters to synthetic data. The chapter explains how the data was generated and prepared for beamforming (section 4.1). The capability of the beamformer is assessed by evaluating a number of performance measures (section 4.2). These measures focus on the directivity and the response of the array under different conditions. First, we look at how well the beamformer can resolve angle of emergence of impinging wavefronts. In addition, we back-project the wave trajectories to assess how well they can localize a scatterer. The data is then subjected to different noise fields and the same procedure for angle resolution and scatterer localization is repeated. Next the data is decimated in the spatial domain and the same procedure is repeated. Finally, the performance of the beamformer is assessed in the presence of multiple scatterers. This establishes the spatial resolving power of the beamformer.

4.1 Data preparation

4.1.1 Generation of data

Synthetic seismic data were generated using a second order finite-difference modeling algorithm implemented in Seismic Unix®. The scatterers were modeled as square-shaped geological blocks placed at a depth of 300m (fig. 4.1). A shot was placed directly
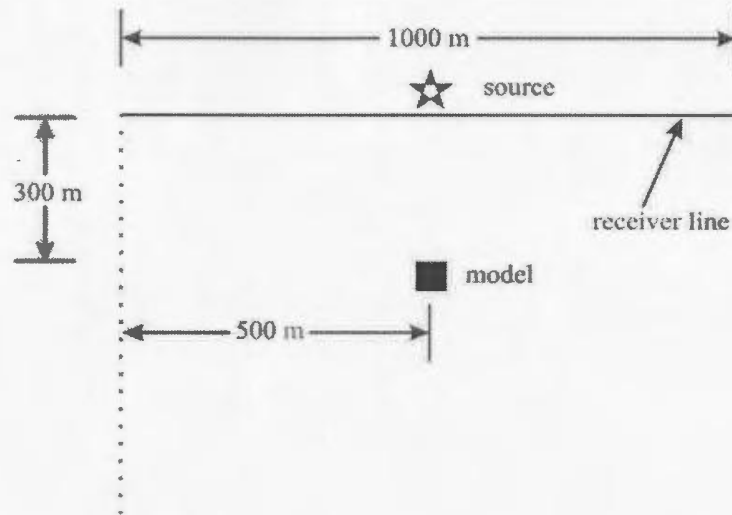
Figure 4.1
Geological model representing a massive sulfide deposit.

above the scatterer or at some offset on one side of the scatterer as depicted in figure 4.2

(a) and (b). The diffraction hyperbolas generated have moveouts determined by the

background velocity. These diffraction hyperbolas were captured by the linear array

directly above the scatterers. Figure 4.3 shows diffraction traveltime curve for a
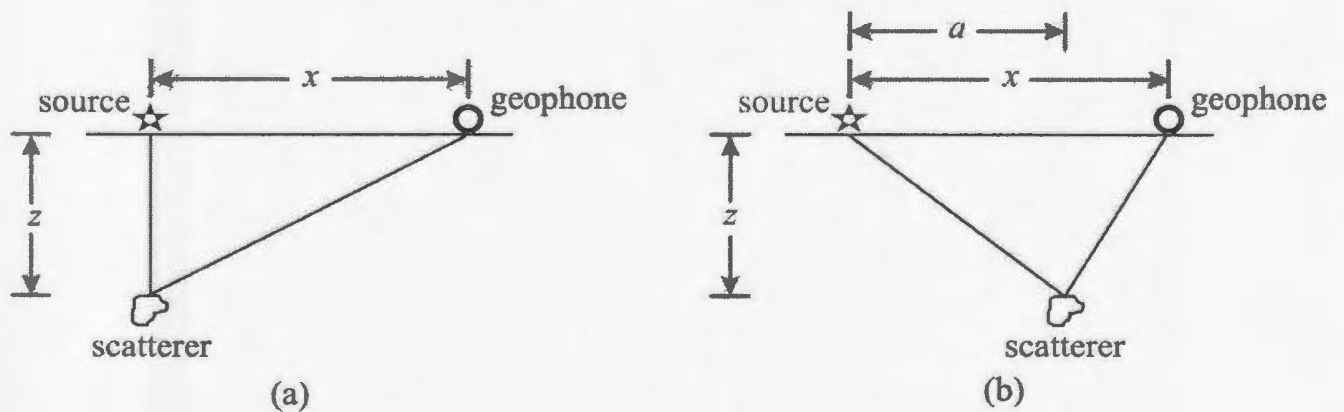
Figure 4.2
Geometry of a source (a) coincident with the scatterer, and (b) offset from the scatterer.
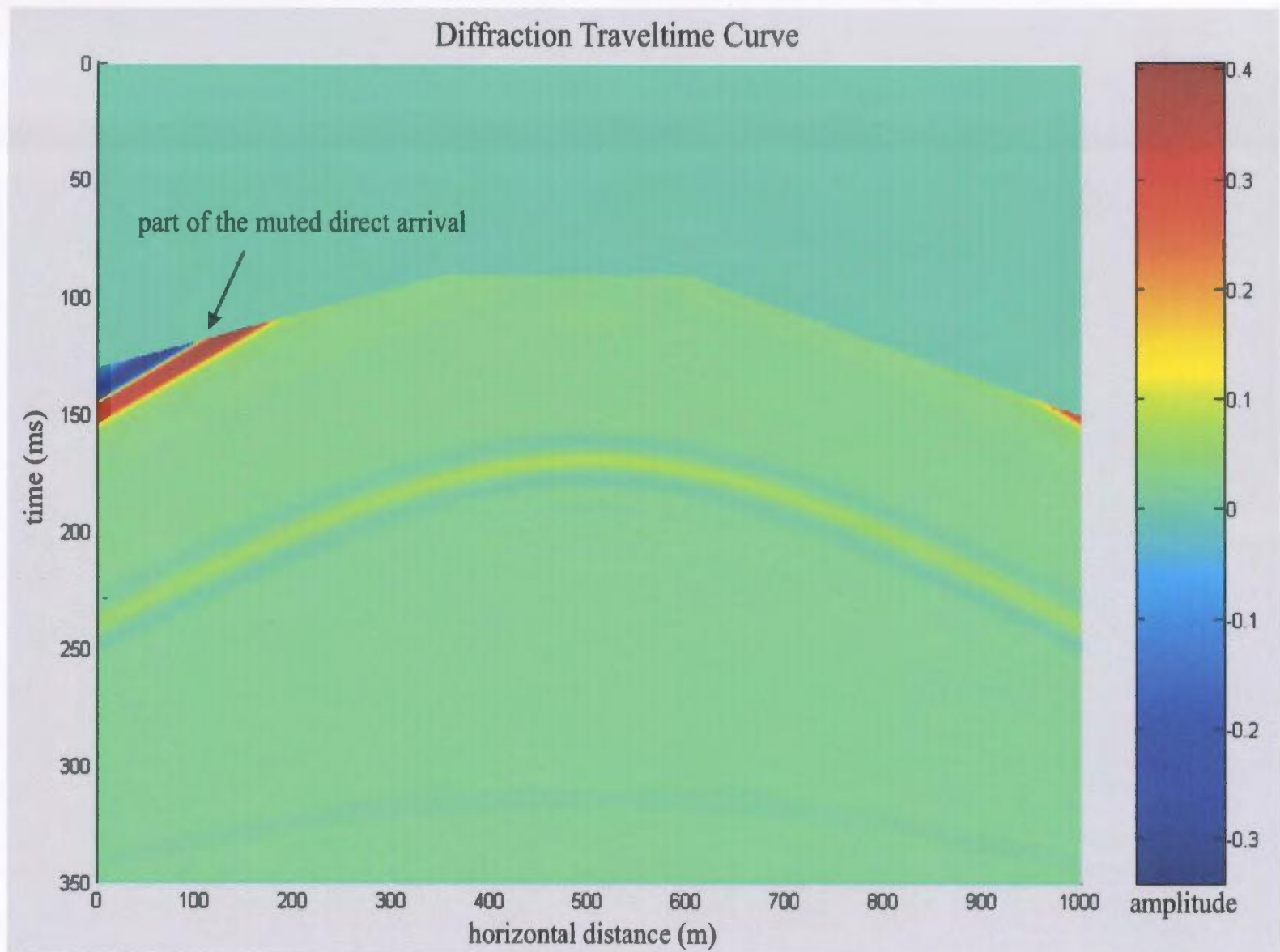
Figure 4.3
Diffraction traveltime curve for a coincident source and scatterer.

coincident source and scatterer. Since the direct wave, which arrives first at the receiver array, had higher amplitude than the diffractions, it was muted out to enhance visualization of the low energy diffraction.

The number of traces generated was equivalent to the number of geophones in the array. The trace interval was varied from 1m to 10m and then 20m. Trace intervals other than 1m involved decimation of data in the spatial domain. The waveform was sampled at 0.5ms, and the dominant and the maximum frequencies of the waveform were set at 50Hz and 100Hz, respectively to simulate realistic exploration data. The x-axis in the records (e.g., figure 4.3) represents the spatial dimension and the y-axis represents the two-way travel time. The frequency content of the data is shown in figure 4.4 below.
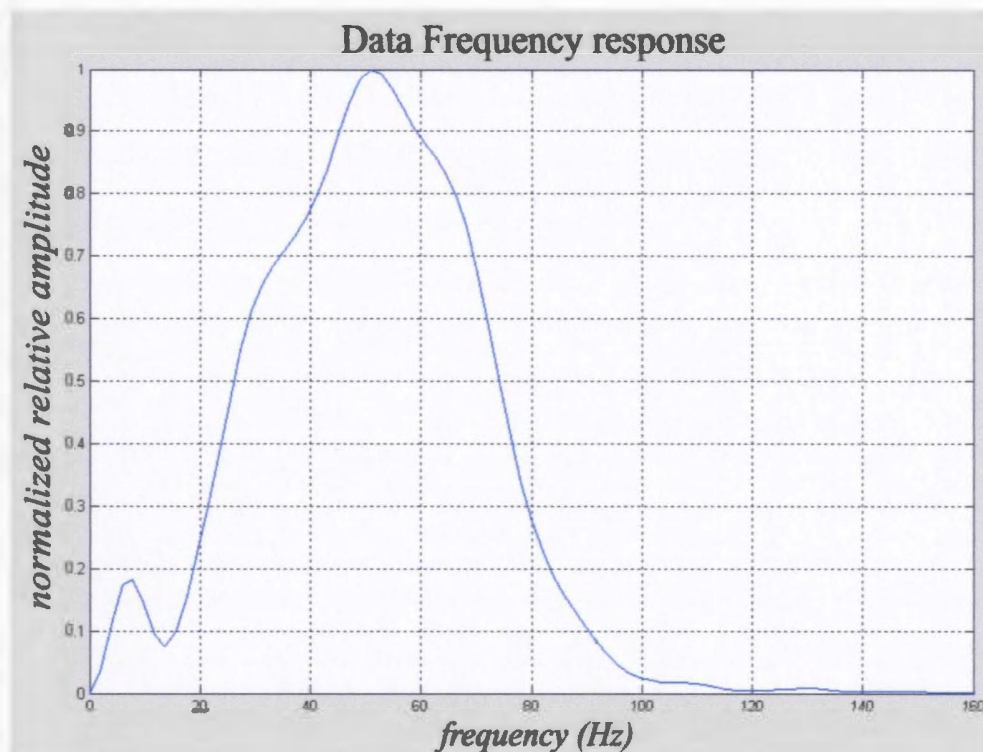
Figure 4.4
Frequency content of the data generated using the finite-difference method.

4.1.2 Data segmentation

To satisfy the plane wave assumption of the beamformer the diffraction must be segmented. In order to segment the data, the position of the apex of the diffraction moveout was noted. A theoretical curve governed by the geometry of the array and the background velocity was fitted to the diffraction hyperbola. An exact fitting of the hyperbola is not necessary; the theoretical curve only guides the segmenting program to which part of the data set to work on. For a coincident source and scatterer (fig. 4.2 (a)) where the depth to the diffracting point is much greater than the offset, i.e., where $z \gg x$, the theoretical solution is given by (Sheriff and Geldart, 1995)

$$t_d \approx t_0 + \Delta t_n. \tag{18}$$

where $t_0 = \dfrac{2z}{v}$ is the travel time of a geophone at the source point and $\Delta t_n = \dfrac{x^2}{4vz}$ is the normal moveout. For a non-coincident source and scatterer Sheriff and Geldart (1995) gives the theoretical solution as

$$t_d \approx t_0 + 2\Delta t_n + \frac{a(a-x)}{vz}, \tag{19}$$

where a is the horizontal distance between the source and the diffracting point (fig. 4.2 (b)).

The segments' lengths were chosen in accordance with the planar wave criterion mentioned in section 2.1. For convenience, this criterion is stated again as follows;

$$z > \frac{2(maximum\ dimension\ of\ the\ array)^2}{wavelength}, \tag{20}$$

where z is the depth. Comparing this equation with equation 1, this simply tells us that the length of each segment in the spatial dimension should be less than the radius of the

42
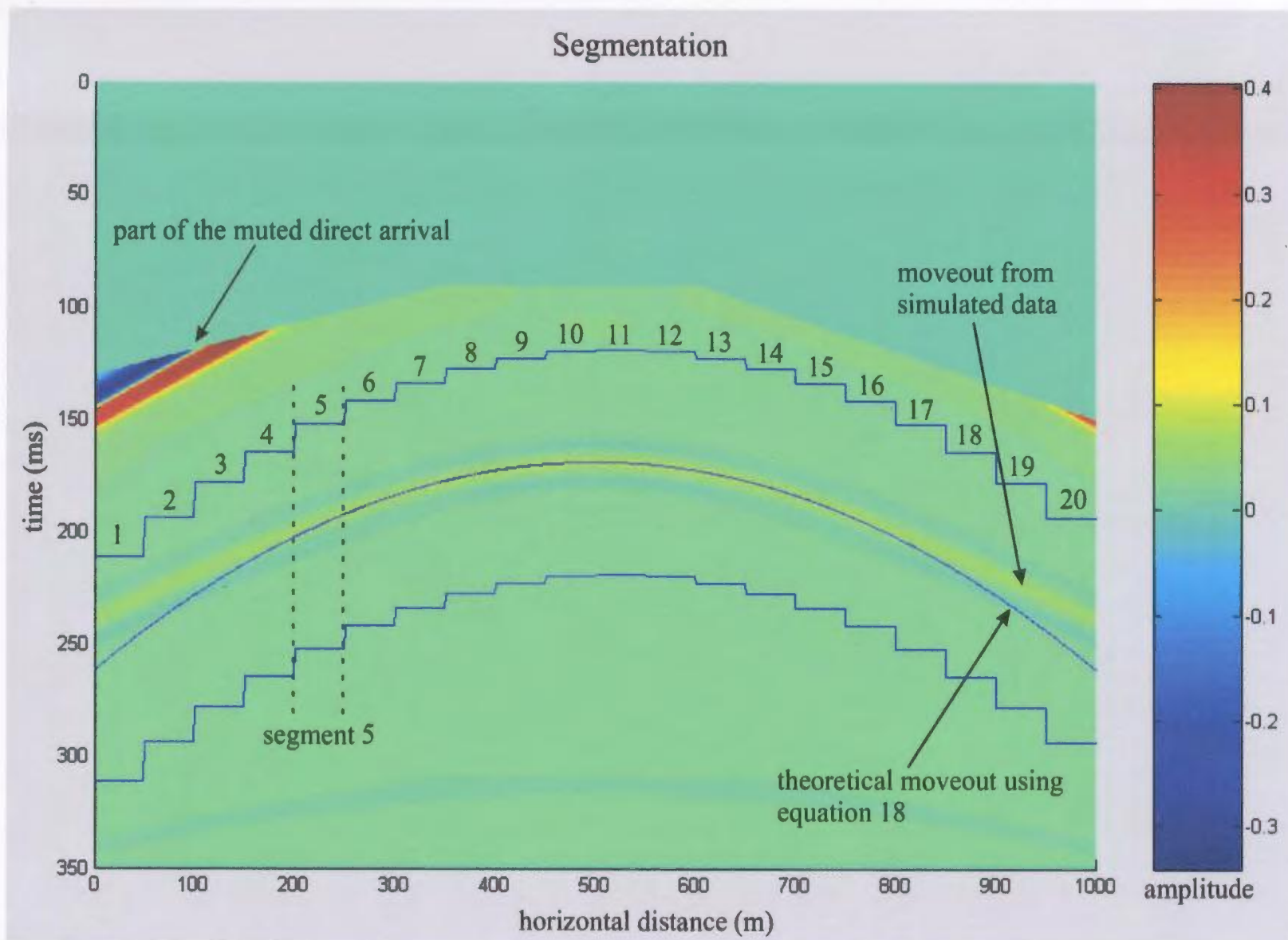
Figure 4.5
Segmentation of the simulated data.

Fresnel zone. An alternative way of selecting the segment length is to visually determine from the moveout how many receivers in the array define the flat portion of it.

Figure 4.5, from one of the experiments, shows a plot of the segmented data in the case where the source is coincident with the scatterer and with the following set of design parameters;

Sample rate, $\Delta t = f_s^{-1} = 0.0005$ s
Dominant frequency, $f_D = 50$ Hz
Background velocity, $v = 4000$ m/s
Velocity of the scatterer, $v_s = 7000$ m/s
Reflection coefficient, $R = 0.43$
Depth, $z = 300$ m
Number of receivers, $M = 1000$
Number of time samples, $N = 700$
Receiver spacing, $d = 1$ m

The reflection coefficient R is the ratio of the reflected wave amplitude to the incident wave amplitude. In terms of acoustic impedance (ρv), where ρ is the rock density and v is the compressional wave velocity, for normal incidence R is given by

$$R = \frac{A_1}{A_0} = \frac{\rho_2 v_2 - \rho_1 v_1}{\rho_2 v_2 + \rho_1 v_1}, \tag{21}$$

where A_0 and A_1 represent displacement amplitudes of incident and reflected compressional waves and subscripts 1 and 2 represent first and second media, respectively. In the above set of design parameters, the massive sulfide deposit is assumed to have a density of 4.15 g/cm^3 and the crystalline host rock is assumed to have a density of 2.92 g/cm^3. Thus, using the above design parameters, the flat portion of the hyperbola would be satisfied by a length not exceeding 109.5 m or a maximum of 109
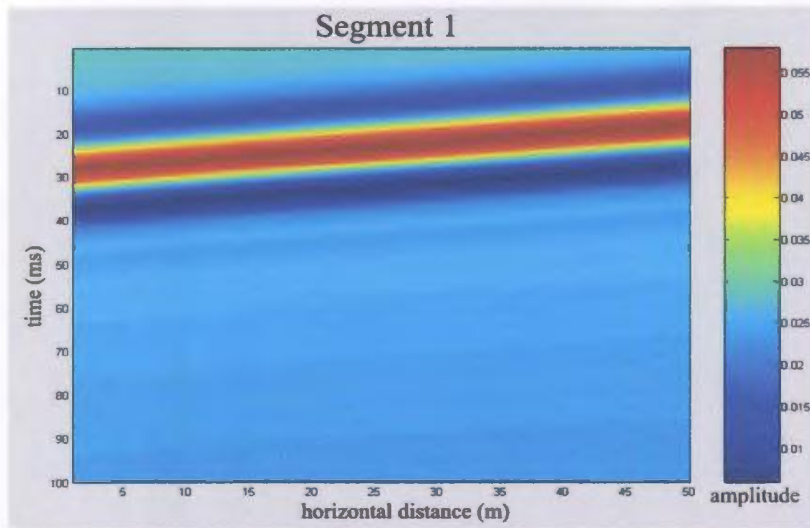
Figure 4.6
In all the plots, the x-axes and the y-axes represent horizontal distance in metres and time in samples, respectively.
(a) Plot of the first segment.
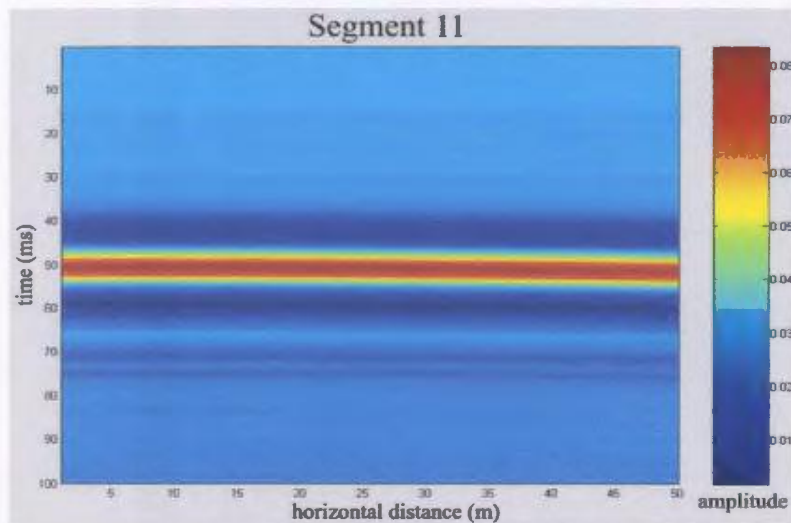
(b) Plot of the eleventh segment.
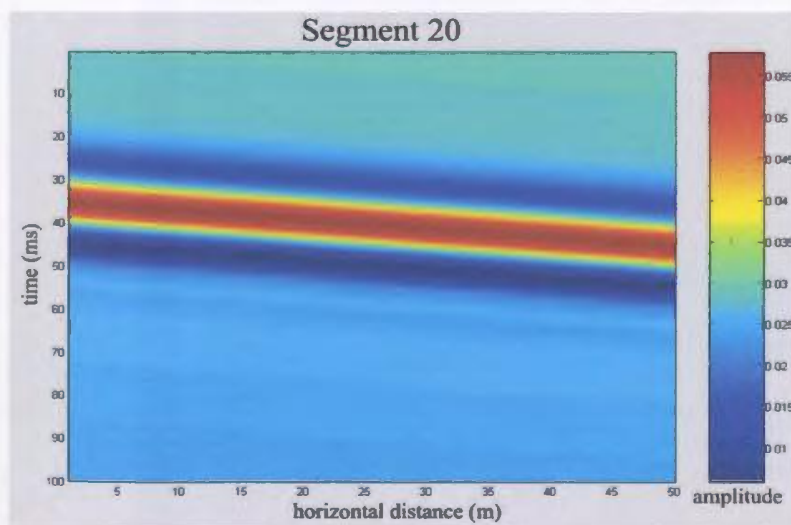
(c) Plot of the twentieth segment.

receivers in the array. In figure 4.5 the length was chosen as 50 m or 50 receivers. Since the uniform linear array for this figure contained 1000 elements, the total number of segments was twenty. Figure 4.6 shows individual plots of the first, middle and last segments as we go from left to right on figure 4.5.

4.2 Beamformer performance

4.2.1 Angle estimation

We will continue to restrict our attention to the uniform linear array (ULA) where the receivers are uniformly distributed over a horizontal plane surface. We start by looking at the situation where the source is coincident with the scatterer and they are both at the center of the array. After segmentation or windowing of the data, an N-point DFT was applied to each window for frequency domain processing. N in this evaluation of the beamformer represents the total number of time samples in a window or segment. As pointed out earlier, casting the data into the frequency domain has advantages over time domain processing. Frequency domain processing is less cumbersome than time domain processing particularly if the data set is very large. The sampling frequency f_s does not affect beam steering directions. The frequency transformed data represented by equation 13 has a beamforming equation as shown in equation 14. It should be noted that the DFT was applied only to the time dimension and not the space dimension. One critical assumption to note is that the receivers have the same signal term $S(f)$, thus the output from each receiver is the same but phase-shifted by an amount determined by the location, $r_m = md \sin \varphi$, of each receiver. Since the signal term is the same throughout all

the elements in the array, and is independent of the angle of direction, we will focus only

on the direction vector $a(k) = e^{j\Omega mk}$ which appears on the right side of equation 14. Let

us rewrite this direction vector as $a(k) = e^{jk_x md}$, where $k_x = \dfrac{2\pi k}{N} \dfrac{f_s \sin \varphi}{v}$ is the

horizontal wavenumber component of the propagating wavefront. The angular direction

of propagation is related to the wavenumber by

$$\varphi = \sin^{-1}\left(\frac{Nvk_x}{2\pi kf_s}\right). \tag{22}$$

The frequency index k should not be confused with the wavenumber component k_x.

Using MATLAB® a uniform linear array with the following design parameters was

analyzed:

Sample rate, $\Delta t = f_s^{-1} = 0.0005$ s
Dominant frequency, $f_D = 50$ Hz
Propagation velocity, $v = 4000$ m/s
Depth, $z = 300$ m
Number of receivers, $M = 1000$
Number of time samples, $N = 700$
Receiver spacing, $d = 1$ m

The shot position was in the centre of the array and directly above the scatterer. The

program code *center_css.m*, which is also the main program, is given in Appendix B. The

data was segmented into 20 windows of size 50 traces by 200 time samples. Each

segment was processed individually to determine the direction of propagation of the

incident wavefront. Figure 4.7 gives an example of the array response of the first segment

that was shown earlier in figure 4.6. The beam power pattern or spectrum is plotted with

a dB scale. The range of k_x values falls within the Nyquist values – 0.5 and 0.5 m^{-1}. Since
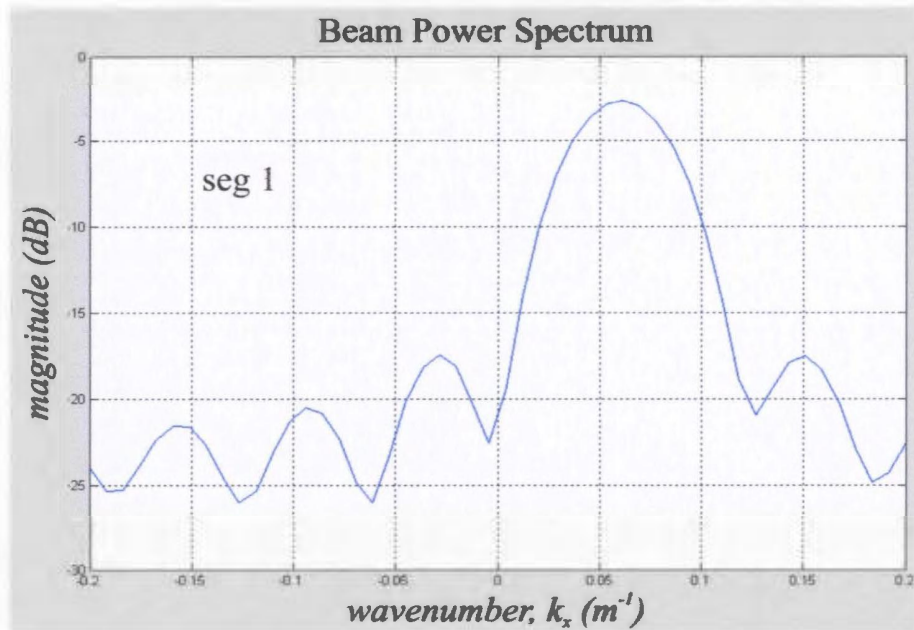
Figure 4.7
Normalized array response of the beamforming operation on the first segment consisting of 50 receivers and 200 time samples. The peak of the main lobe is located at 0.06 m^{-1} or at an angle of 49.8°.

the main beam spans a limited range of wavenumber values, the response is shown within

a range of -0.2 and 0.2 m^{-1}.

Table 4.1 below shows incidence angles obtained from all the segments. The

array responses of all segments are shown together in figure 4.8. Since the angles

represent a direction vector for each segment along the diffraction hyperbola, it was

possible to project them back to the original scattering point. The following discussion

explains this procedure.

Table 4.1: *Incidence angles obtained from the data with a coincident source and scatterer.*

Segment Number	k_x (m^{-1})	φ (degrees)
1	0.06	49.8131
2	0.057	46.5309
3	0.053	42.4399
4	0.05	39.5402
5	0.047	36.7570
6	0.043	33.1951
7	0.04	30.6169
8	0.033	24.8452
9	0.022	16.2669
10	0.008	5.8462
11	-0.008	-5.8462
12	-0.022	-16.2669
13	-0.03	-22.4559
14	-0.039	-29.7729
15	-0.042	-32.3277
16	-0.045	-34.9567
17	-0.05	-39.5402
18	-0.053	-42.4399
19	-0.056	-45.4807
20	-0.06	-49.8131
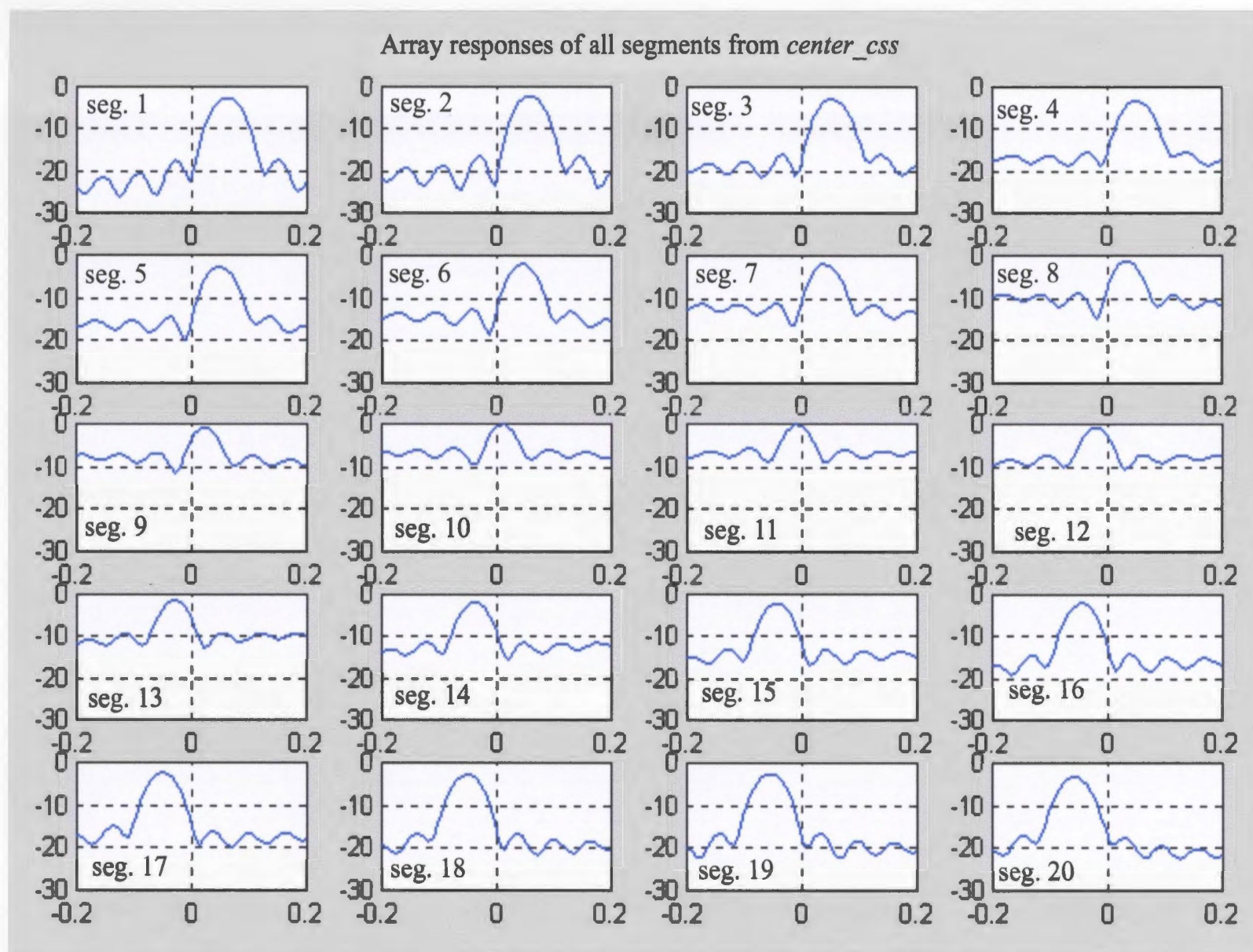
Figure 4.8: *Array responses from center_css.m*

4.2.2 Projection of angles to a point

The main emphasis of this processing step is in assessing the performance of the algorithm to see how best it can be helpful in determining the location of the target in the subsurface.

Examples

a. Source and scatterer at the centre of the array

The model used in this investigation was shown above in figure 4.1. The target was placed at a depth of 300 m in the middle of the array. Angles of incidence of the propagating wavefronts obtained from the segments were used together to trace back the origin of the wavefronts. Since the background medium had a constant velocity the rays were straight and thus it was possible to make linear projections back to a common point of intersection. The angles in table 4.1, obtained from the program *center_css.m* were used for the projection.

Using the relation $z = x/\tan \varphi$, where z is the depth, x the horizontal distance and

(a)
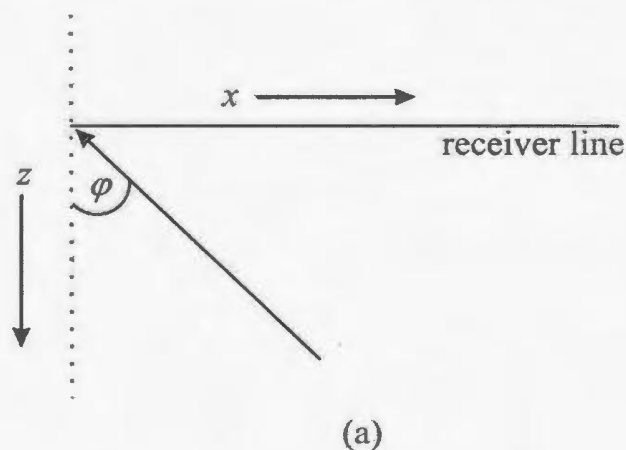
Figure 4.9: *(a)*
Schematic used to calculate the raypaths. Incidence angles clockwise from the axis normal to the array were treated as negative and those anticlockwise were treated as positive.

φ is the angle of incidence (refer to figure 4.9 (a)), raypaths were calculated and plotted on horizontal distance versus depth plot (figure 4.9 (b)). These raypaths are expected to originate from a common point which represents the target. The intersection of every ray with other rays was noted and plotted in figure 4.10. There is some scatter in the position of the intersection points but they are concentrated at some area in the plot. Because of the statistics we expect the target to be somewhere within this area of concentration. Points that are far from this area of concentration would obviously introduce errors when computing a common intersection of all the points. Thus, some averaging methods were used that addressed this problem. The common intersection was found by taking the simple average of all points or employing the least-squares fit or using some weighted average that took account of the distance of a point from a presumed position within this
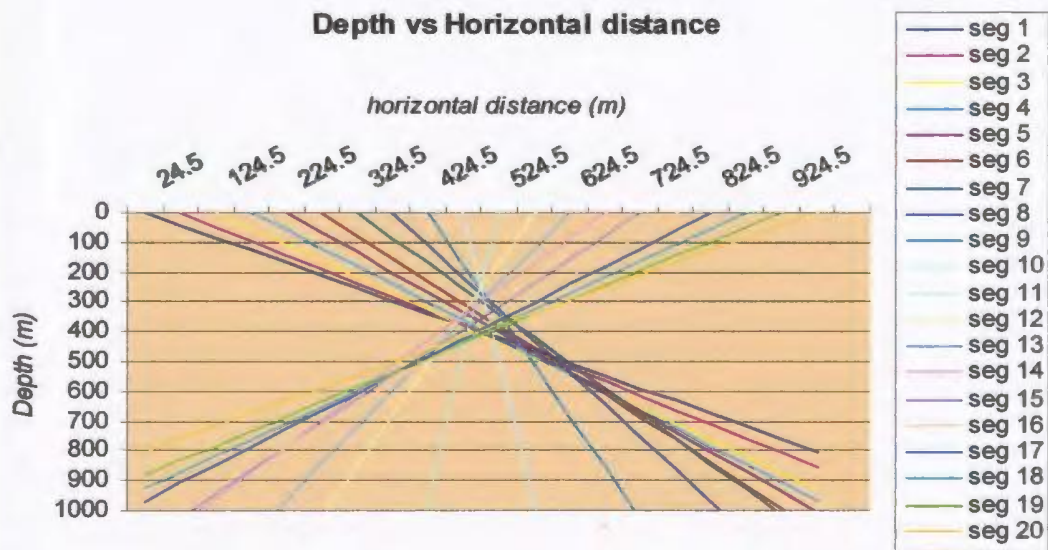
Figure 4.9: *(b)*
Raypaths from all segments projected back to a common point of origin.

area of concentration of points. A simple average of all points gave a horizontal distance of 504 m and a depth of 415 m as a solution. This is shown in table 4.2. The least-squares

Intersections

horizontal distance (m)
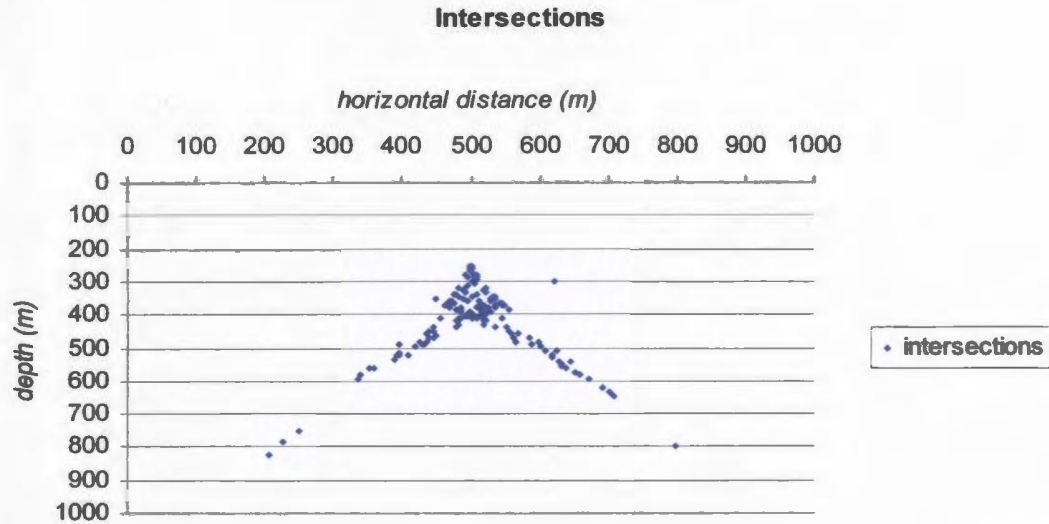
Figure 4.10
Intersection points of raypaths with each other.

Table 4.2: *Location estimates for the scatterer with the source placed at the center of the array and directly above it. The scatterer position in the x- direction is measured relative to the position of the first receiver while that of the source is measured relative to the position of the scatterer.*

	Actual location of the scatterer	Position of the source	Simple average solution	Least-squares solution	Weighted average	
					Starting location	Weighted solution
Horizontal distance x (m)	500	0	504	501	509	502
Depth z (m)	300	0	415	394	340	368

fit found the common intersection by measuring the square root of the mean of the

squares of the individual errors. The least-squares method included in Microsoft's Excel®

spreadsheet program was used to determine the solution. From the least-squares method

the horizontal distance and the depth of the common intersection were 501 m and 394 m,

respectively. The distance-weighting scheme calculated the common point of intersection

by down weighting points according to how far they were from a starting point and then

taking the average. Points that are far away from this presumed point receive lowest

weighting; this effectively reduces the error that may be introduced by these points. A

point, $(509, 340)^\dagger$ in meters, within the area of concentration was chosen as a starting

point. Values closest to this presumed point of intersection were allocated higher weights.

To make the weighting simple, the closest point was weighted 1 and the farthest point

received the least weight. A Gaussian function represented by

$$f(r) = ae^{-\frac{r^2}{b}},$$

(23)

where $a = \dfrac{1}{\sqrt{2\pi\sigma^2}}, b = 2\sigma^2, \sigma$ is the standard deviation and the mean of the distribution

is zero, was used to calculate the weights. r represented the distance between the starting

location and any intersection point. The weights used for the model are shown in

graphical form in figure 4.11. The common point of intersection using this method was

found to be (501.73, 367.89), i.e., a horizontal distance of 501.73 m and a depth of

367.89 m. The results displayed in figure 4.10 are shown again in figure 4.12 but with the

solutions from the simple average, the least-squares method and the distance-weighting

scheme included. The real target location was at a horizontal distance of 500 m and a

---

†The choice of the initial point in the weighted averaging scheme does not assume *apriori* knowledge of the
location of the scatterer. The point is chosen at random from a concentration of intersection points.

Normalized weights
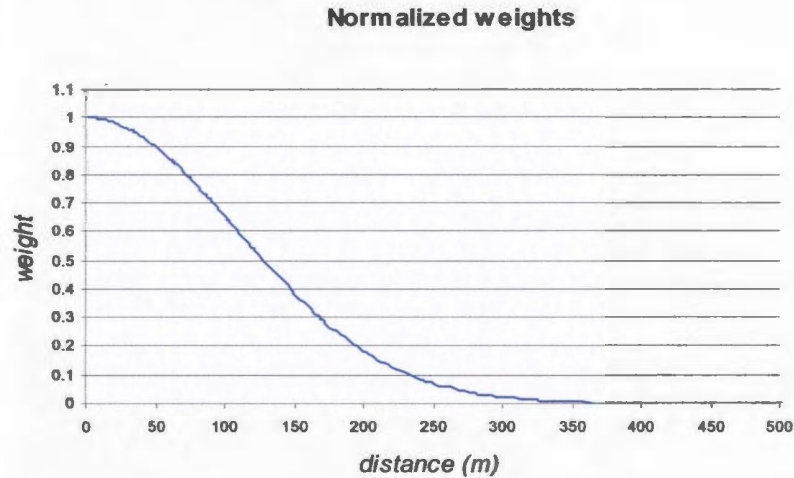
Figure 4.11
Normalized weights applied to intersection points. A Gaussian distribution with mean zero was used to calculate the weights. The distance (r) represents the location of an intersection point away from the expected target location.
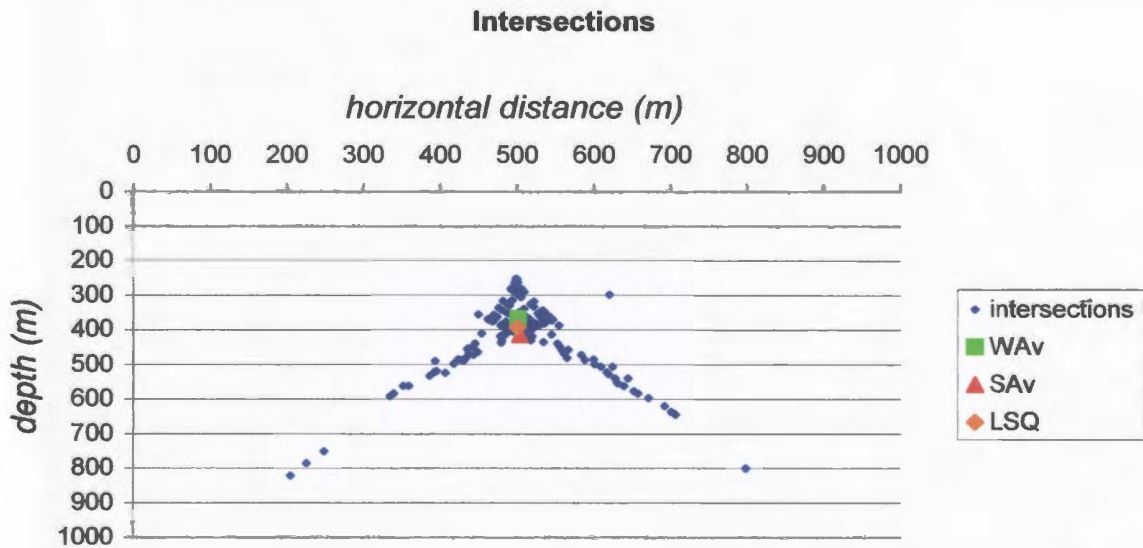
Intersections

Figure 4.12
Intersection points of raypaths with the solutions from simple average (SAv), weighted average (WAv) and least-squares (LSQ) methods estimating the position of the target.

depth of 300 m. Although they could not pinpoint the exact location of the target, both the least-squares and the weighted average methods improved on the result obtained by simply averaging the points. The least-squares solution overestimated the depth more than the weighted average solution. Thus the weighted average method was used in subsequent analysis of other data. One of the reasons that could explain the failure to exactly pinpoint the target location was the way peaks of the mainlobe in the array responses were picked.

An automated program for picking incidence angles corresponding to the peak of the mainlobe was not developed or included in the algorithm. Such an algorithm might introduce bias in the estimate of position of the mainlobe. The program would pick the highest value regardless of where it lies on the beam. The highest point on the beam power pattern is expected to lie in the middle of the mainlobe. The following example (fig 4.13) indicates how difficult it would be to choose this point. Because of this problem, handpicking the position of the mainlobe which focused at the centre was used.

(a)   (b)   (c)
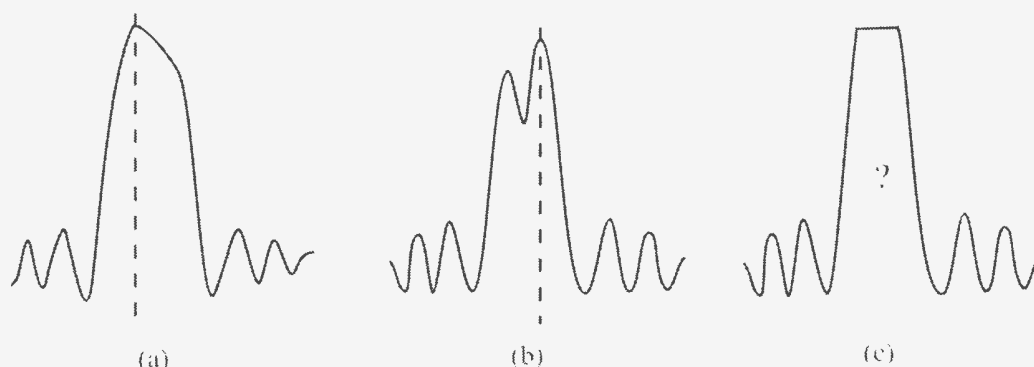
Figure 4.13
Schematic showing bias in the estimation of the position of the mainlobe. The peak of the beam should be in the middle of the mainlobe.

b. Source offset from the scatterer which is at the center of the array

The model used in this analysis is shown in figure 4.14 (a). The scatterer is located at a depth of 300 m as in the above investigation. The source is put at a location 200 m away from a point directly above the scatterer. All other design parameters are the same as in the model used in example **a** above. A few minor changes were introduced to the program *center_css.m* and it was renamed *soffset_nc.m*. This new program was used in this investigation. The changes made are shown in Appendix C. Figure 4.14 (b) shows diffraction traveltime curve for this model (i.e., model in fig. 4.14 (a)). Note again that part of the direct wave has been muted out to enhance visualization of the low energy diffraction hyperbola. The array responses are shown in figure 4.15. The incidence angles corresponding to the location of the mainlobes in each segment are displayed in table 4.3. As in the above model, the incidence angles were used together to generate raypaths (fig. 4.16) that were back-projected to their origin. A plot was then generated of
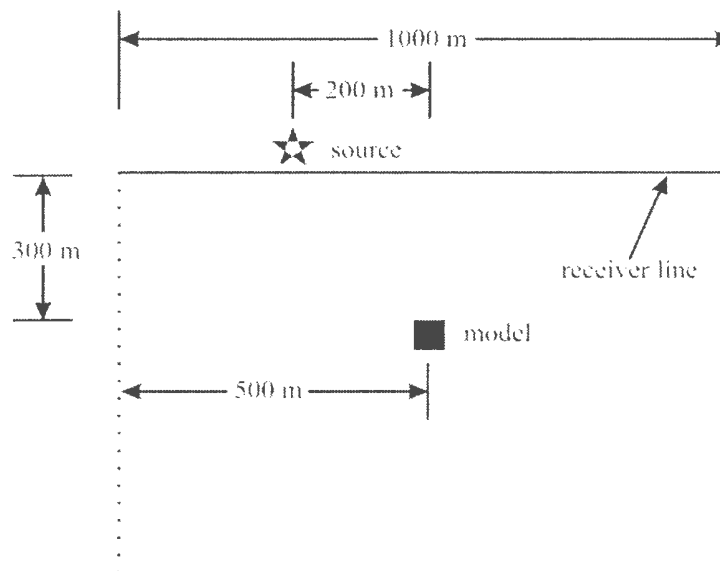
Figure 4.14: *(a)*
Geological model showing the source offset from the scatterer.

Table 4.3: *Incidence angles obtained from the data with source offset from the scatterer. The scatterer is at the center of the array.*

Segment number	k_x	φ (degrees)
1	0.0573	46.85004
2	0.0569	46.42505
3	0.0531	42.53887
4	0.0474	37.1221
5	0.0449	34.86778
6	0.04	30.61694
7	0.0367	27.85781
8	0.0326	24.52411
9	0.0244	18.09964
10	0.0163	11.97811
11	0	0
12	-0.0153	-11.2334
13	-0.0244	-18.0996
14	-0.034	-25.6518
15	-0.0406	-31.1269
16	-0.0486	-38.2281
17	-0.0531	-42.5389
18	-0.0579	-47.4939
19	-0.0612	-51.1895
20	-0.0653	-56.2454
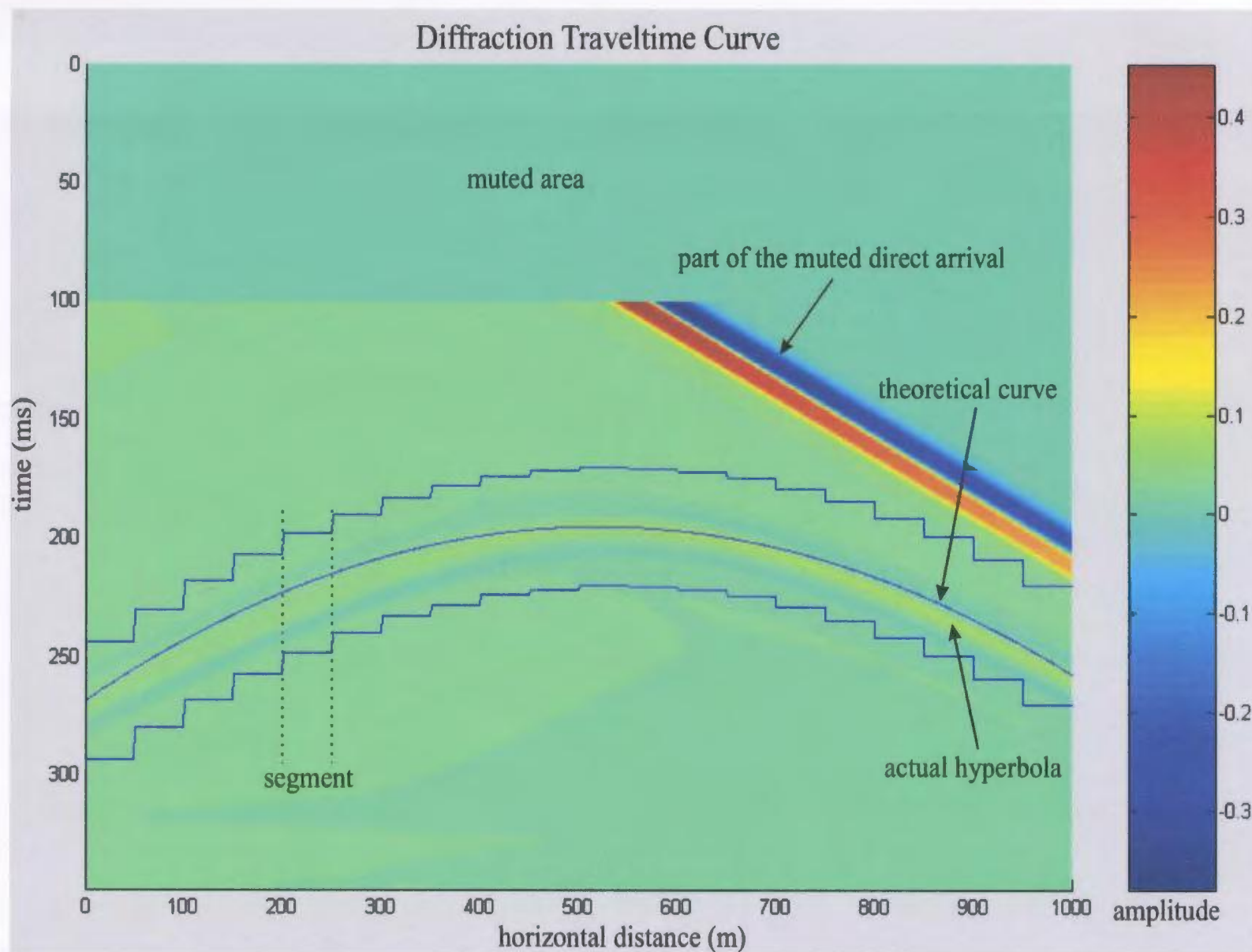
Figure 4.14: *(b)*
Diffraction traveltime curve for a source offset from a scatterer, i.e., for the model in figure 4.14 (a).
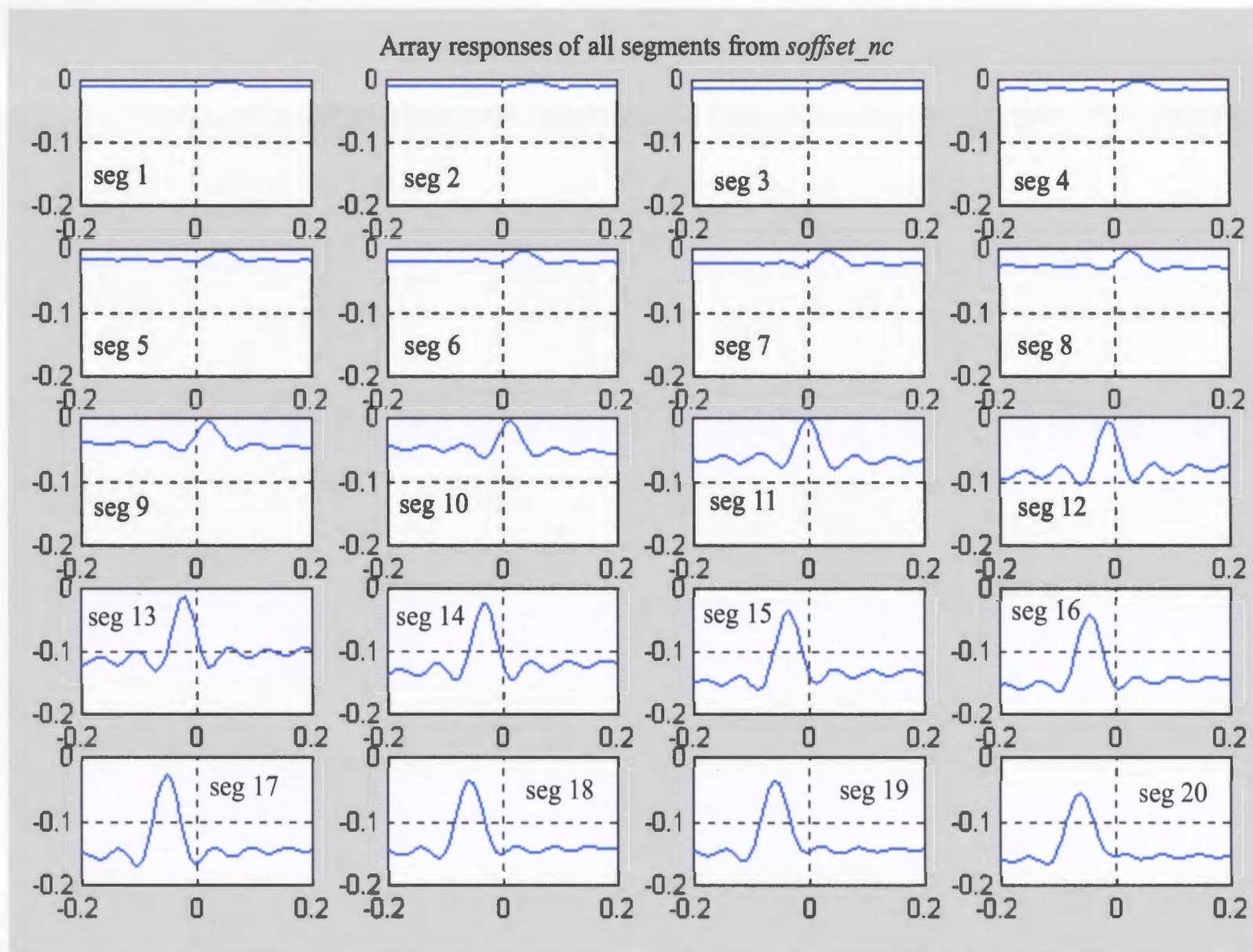
Figure 4.15: *Array responses from soffset_nc.m*

Depth vs hozizontal distance
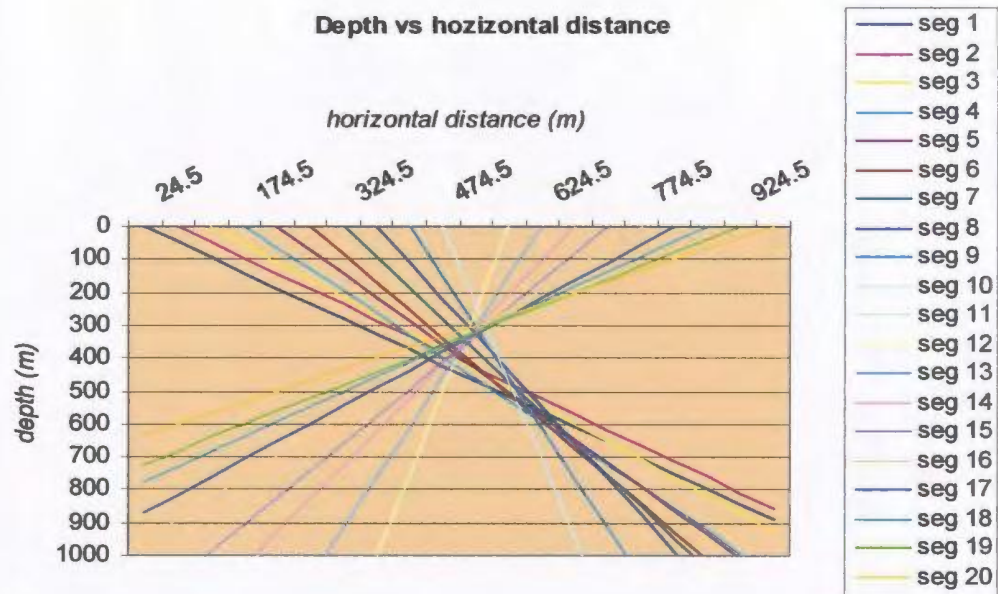
Figure 4.16
Raypaths from data with source offset from scatterer projected back to a common point of origin.
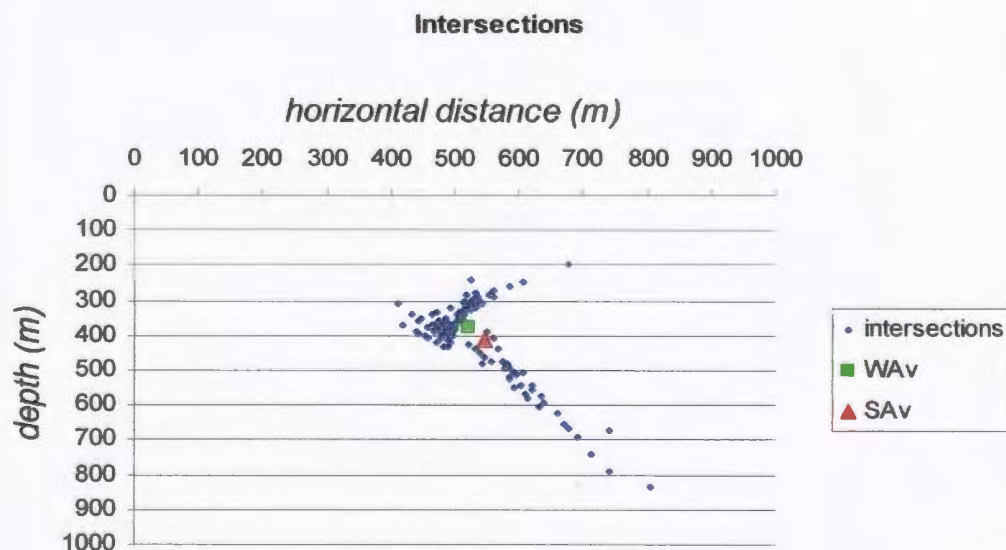
Intersections

Figure 4.17
Intersection points of raypaths with the solutions from simple average (SAv) and weighted average (WAv) methods estimating the position of the target.

Table 4.4: *Location estimates for the scatterer at the center of array with the source offset 200 m from a point directly above it. The scatterer's horizontal distance is measured with respect to the source position.*

	Actual location of the scatterer	Position of the source	Simple average solution	Weighted average	
				Starting location	Weighted solution
Horizontal distance x (m)	200	300	245	177	220
Depth z (m)	300	0	410	370	382

all possible intersections among the raypaths displayed in figure 4.17. The position of the target was first estimated by simply taking the average of all intersections. This position was computed as a horizontal distance of 245 m from the source position toward the center of the array and a depth of 410 m. An improvement on this point was obtained by taking a weighted average of all the intersections using an initial location of 177 m from the source position toward the center of the array and a depth of 370 m. Once again, the weighted average was performed by assigning least weights to points furthest from the starting point. The closest point was assigned a value of 1. The starting point was chosen from the area where points seemed to be concentrated. A location of 220 m and a depth 382 m was obtained using the weighted average technique. Changing the starting value changes the output very slightly. For example, instead of using 177 m and a depth of 370 m, one could use a distance of 232 m from the point directly above the scatterer and a depth of 298 m to get an output of 220 m and a depth of 378 m. Figure 4.17 also displays

the position of the scatterer estimated by simply taking the average of all intersections and by using a weighted average. The results of this investigation are summarized in table 4.4.

An observation made is that the results in the above two examples demonstrate that the beamformer's ability to pinpoint the location of the scatterer is degraded as the source moves away from the scatterer. With this simple beamformer, it is difficult to tell exactly where the source (generator of seismic energy) is located. Thus, one has to know the source position which is the case in most seismic explorations. The beamformer focuses only on the diffraction hyperbola not the entire wavefield.

c. Source and scatterer coincident and at the end of the array

Another model, displayed in figure 4.18, was investigated where the source and the scatterer were coincident and at the other end of the array. The scatterer was at a depth of 300 m. Data were generated in Seismic Unix® using the following design parameters:
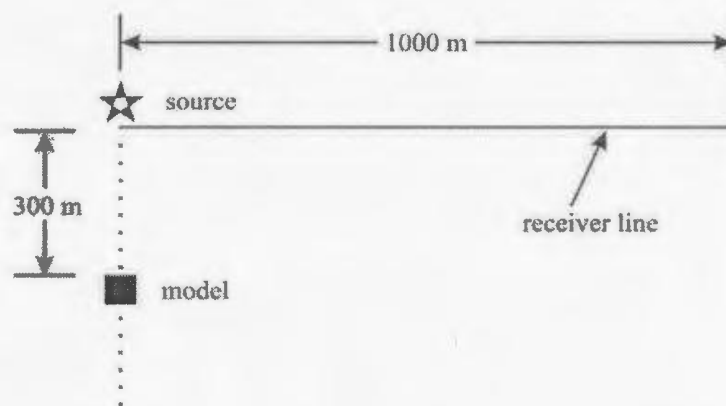
Figure 4.18
A geometry showing coincident source and scatterer at the other end of the array.

Table 4.5: *Incidence angles obtained from the data with source and scatter coincident and at one end of the array.*

Segment number	k_x	φ (degrees)
1	-0.003	-2.18907
2	-0.008	-5.84624
3	-0.016	-11.7545
4	-0.02	-14.7527
5	-0.029	-21.6687
6	-0.033	-24.8453
7	-0.044	-34.0714
8	-0.045	-34.9567
9	-0.05	-39.5402
10	-0.055	-44.4496
11	-0.053	-42.4399
12	-0.065	-55.8536
13	-0.065	-55.8536
14	-0.065	-55.8536
15	-0.065	-55.8536
16	-0.069	-61.4662
17	-0.069	-61.4662
18	-0.065	-55.8536
19	-0.061	-50.9572
20	-0.069	-61.4662
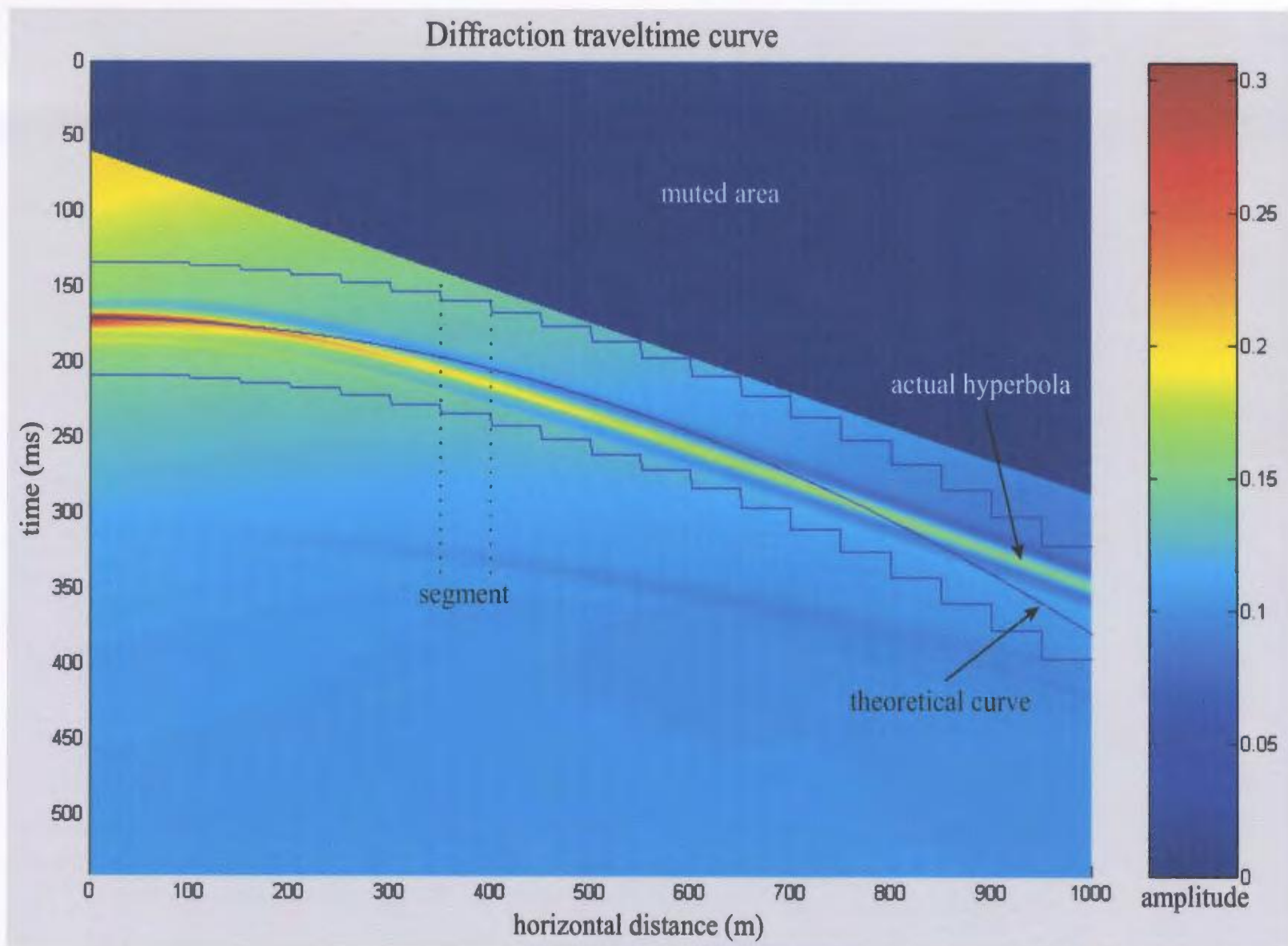
Figure 4.19
Diffraction traveltime curve for a coincident source and scatterer at the end of the array.
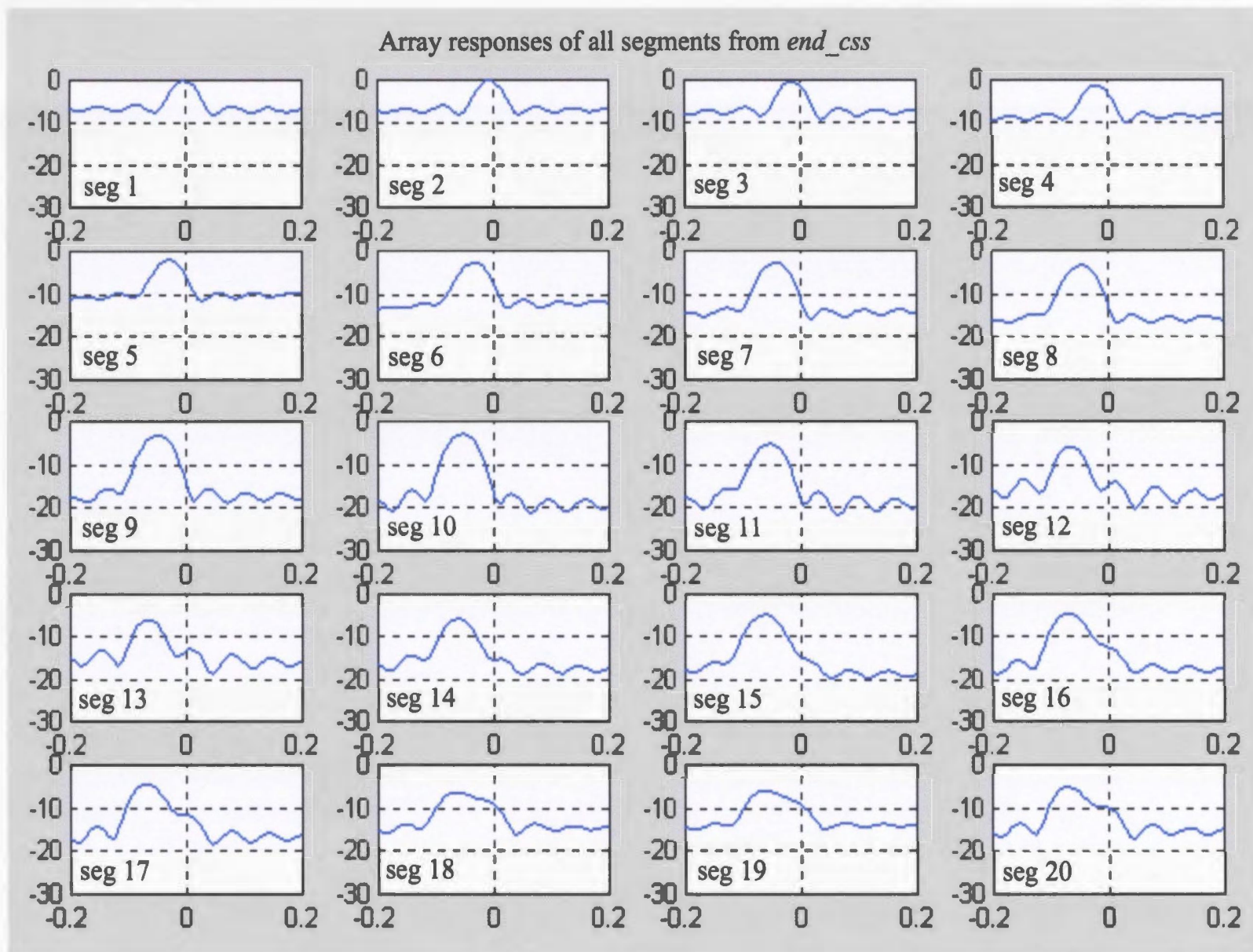
Figure 4.20: *Array responses from end_css.m*

Depth vs. horizontal distance

Legend:
- seg 1
- seg 2
- seg 3
- seg 4
- seg 5
- seg 6
- seg 7
- seg 8
- seg 9
- seg 10
- seg 11
- seg 12
- seg 13
- seg 14
- seg 15
- seg 16
- seg 17
- seg 18
- seg 19
- seg 20
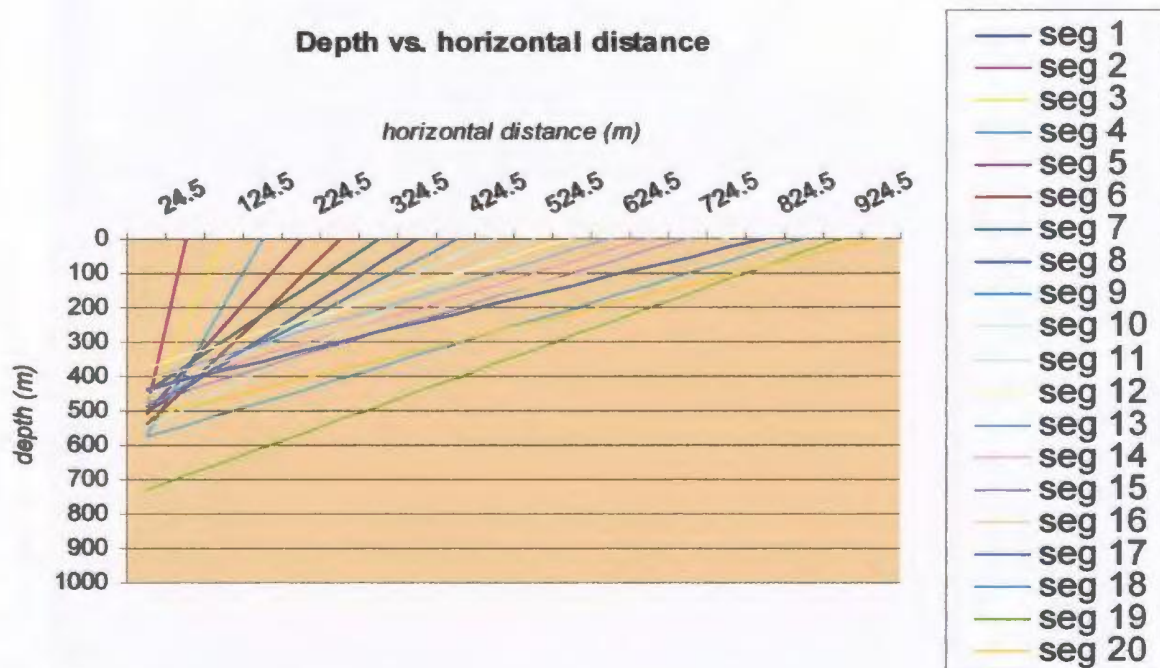
Figure 4.21
Raypaths projected back to a common point of origin from the data with source and scatterer coincident and at one end of the array.
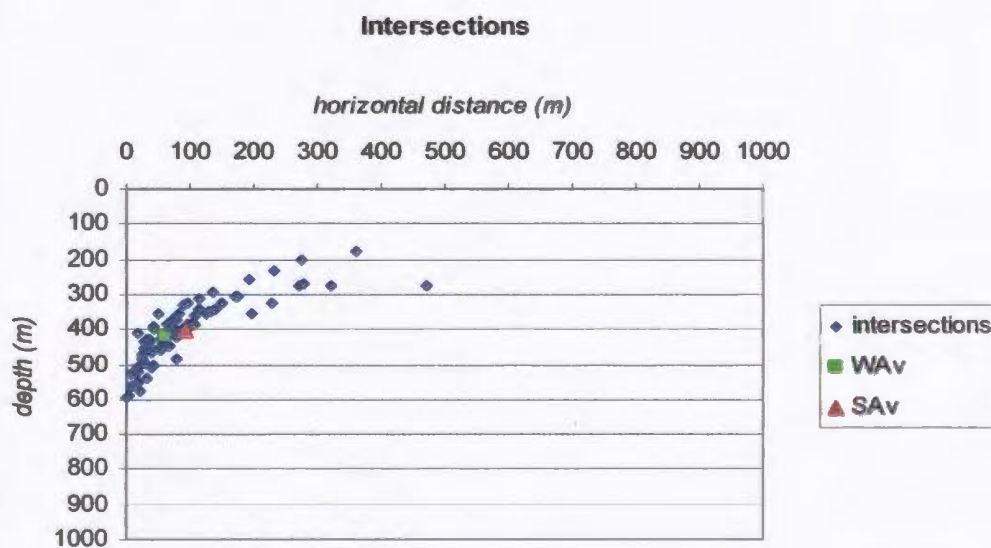
Intersections

Figure 4.22
Intersection points of raypaths with the solutions from simple average (SAv) and weighted average (WAv) methods estimating the position of the target.

Sample rate, $\Delta t = f_s^{-1} = 0.0005$ s
Dominant frequency, $f_D = 50$ Hz
Propagation velocity, $v = 4000$ m/s
Depth, $z = 300$ m
Number of receivers, $M = 1000$
Number of time samples, $N = 1100$
Receiver spacing, $d = 1$ m

Figure 4.19 shows the data generated using the above design parameters; the figure also shows how the diffraction hyperbola was segmented. The goal of using the theoretical curve was not to match it exactly to the diffraction curve generated but it was only used as a guide for the segmentation process. Twenty segments of size 50 receivers by 150 time samples were generated. The segments were then prepared for beamforming and then run through the beamforming procedure. The main program, *center_scc.m*, was slightly modified to create a new one, *end_css.m*, for this investigation. The minor changes made are shown in Appendix C. Figure 4.20 shows array responses obtained from the segments generated from the model. These segments were beamformed individually to get incidence angles of the incoming wavefront. The incidence angles corresponding to the mainlobe in each segment are shown in table 4.5. The negative sign in front of the incident angles indicate that the wavefront arrives at the array from the southwest quadrant as illustrated in figure 2.6 (signal *b*). A ray diagram was immediately generated using the incidence angles in table 4.5. The raypaths are displayed in figure 4.21. A careful observation indicates that segments close to the source do intersect while those that are furthest away from the source, e.g., the last three segments do not. Looking at figure 4.19 above one could understand why this is the case. These segments occupy the widest aperture (close to sixty degrees) and they don't have a good resolution. The

intersections among the segments are shown in figure 4.22. A simple average of the intersection points estimated the location of the scatterer at a horizontal distance $x = 93$ m and a depth $z = 405$ m. This position is shown in figure 4.22 by a red triangle. A weighted average was also calculated to estimate the location of the scatterer using an initial point of 0 m from the source and a depth of 400 m. The estimated location was determined as 60 m from the source and a depth of 421 m. The weighted average technique overestimated the depth of the scatterer more than the simple average method, but it brought the horizontal distance closer to the location of the scatterer. Table 4.6 summarizes the main results obtained using the model in figure 4.18.

Table 4.6: *Location estimates for the scatterer coincident with the source and at one end of the array.*

	Actual location of the scatterer	Position of the source	Simple average solution	Weighted average	
				Starting location	Weighted solution
Horizontal distance x (m)	0	0	93	12	60
Depth z (m)	300	0	405	200	421

d. Source at the center and scatterer at one end of the array

In this example the source was placed at the center of the array and the scatterer was placed directly below the first receiver in the array and at a depth of 300m. The geometry of this configuration is displayed in figure 4.23. The same design parameters as in
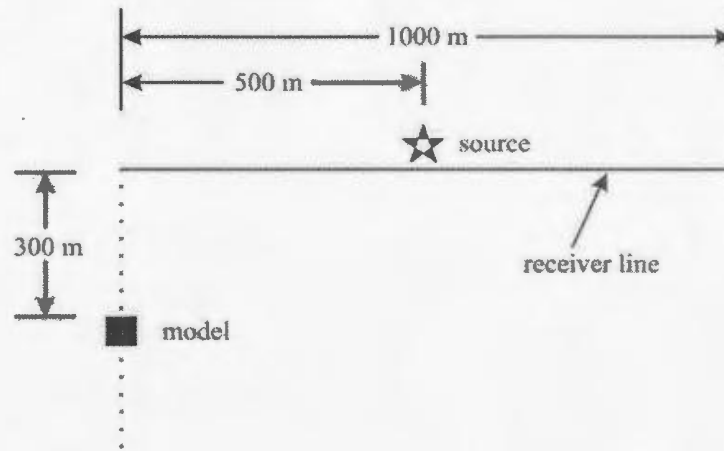
Figure 4.23
The geometry of the source at the center and the scatterer at one end of the array.

Table 4.7: *Incidence angles obtained from the data with source at the center and the scatterer at one end of the array.*

Segment number	k_x	φ (degrees)
1	0	0
2	-0.008	-5.84624
3	-0.02	-14.7527
4	-0.029	-21.6687
5	-0.037	-28.1056
6	-0.041	-31.4684
7	-0.045	-34.9567
8	-0.05	-39.5402
9	-0.05	-39.5402
10	-0.045	-34.9567
11	-0.05	-39.5402
12	-0.05	-39.5402
13	-0.052	-41.459
14	-0.045	-34.9567
15	-0.05	-39.5402
16	-0.057	-46.531
17	-0.052	-41.459
18	-0.053	-42.4399
19	-0.055	-44.4496
20	-0.057	-46.531
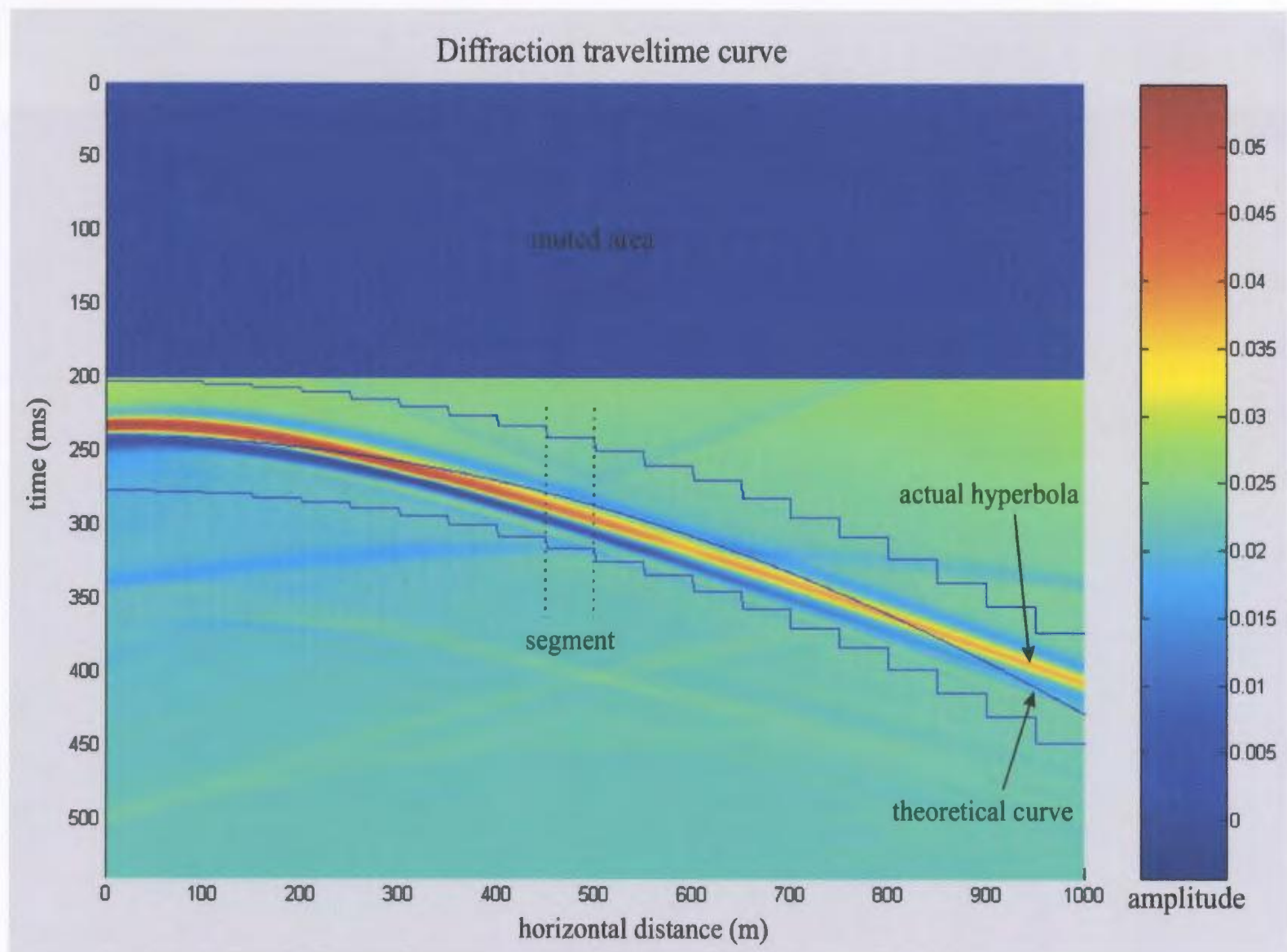
Figure 4.24
Diffraction traveltime curve for a source at the center and scatterer at one end of the array.
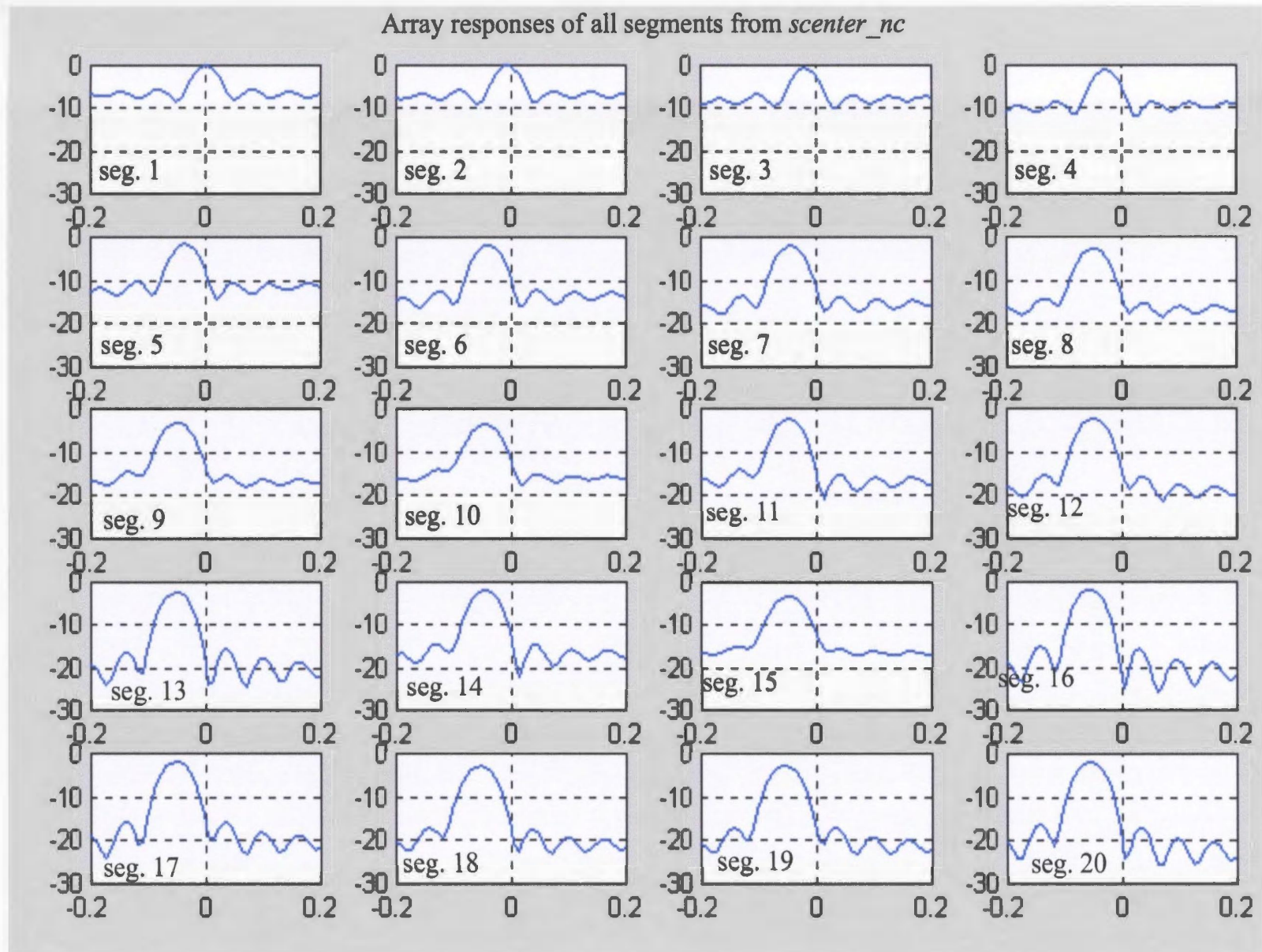
Figure 4.25: *Array responses from scenter_nc.m*
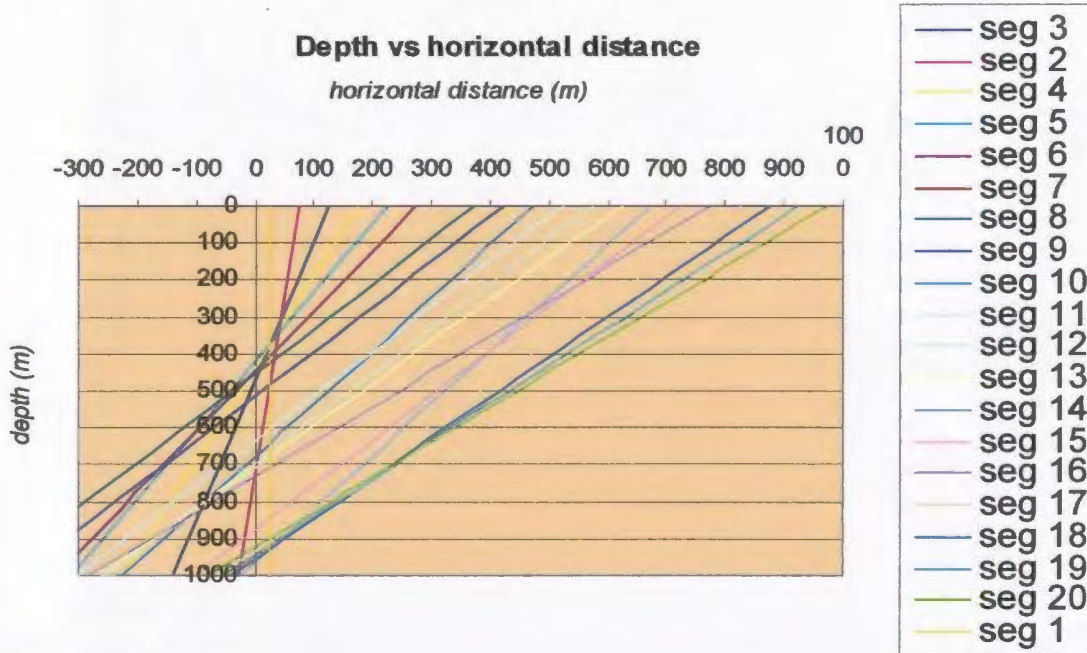
Figure 4.26
Raypaths projected back to a common point of origin from the data with source at the center and scatterer at one end of the array.

example **c** above were used to generate the data, i.e.,

Sample rate, $\Delta t = f_s^{-1} = 0.0005$ s
Dominant frequency, $f_D = 50$ Hz
Propagation velocity, $v = 4000$ m/s
Depth, $z = 300$ m
Number of receivers, $M = 1000$
Number of time samples, $N = 1100$
Receiver spacing, $d = 1$ m

The data was generated using Seismic Unix® data processing software. Figure 4.24 shows

the data record generated. The figure also shows how the segmentation was done. The

hyperbola was segmented into twenty segments of size 50 receivers by 150 time samples.

Each segment was prepared for beamforming and the beamforming process was carried

out on each segment individually. Program *scenter_nc.m*, created after making a few

changes to the main program *center_css.m*, was used for this investigation. The changes

made are recorded in Appendix C. Figure 4.25 shows array responses of the segments

plotted together. Incidence angles corresponding to the mainlobe in each segment were

determined and recorded in table 4.7. These angles of approach of the diffraction

wavefront were then used to construct a ray diagram which is shown in figure 4.26. As

can be seen in the figure the first six segments do intersect. The later segments which

contain part of the hyperbola at very wide angles do not intersect with the first segments

or among themselves. Later segments are almost parallel to each other and it is difficult

to use them to locate the scatterer.

The intersections among the segments are plotted in figure 4.27. It can be seen

clearly here that the later segments do not seem to intersect with the first six segments
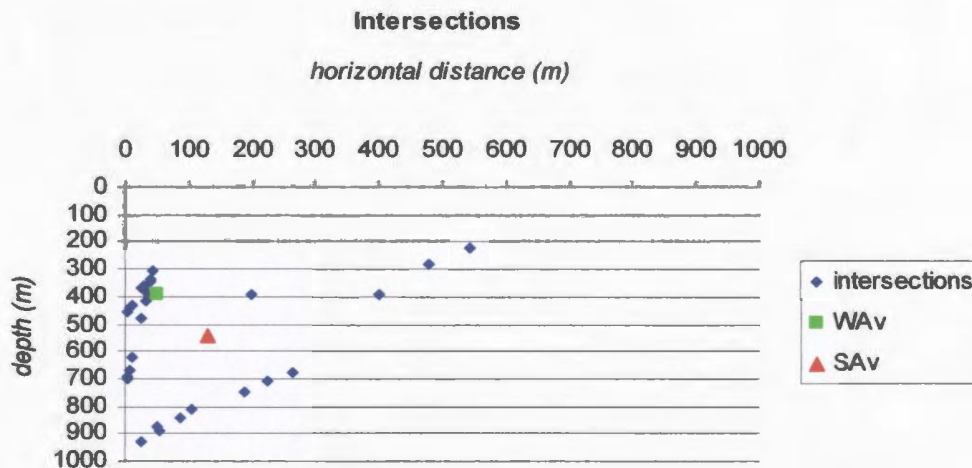
Figure 4.27
Intersection points of raypaths with the solutions from simple average (SAv) and
weighted average (WAv) methods estimating the position of the target.

which means they cannot locate the scatterer very well. They have almost the same angle

of incidence and hence are parallel. To be able to locate the scatterer all segments should

have different directions of arrival. The simple average for this example was determined

to be 129 m away from a point directly above the scatterer and a depth of 542 m while the weighted average was found to be 50 m away and at a depth of 396 m using initial position of 12 m away from a point directly above the scatterer and a depth of 200 m (refer to table 4.8). The weighted average improved on the simple average but the depth was still overestimated.

Table 4.8: *Location estimates for the scatterer at one end of the array and the source at the center of the array. The source position in the x-direction is measured relative to that of the scatterer.*

	Actual location of the scatterer	Position of the source	Simple average solution	Weighted average	
				Starting location	Weighted solution
Horizontal distance x (m)	0	500	129	12	50
Depth z (m)	300	0	542	200	396

4.2.3 Noise analysis

This section investigates the response of the beamformer to different noise environments. The same data which was used in example **a** (section 4.2.2) for the determination of incidence angles was subjected to signal-to-noise ratios (SNR's) of 0.5, 1, 2, 3, 4, 5, 6, 10, 15 and 20. The noise simulation was performed in Seismic Unix® processing software using a program called SUADDNOISE. This program computes the noise using the value of the absolute maximum for the dataset as a whole. There is currently no trace-by-trace

noise computation option in the software package. The output is computed by adding a scaled noise with a Gaussian probability distribution to the signal, i.e.,

$$output = sig + scale \times noise, \text{ where } scale = \frac{abs\max(sig)/\sqrt{2}}{SNR\sqrt{energy\_per\_sample}}.$$ Figure 4.28

shows the diffraction travel time curve, for the data set shown previously in figure 4.3, with different noise simulations. At an SNR of 0.5, the diffraction hyperbola is not visible but is clearly seen from an SNR of 2 upwards.

All the data sets were then processed the same way as the original output data in example **a** (section 4.2.2). Each output was segmented and then beamformed. The main program, *center_css.m*, was used in this investigation. No changes were made except for the input data. Different data with various signal-to-noise ratios were used. It should be stressed again here that narrowband beamforming was performed on each segment since the data was sufficiently narrowband. An angle of incidence was determined from the wavenumber value that corresponded to the maximum power of the array response of each segment. The angles were then used together to determine a common point of origin of the wavefronts in each data set. This was carried out by generating raypaths for each individual segment. Intersections among raypaths were determined as well as the common point of intersection which was determined using a distance-weighting scheme already discussed in section 4.2.2. Beam power patterns obtained from data sets that had an SNR of less than 5 (i.e., those with SNR of 4, 3, and 2) had many maxima in their beam power responses. Thus, it was difficult to identify the mainlobe's position from these data sets. An example of this situation is displayed in figure 4.29 which are the
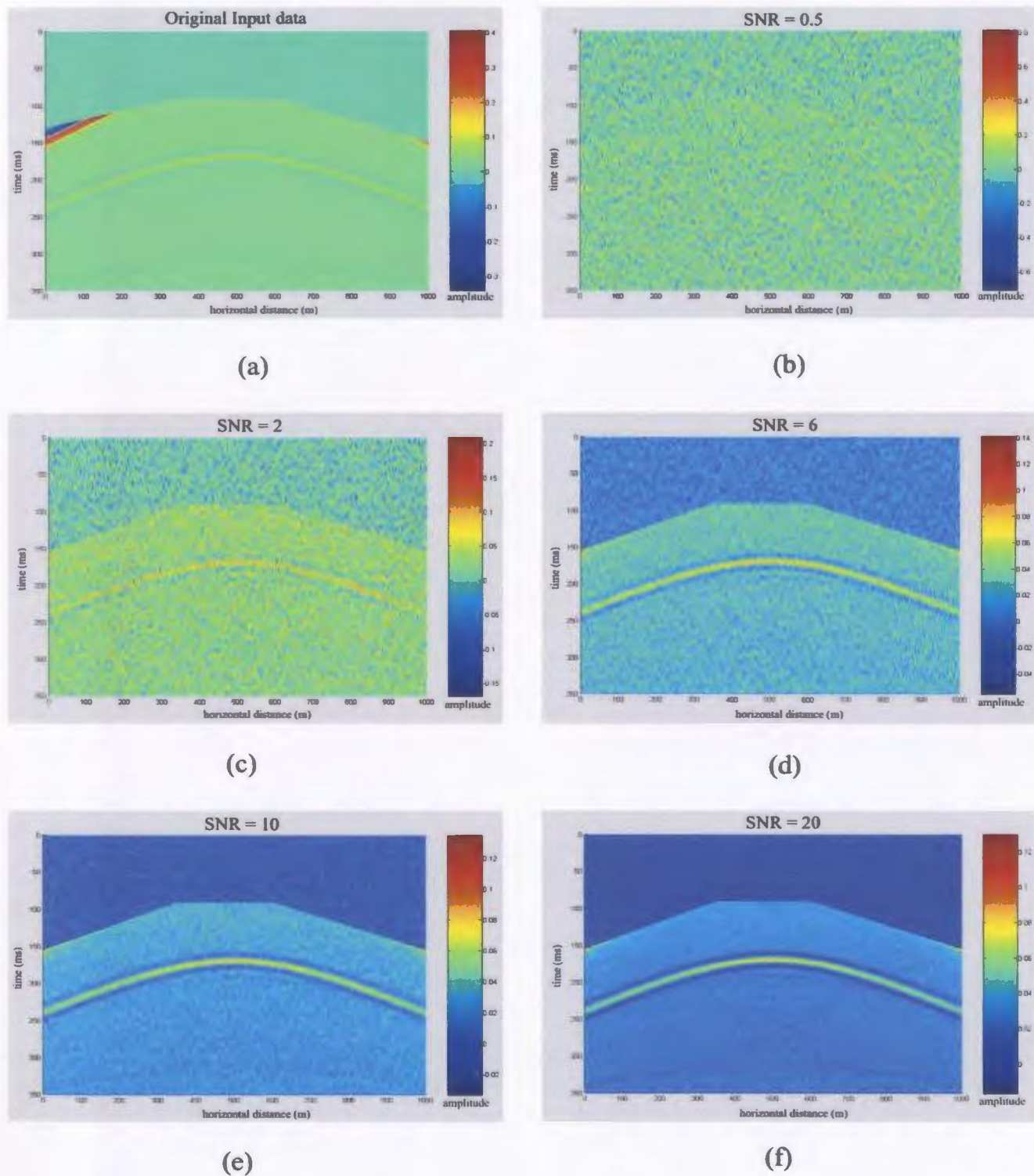
(a)

(b)

(c)

(d)

(e)

(f)

Figure 4.28
Noise simulations for a coincident source and scatterer. (a) shows the output from the original data set and the remaining diagrams indicate outputs with signal-to-noise (SNR) (b) 0.5, (c) 2, (d) 6, (e) 10 and (f) 20. The diffraction hyperbola is not visible at SNR of 0.5 and starts being visible at SNR of 2.

beam power responses of all segments from the data set with SNR of 4. It was relatively easy to determine the position of the mainlobe in the data sets which had an SNR equals to or greater than 5. Figure 4.30 shows the intersection points among raypaths and the common point of intersection obtained using the distance-weighting scheme for the data set with the SNR of 5. Although there was some scatter in the distribution of points, it was possible to estimate the depth and location of the target with respect to the horizontal axis of the array. By taking a simple average of the intersection points the depth of the target is estimated at about 371 m and at a horizontal distance of 511 m from the first receiver. Using a distance-weighting scheme with the starting point located at 488 m from the first receiver and at a depth of 338 m, the location of the scatterer is estimated at a 343 m depth and a distance of about 501 m away from the first receiver. Figure 4.31 (a), (b), (c) and (d) show results from data sets with signal-to-noise ratios 6, 10, 15 and 20, respectively. Table 4.9 shows the results from these data sets. The results show that with the noise added to the input data the beamformer still is able approximate the location of the scatterer to a few meters. The actual location as shown in the model for example **a** in section 4.2.2 is 500 m (middle of the array) and a 300 m depth. To improve on the solution using the simple average a weighted solution has been used and it has shown to improve the depth estimates significantly. The results also show that as the SNR improved the intersections became a little tighter or close together. But the depth estimate became poorer as we progress to the highest SNR. The tails that appear in the distribution of the intersection points have added some error into the results. The Gaussian weighting with zero mean was used to reduce this error. Although, the

Table 4.9: *Location estimates of the scatterer from data with signal-to-noise ratios 6, 10, 15 and 20. x represents horizontal distance from the first receiver and z represents the depth.*

	Simple Average (m)		Weighted Average			
			starting location (m)		weighted solution (m)	
	x	z	x	z	x	z
SNR 6	505	383	524	305	506	329
SNR 10	501	374	501	291	497	332
SNR 15	502	379	504	303	498	347
SNR 20	504	391	502	308	502	352

weighting has helped reduce the error significantly some error still remains. One error that might have contributed significantly to the results was the handpicking of the incident angles. As has already been explained in section 4.2.2, letting the program pick the peaks would have introduced bias in the estimates of the angles of arrival. The program could pick a peak regardless of where it lies with respect to the center of the mainlobe.

4.2.4 Decimation in space

The performance of the beamformer was also tested by using data decimated in space. The process of decimation involved killing every second trace, second and third trace, etc., in the data set. The muting was followed by casting the data into the frequency domain and then padding the data with a vector of (D-1) zeros, where D is the decimation
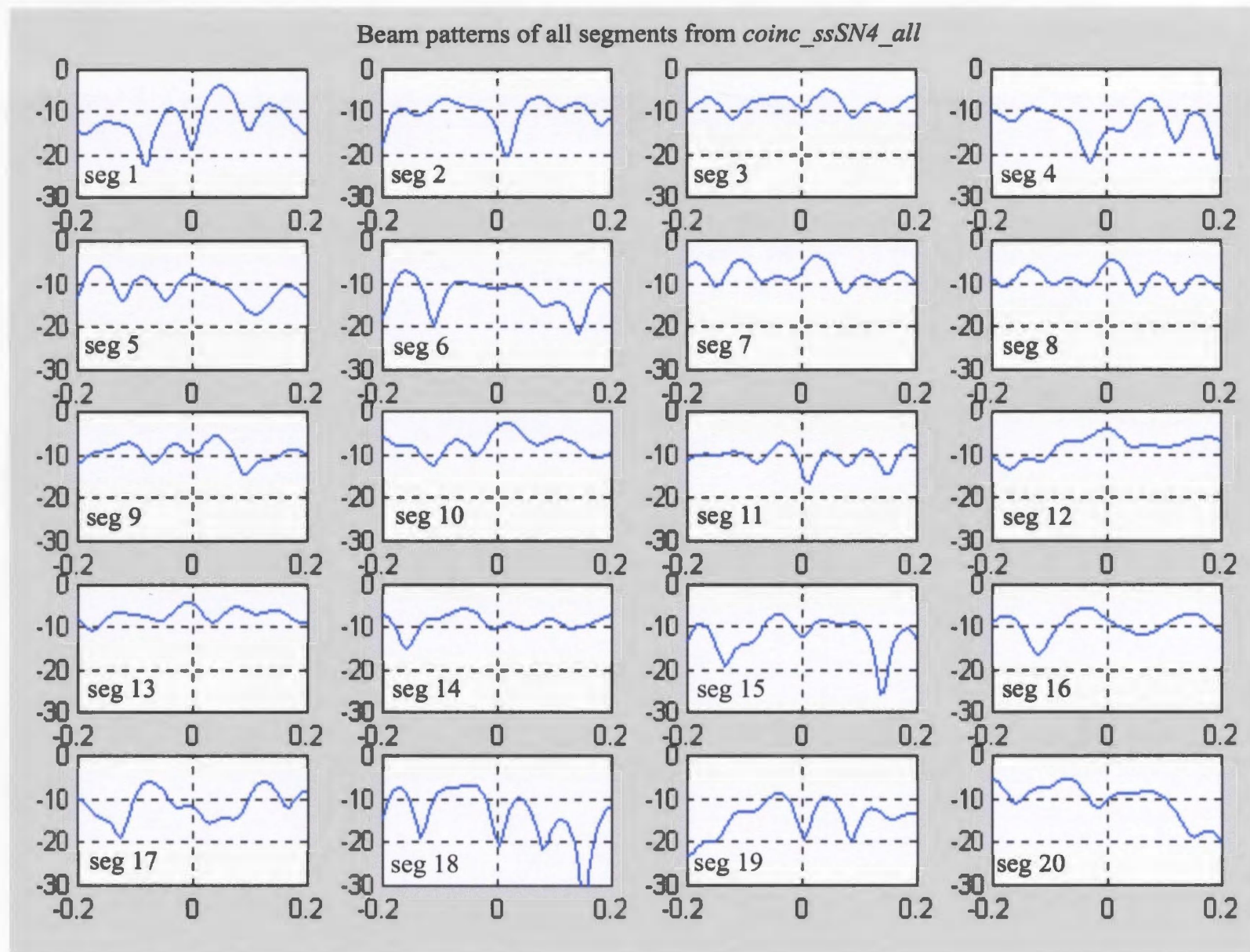
Figure 4.29: *Array responses from coinc_ssSN4_all.m*
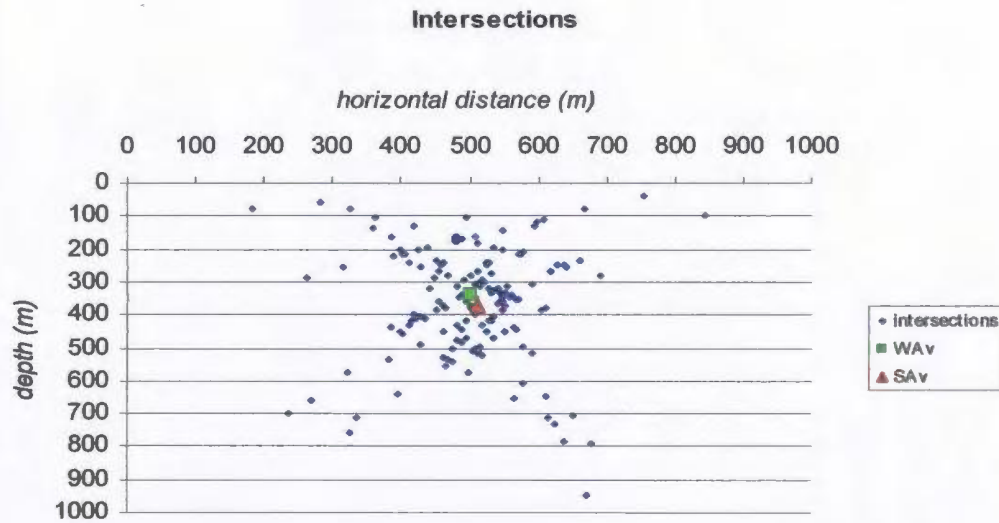
Figure 4.30
Intersection points of raypaths with the simple average (SAv) solution of (511 m, 371 m) and the weighted average solution (WAv) with coordinates (501 m, 343 m) for the data set with SNR of 5.
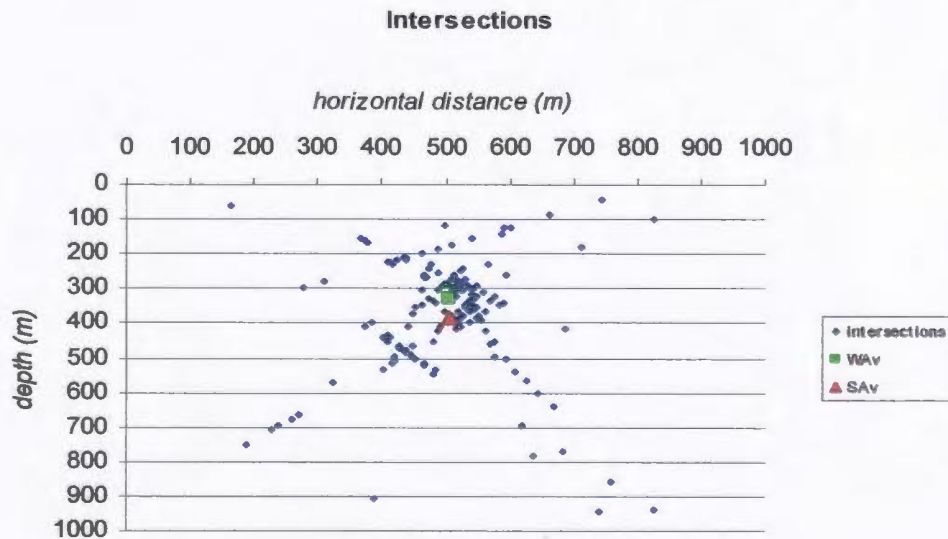
Figure 4.31: *(a)*
Results from the data set with SNR of 6. The SAv solution is (505 m, 383 m) while that from WAv is (506 m, 329 m). The WAv has significantly improved the depth estimate.
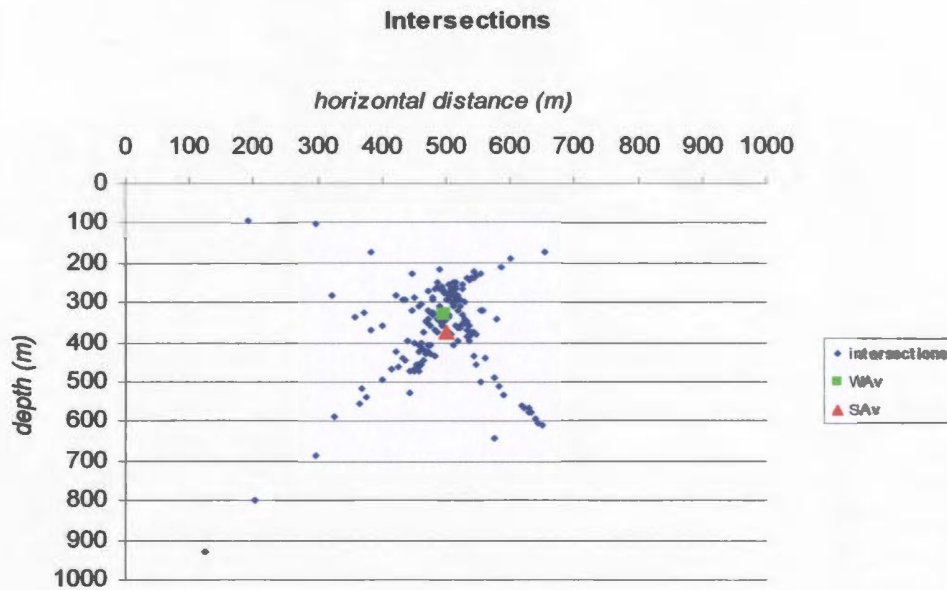
Figure 4.31: *(b)*
Results from the data set with SNR of 10. The SAv solution is (501 m, 374 m) while that from WAv is (497 m, 332 m).
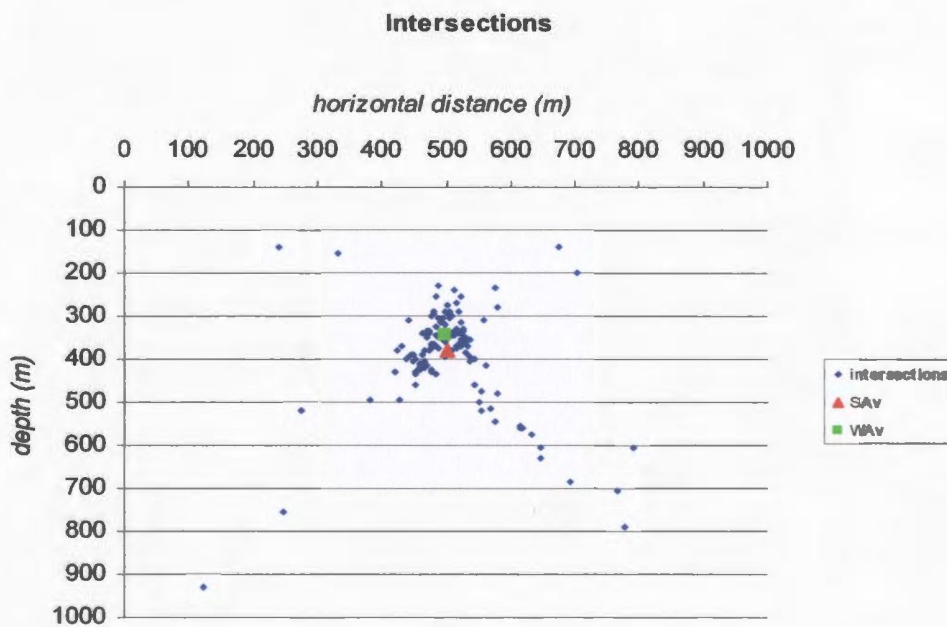
Figure 4.31: *(c)*
Results from the data set with SNR of 15. The SAv solution is (502 m, 379 m) while that from WAv is (498 m, 347 m).
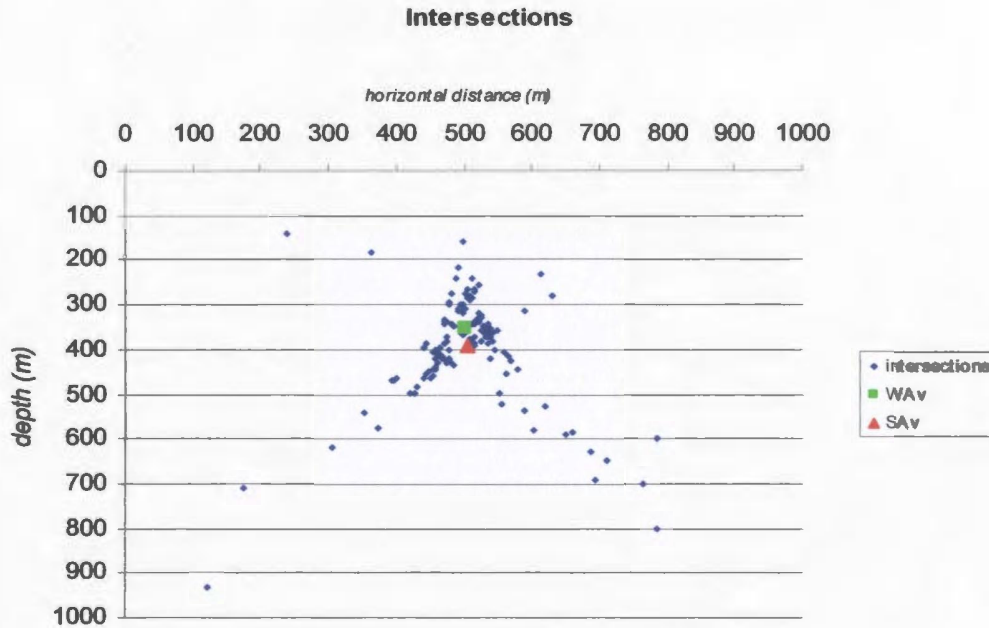
Figure 4.31: *(d)*
Results from the data set with SNR of 20. The SAv solution is (504 m, 391 m) while that from WAv is (502 m, 352 m).

factor. Decimation reduces the aperture of the array and hence widens the beam output

(see section 3.1.4). To counter this, interpolation by a factor of D was then used. This

interpolation process was performed in MATLAB® using a function called ***interpft***

which performed 1-D FFT interpolation along the spatial dimension. The data was then

transformed back to the time domain with the same number of samples as in the original

data set. Maintaining the same number of samples as in the original data set ensured that

a desired beam steering resolution was achieved. This, however, does not necessarily

improve precise estimation of the angle of emergence of the wavefronts.

A decimation factor of 10 (i.e., keeping every 10th trace and zeroing the other

nine) was first tried on the original data set that was shown in figure 4.3. Figure 4.32
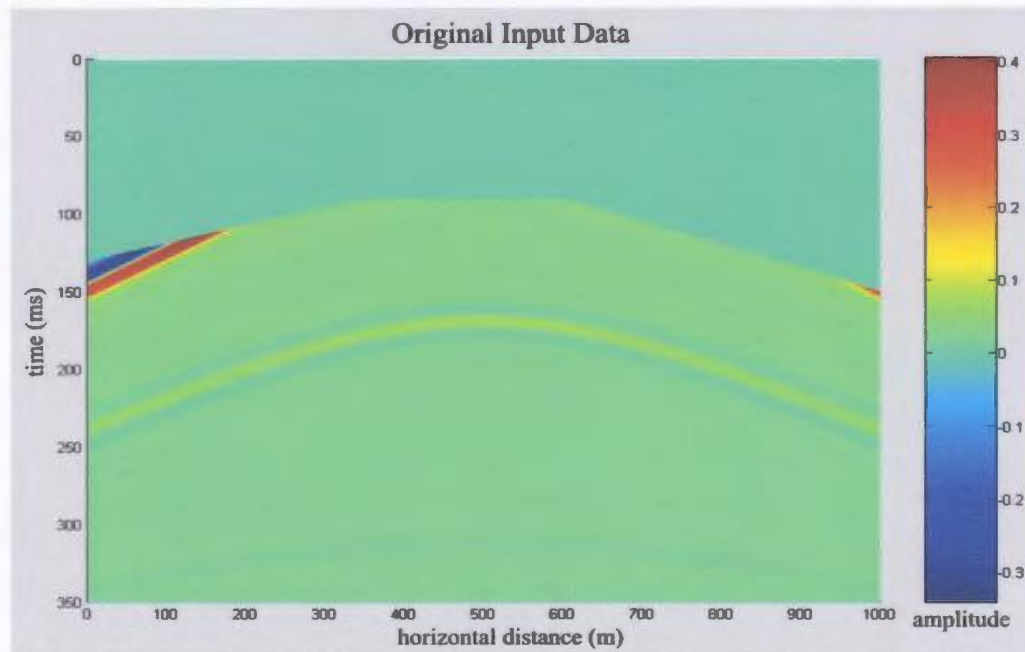
(a)
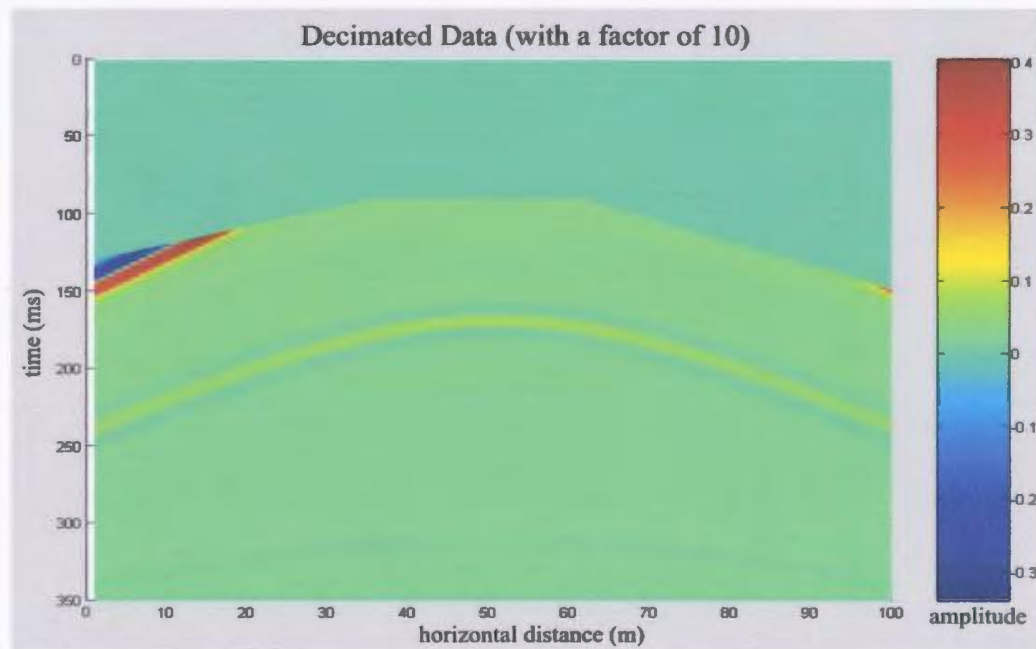
(b)

Figure 4.32
The result of decimating the data. The bottom panel (b) was resampled by keeping every tenth trace and zeroing the other nine. Trace spacing in the top (a) panel is 1 m while in the bottom one it is 10 m.

Figure 4.33
The procedure for determining the position of the target using decimated data. The decimated data is segmented, transformed to the Fourier domain and transformed back with more points. The resulting output is then beamformed to produce incidence angles which are then used to find the position of the target.
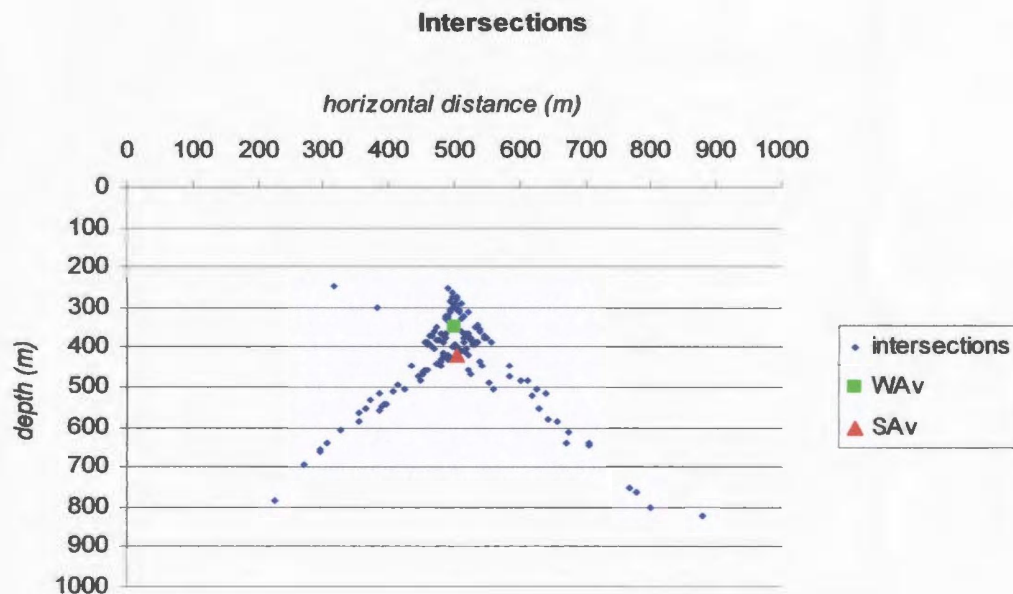
Figure 4.34
Intersection points of raypaths generated from data decimated with a factor of 10. The target has coordinates (502 m, 420 m) and (499 m, 348 m) from SAv and WAv, respectively.

shows the two data sets placed side by side. It is not immediately obvious to see that some of the traces have been omitted in figure 4.32 (b) because of the nature of the plot. But a closer look at it reveals some traces have been muted. The procedure followed before (i.e., segmentation, Fourier transformation and then beamforming) was used in

85

addition to interpolation. The program code, *center_cssDecF10.m*, for the process is shown in Appendix C. The procedure for finding angles of incidence was the same as before.

After finding the angles they were then projected back to a common point which would indicate the probable position of the target. Figure 4.33 shows in a flow diagram the procedure taken to find the probable position of the target. Figure 4.34 shows results obtained from the data decimated with a factor of 10. The results indicate the target has a horizontal distance of 499 m away from the first receiver and a depth of 348 m which are very close to that of the original data set of 501 m and 364 m. This indicates that with decimated data which has the same number of points as the original data set, the beamformer's performance is satisfactory. The original data set's results are used as a comparison even though they themselves were not accurate enough to pinpoint the actual position of the target.

Another test was done on a data set with a decimation factor of 20. The original and decimated data sets are shown in figure 4.35 for comparison. One can see clearly now because of the jagged nature of the diffraction hyperbola that some traces have been killed in the panel on the right. The procedure in figure 4.35 was then followed to find the incidence angles which were later used to locate the target. The results from the data set decimated with a factor of 20 are shown in figure 4.36. The processing results indicate a probable horizontal distance of 504 m away from the first receiver and a depth of 359 m. Compared with the original data's results, this is a slight improvement particularly in the

depth estimate. The original data set weighted average solution was a horizontal distance

of 501 m and a depth of 364 m. Table 4.10 is a summary of these results.

Table 4.10: *Location estimates from data decimated with factors of 10 and 20. The source is located at the center of the array. Like in section 4.2.2, the scatterer position is measured relative to the first receiver in the array while that of the source is measured relative to that of the scatterer.*

	Location of the scatterer from the original data set	Position of the source	Simple average solution	Weighted average	
				Starting location	Weighted solution
Decimation factor of 10	501	0	502	480	499
	364	0	420	200	348
Decimation factor of 20	501	0	504	505	504
	364	0	403	306	359

4.2.5 Location of more than one scatterer

The beamformer was also assessed on its ability to "see" two wavefronts impinging on

the array from different directions. The wavefronts should satisfy the Rayleigh criterion

for them to be resolved by the receiving array. Recalling section 3.1.4, the wavefronts'

directions of arrival should differ by more than $\Delta\varphi_{nn}/2$. The targets or scatterers which

are the sources of the wavefronts should at least be one Fresnel radius apart.

Two similar blocks of 60 x 50 m^2 each were placed at a depth of 300m. The receiver

array had the following design parameters; $\Delta t = f_s^{-1} = 0.0005$ s, $f_d = 50$ Hz, $v = 4000$ m/s,

$z = 300$ m, number of receivers $= 1000$ and receiver spacing $= 1$ m. Since the dominant

frequency of the waveform was 50 Hz, the Fresnel zone radius was calculated as 116.19

m. Thus, the models were placed 300 m apart along the axis of the array. The first

scatterer was placed at 325.5 m along the x-axis from the first receiver and the source

was placed between them directly above. Figure 4.37 shows the geometry of this

situation. Using this model, synthetic data was generated using Seismic Unix™ and the

diffraction hyperbolas can be seen in figure 4.38.

A new program, *twoscat_rm.m*, was created after making a few modifications to

the main program, *center_css.m*. The minor changes made are shown in Appendix C.

Figure 4.39 gives three examples of segments obtained from the data set shown in figure

4.38. The two wavefronts are clearly shown. Segments 1 and 20 are on the opposite ends

of the diffraction hyperbola. We expect the incidence angles of the two wavefronts to be

almost the same making them hard to be picked up by the beamformer. The beamformers

response should indicate a single mainlobe. This is indeed shown in figure 4.40 (a) and

(c). The eleventh segment which contains the two wavefronts at their maximum angular

separation does not show two distinct peaks even though the geometry satisfied the

Fresnel zone limitation. The angles may have been too close for the conventional

beamformer to resolve them.
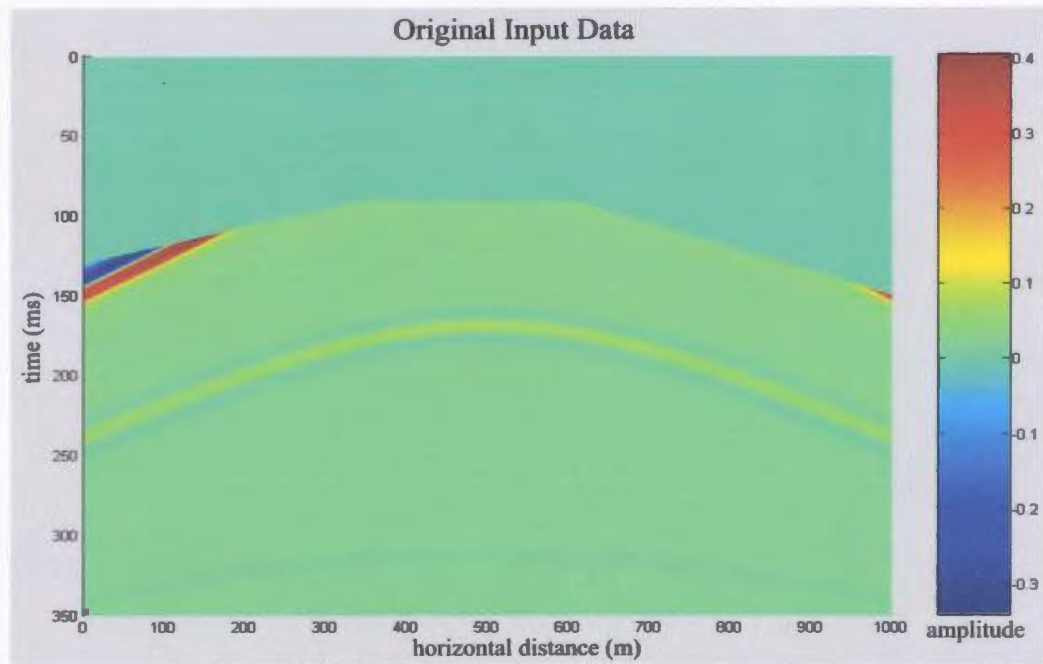
(a)
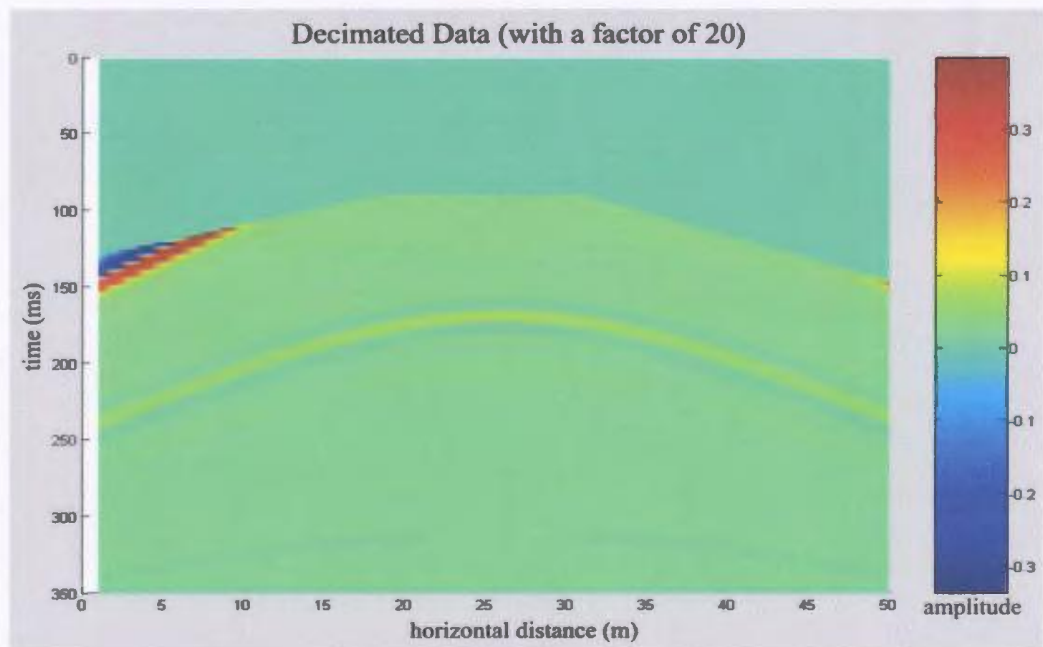
(b)

Figure 4.35
Decimation of the original data. The right panel was resampled by keeping every twentieth trace and zeroing the other nineteen. The resulting trace space is 20 m.

horizontal distance (m)
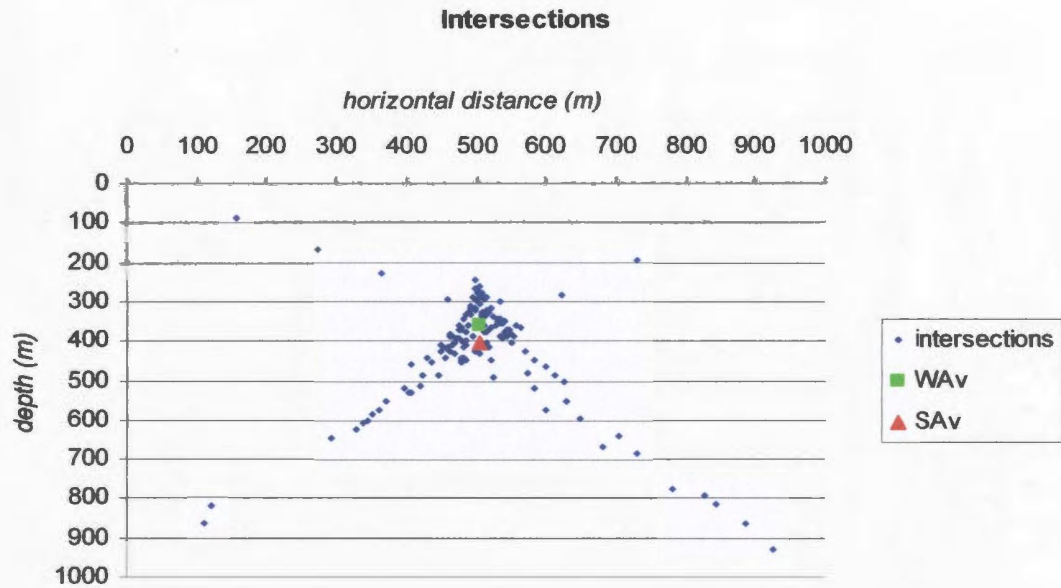
Figure 4.36
Intersection points of raypaths generated from data decimated with a factor of 20. The target has coordinates (504 m, 403 m) and (504 m, 359 m) from SAv and WAv, respectively.
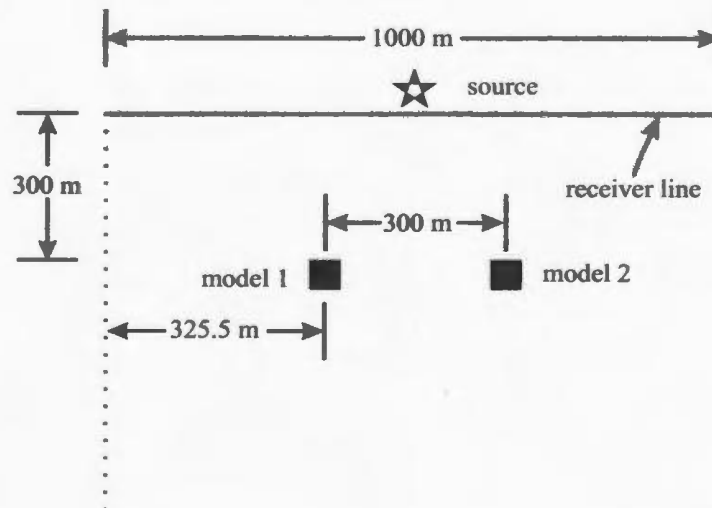
Figure 4.37
Geometry of two similar geological models representing adjacent massive sulfide deposits.
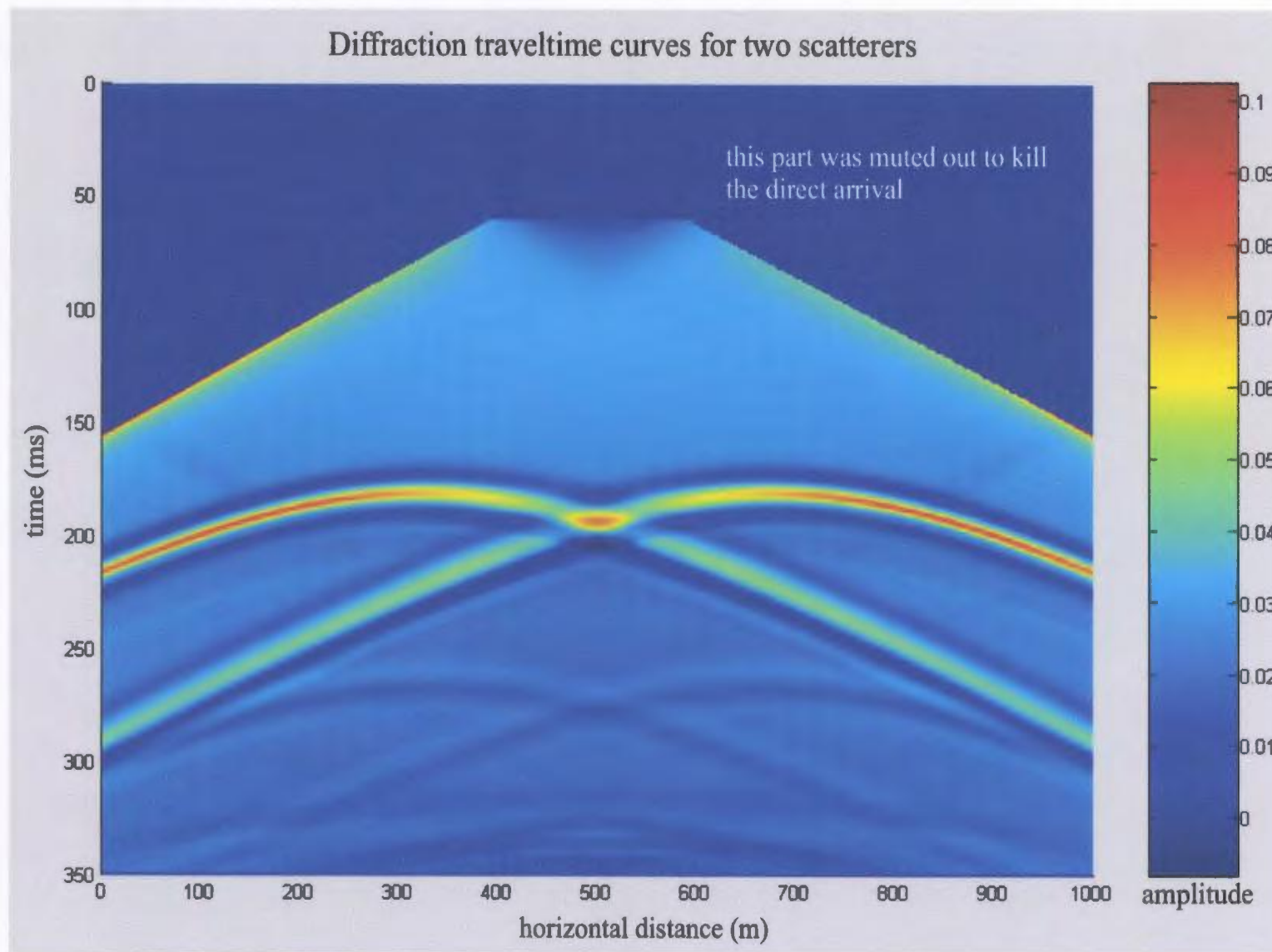
Figure 4.38
Diffraction travel time curves for adjacent scatterers or deposits. The scatterers are 300 m apart which is more than a Fresnel diameter apart.
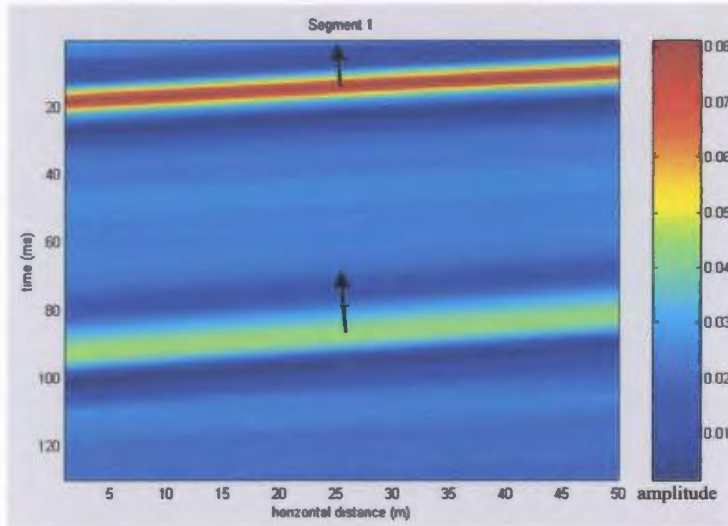
Figure 4.39

(a) *The first segment showing two wavefronts approaching the receiver array. The two waves are arriving at almost the same angle.*
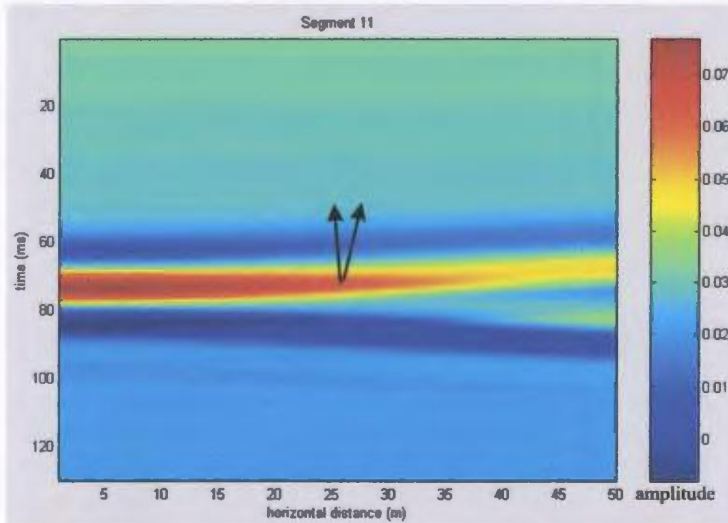
(b) *The eleventh segment showing the the point where the two wavefronts intersect. This is where there is maximum separation between their angles of incidence.*
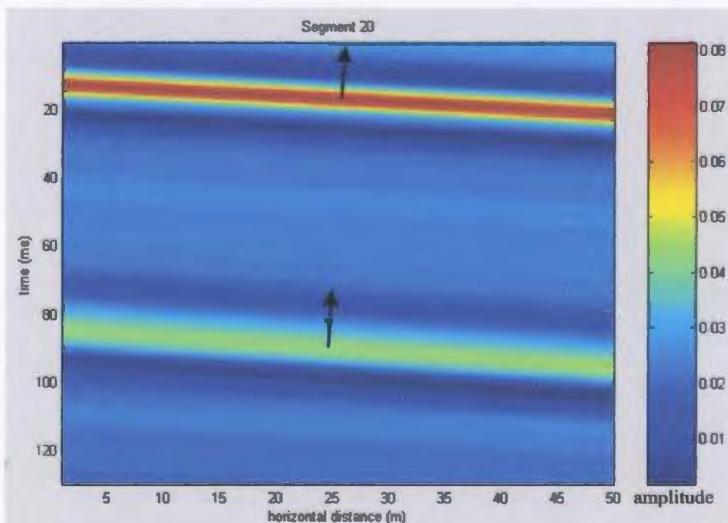
(c) *The twentieth segment showing the two wavefronts almost parallel to each other arriving at the receiver array.*
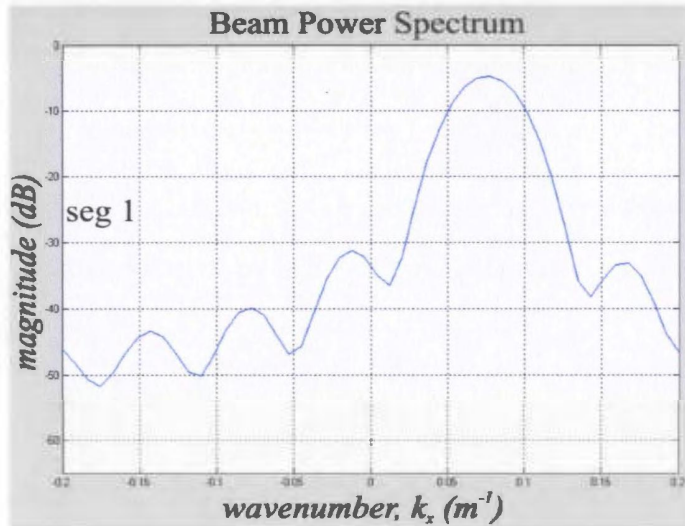
Figure 4.40
Location of two scatterers.
(*a*) *Beam power response of the first segment. Since the two wavefronts are almost parallel, the beamformer is not able to resolve them.*
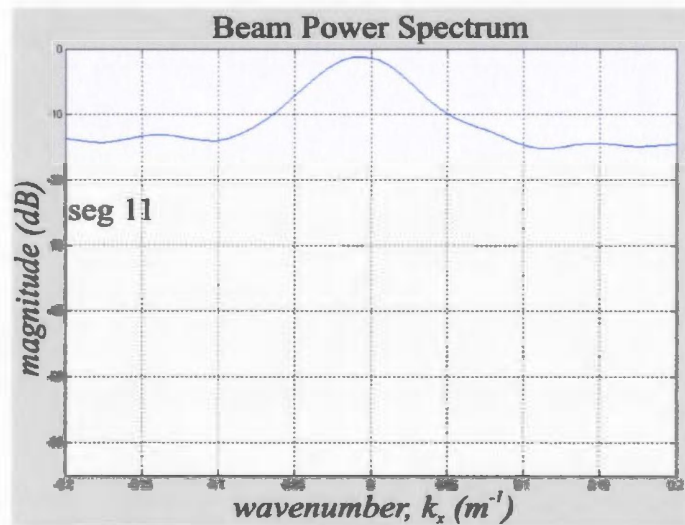
(*b*) *Beam power response of the eleventh segment. Although, the two wavefronts have a maximum separation between their angles of arrival, the beamformer could not resolve them.*
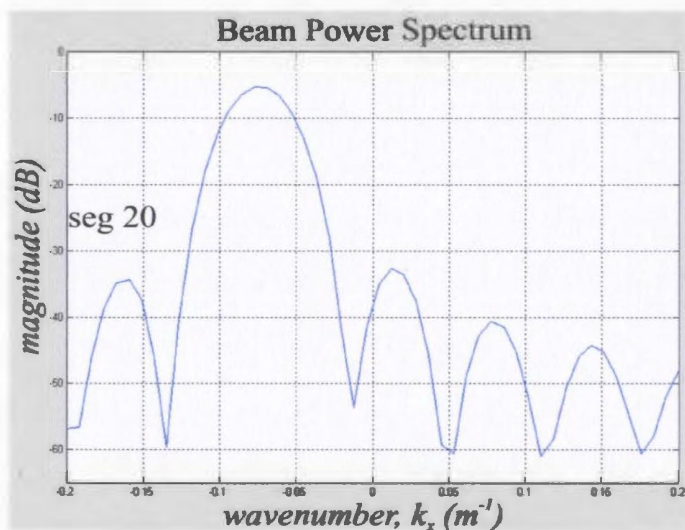
(*c*) *The wavefronts are almost parallel to each other as in (a) above, thus the beamformer "sees" them as one thing.*
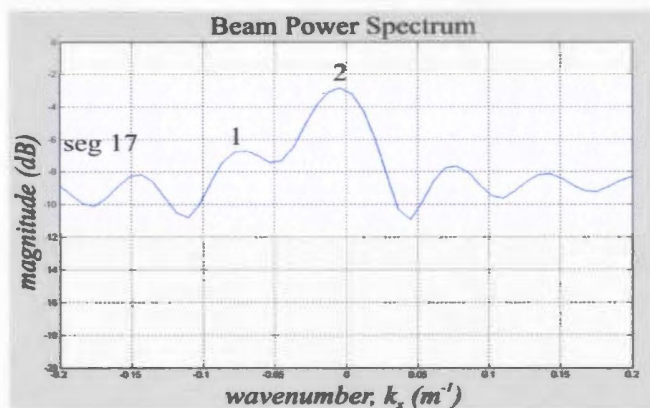
Figure 4.41
(*a*) *Segment 17 showing two distinct peaks marked 1 and 2.*
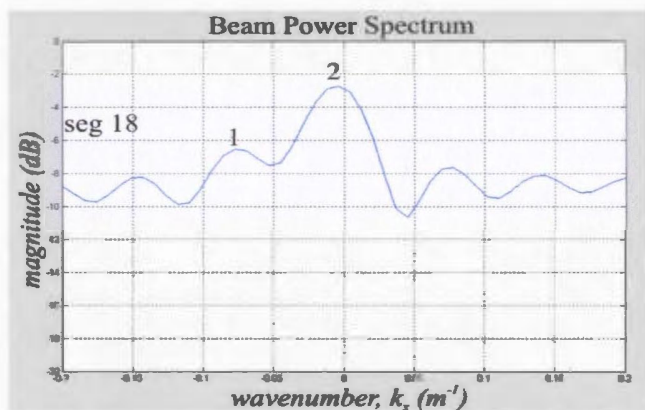
(*b*) The two wavefronts can still be picked by the beamformer in segment 18.
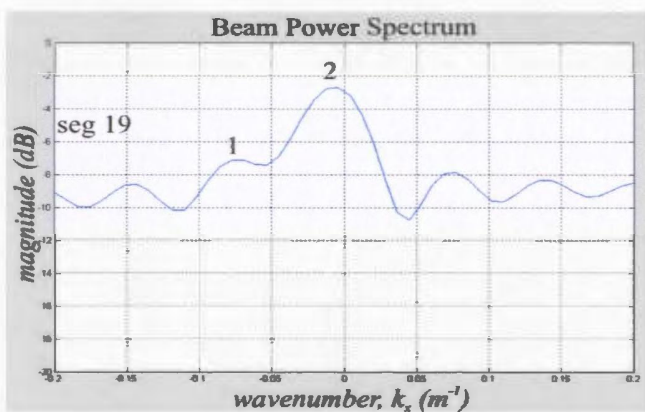
(*c*) The two wavefronts are also resolved in segment 19.
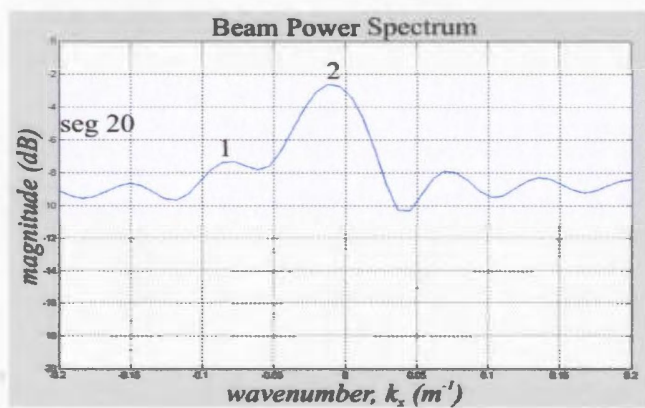
(*d*) The wavefronts are still resolved in segment 20.

The source was moved to a distance of 300 m from the first receiver and the experiment was repeated with the same program as above, but for convenience it was given a new name, *twoscatNC_rm*, with some few changes as shown in Appendix C. Figure 4.41 shows the beam power responses from all the segments. Two peaks appear at segments 17, 18, 19 and 20. This shows the presence of two waves impinging on the array. The beamformer has been able to identify two wavefronts approaching the array from different angles. This result indicates that the beamformer can only resolve the two waves if the source is not directly above the scatterers.

4.3 Summary

This chapter has assessed the performance of the conventional beamformer on a uniform linear array (ULA) in view of the background theory presented in chapters 1, 2, and 3.

A procedure for generating and preparing the data for the beamforming process was outlined in section 4.1. Synthetic seismic data were generated in Seismic Unix® by solving the scalar wave equation using a second order finite-difference method. The data were generated using a dominant frequency of 50 Hz which made it sufficiently narrowband for it to be processed using narrowband techniques discussed in chapters 2 and 3. Segmentation of the whole hyperbolic diffraction from the data sets generated was done in accordance with the planar wave criterion mentioned in section 2.1. After segmentation the data was then ready for beamforming.

Section 4.2 discusses the capability of the beamformer by evaluating a number of performance measures like angle estimation, how well it can locate one or more targets,

response of the array in the presence of noise and effect of decimating the data. Incidence angles corresponding to the mainlobe in each segment were obtained. These angles represented the direction vector for each segment and thus were back-projected to a common location which represented the probable location of the scatterer. The beamformers' ability to pinpoint the location of the target was shown in four model examples. In all the models, the intersection points of back-projected raypaths was a bit scattered and thus a distance-weighting scheme had to be used to reduce the errors introduced by points far away from the area of concentration. The results demonstrated that after using a distance-weighting scheme the beamformer could satisfactorily estimate the location of the scatterer to within a few meters of the actual location. It was also established from the results that as the source moves to the other end of the receiver array beamformer segments far away from the source lose resolution and cannot be relied on in determining the location of the scatterer.

The chapter has also shown that in a noise environment the beamformer performs well within its limitations. One striking observation is that the beamformer could not produce any meaningful results when the signal-to-noise ratio was less than 5. The signal-to-noise ratios (SNR's) used were the ones as defined in Seismic Unix®. Seismic Unix® computes the noise using the value of the absolute maximum for the dataset as a whole. A different software package may compute SNR's trace-by-trace.

The beamformer was also tested on decimated data, but the data had to be interpolated to have enough resolution for picking the angle of arrival of the wavefronts. The beamformer's performance was satisfactory within its limitations.

The beamformer's ability to locate two scatterers was assessed in 4.2.5. Two scatterers were placed more than a Fresnel zone apart with the source placed at two different locations, one at the middle of the receiver array and the other at 300 m away from the first receiver. The results indicate that the beamformer is only able to detect the two scatterers when the source is not at a point directly between them. The presence of the two scatterers was shown by two peaks in the array responses of a few segments of the diffraction hyperbola.

Chapter 5

Thesis Summary

5.1 Conclusions

An important issue in this thesis was the potential of using seismic beamforming to locate

mineral deposits in a cost-effective manner. The decision to use this technique follows

the idea that mineral deposits particularly massive sulfide bodies generate a characteristic

scattering response that could be detected and thus help in locating and imaging them.

Seismic beamforming works under the assumptions that arriving wavefronts are planar

on the scale of the array aperture and are generated by point sources. These assumptions

allow us to only use the arrival energy, which contains the wavenumber or angle of

incidence and amplitude, to locate a scatterer. The angles are back-projected to a

common point which represents the location of a point source or scatterer. The use of

both seismic beamforming and a small number of sources to generate the energy would

considerably reduce exploration costs for deeper targets.

After writing a beamforming algorithm, synthetic data for four different

geological models was generated using a finite-difference method of solving differential

equations. The 1-D beamformer's capability was assessed by looking at a number of

performance measures. These included the angle of arrival of impinging wavefronts on

the receiver array, effect of adding noise to the data, effect of decimating the data and the

presence of multiple targets. An investigation of the angles indicates the limitations of the

beamformer. After back-projecting arrival angles a distance-weighting scheme is

necessary to use to reduce errors introduced by intersection points that are far from their concentration area. Using the distance-weighting scheme enabled the beamformer to satisfactorily estimate the location of a scatterer. It was established that beamformer segments further away from the source lose resolution and these segments cannot be used for the investigations. A comprehensive study on noise effects reveals that the beamformer performs well on a data set, generated in Seismic Unix®, with a signal-to-noise ratio of at least 5. The noise generated had an uncorrelated Gaussian distribution and it was computed using the value of the absolute maximum of the data set. It was also shown that spatial decimation of the data has no adverse effect on location estimates. However, for the purpose of having enough beam steering resolution, the interpolated data had to have more spatial points in the beamformer. Performance of the beamformer in the presence of two scatterers separated by a distance more than a Fresnel zone apart was also demonstrated. The beamformer was not able to pick two scatterers in its vicinity when the source was at a point directly between them. But it was able to "see" the two scatterers when the source was moved to a point on the other side of one scatterer.

Finally, I can state that the objectives of the thesis have been realized under the limitations of the beamforming algorithm I used. Even though the beamformer was not very robust it has demonstrated that with a robust system the idea can work.

5.2 Recommendations

Future multi-dimensional beamformers can build on the results obtained using the 1-D array that was analyzed in this thesis. A few recommendations exist arising from the problems that were faced in the implementation of the beamformer.

The main issue that needs to be addressed before going further with the topic addressed by the thesis is the picking of incidence angles or wavenumbers where the mainlobe has the highest power. This aspect of the method is very crucial to obtaining any meaningful results. Handpicking the peaks is very tedious and for a very large data set may not be desirable. A source code could be developed to pick these angles automatically. However, one should ensure that the noise level is not too high to compromise this process. Unwanted noise and interfering signals could be filtered prior to beamforming using standard seismic filtering techniques.

A robust method other than conventional beamforming is possible to attain higher resolution and accuracy. These methods are extensively used in Sonar and Radar applications. Details of these other methods are discussed in Van Trees (2002). With these high-resolution methods 2-D and 3-D arrays can be explored.

References

[1] Arnold, M. E., 1977, Beam forming with vibrator arrays: *Geophysics*, vol. 42, no. 7, pp 1321-1338.

[2] Burdic, W. S., 1991, *Underwater acoustic system analysis*: Prentice-Hall, Inc.

[3] Cohen, J. K. and Stockwell, Jr. J. W., 1999, CWP/SU: Seismic UNIX Release 33: a free package for seismic research and processing, Center for Wave Phenomena, Colorado School of Mines.

[4] Dahle, A., Gjøystdal, H., Grammeltvedt, G., and Hansen, S. T., 1985, Application of seismic reflection methods for ore prospecting in crystalline rock: *First Break*, vol. 3, no. 2, pp 9-16.

[5] Dudgeon, D. E., and Mersereau, R. M., 1984, *Multidimensional digital signal processing*: Prentice-Hall, Inc.

[6] Eaton, D., Guest, S., Milkereit, B., Bléeker, W., Crick, D., Schmitt, D., and Salisbury, M., 1996, Seismic imaging of massive sulfide deposits, Part III: Borehole seismic imaging of near-vertical structures: *Economic Geology*, vol. 91, no. 5, pp 835-840.

[7] Eaton, D. W., 1999, Weak elastic-wave scattering from massive sulfide orebodies: *Geophysics*, vol. 64, no. 1, pp 289-299.

[8] Hampson, G., 1997, *Implementing multi-dimensional digital hardware beamformers*: Ph. D. thesis, Monash University.

[9] Johnson, D. H., 1982, The application of spectral estimation methods to bearing estimation problems: *Proceedings of the IEEE,* vol. 70, no. 9, pp 1018-1028.

[10] Johnson, D. H., and Dudgeon, D. E, 1993, *Array Signal Processing: Concepts and techniques:* PTR Prentice-Hall, Inc.

[11] Laletsang, K., 2001, *Seismic exploration for metallic mineral deposits*: Ph. D. thesis, Memorial University of Nfld.

[12] Manolakis, D. G., Ingle, V. K., and Kogon, S. M., 2000, *Statistical and Adaptive Signal Processing: Spectral estimation, signal modeling, adaptive filtering and array processing*: The McGraw-Hill Companies, Inc.

[13] Maranda, B., 1989, Efficient digital beamforming in the frequency domain: *J. Acoust. Soc. Am.,* vol. 86, no. 5, pp1813-1819.

[14] Milkereit, B., Eaton, D., Wu, J., Perron, G., Salisbury, M., Berrer, E. K., and

Morrison, G., 1996, Seismic imaging of massive sulfide deposits, Part II: Reflection seismic profiling: *Economic Geology*, vol. 91, no. 5, pp 829-834.

[15] Moran, M. L., and Albert, D. G., 1996, Source location and tracking capability of a small seismic array: US Army *CRREL* Report CR 96-8.

[16] Mucci, R. A., 1984, A comparison of efficient beamforming algorithms: *IEEE Transactions on Acoustics, Speech, and Signal Processing,* vol. ASSP-32, no. 3, pp 548-558.

[17] Nielsen, R. O., 1991, *Sonar Signal Processing*: Artech House, Inc.

[18] Robinson, E. A., and Treitel, S., 1980, *Geophysical Signal Analysis*: Printice-Hall.

[19] Salisbury, M. H., Milkereit, B., and Bléeker, W., 1996, Seismic imaging of massive sulfide deposits, Part I: Rock properties: *Economic Geology*, vol. 91, no. 5, pp 821-828.

[20] Sheriff, R. E., and Geldart, L. P., 1995, *Exploration Seismology*: Cambridge University Press.

[21] Stoica, P., and Moses, R. L., 1997, *Introduction to spectral analysis*: Printice-Hall.

[22] Telford, W. M., Geldard, L. P., and Sheriff, R. E., 1990, *Applied Geophysics*: Cambridge University Press.

[23] The MathWorks Inc., *MATLAB Version 5.3.1.29215a (R11.1)*, September 1999.

[24] Van Trees, H. L., 2002, *Optimum Array Processing: Part IV of Detection, estimation, and modulation theory*: John Wiley & Sons.

[25] Van Veen, B. D., and Buckley, K. M., 1988, Beamforming: A versatile approach to spatial filtering: *IEEE Acoustic, Speech, and Signal Processing Magazine,* pp. 4-24, April.

[26] White, D., 1999, The basic principles of seismic reflection methods for mineral exploration, *in* Lowe, C., Thomas, M.D. and Morris, W.A., eds., *Geophysics in Mineral Exploration: Fundamentals and Case Histories*: Geological Association of Canada, Short Course Notes, v. 14, pp 163-176.

[27] Wright, C., Wright, J. A., and Hall, J., 1994, Seismic reflection techniques for base metal exploration in eastern Canada: examples from Buchans, Newfoundland: *Journal of Applied Geophysics*, vol. 32, pp 105-116.

[28] Yilmaz, O., 2001, *Seismic Data Analysis: processing, inversion, and interpretation of seismic data*: Society of Exploration Geophysicists.

Appendices

The appendices' section contains the source code for all the figures generated in the text using MATLAB® (Matrix Laboratory). The codes for illustrating Rayleigh resolution and grating lobes are given, as well as the main source code for the thesis. Minor changes to the main code that help us achieve the objectives of the thesis are also shown in the last appendix.

Appendix A

Illustration of Rayleigh Resolution and Grating Lobes

A1. The following code was used to generate the diagrams in figure 3.4.

rayleigh_res.m

```
%%%%%%%%%%%%%%%%%%%%%%%%%%%%%%%%%%%%%%%%%%%%%%%%%%%%%%%%%%%%%%%%%%%%%%%%%%%%%%
%                 Uniform Linear Array (ULA) - RAYLEIGH RESOLUTION          %
%                    © Lucky Moffat, 07/01/2004                            %
%%%%%%%%%%%%%%%%%%%%%%%%%%%%%%%%%%%%%%%%%%%%%%%%%%%%%%%%%%%%%%%%%%%%%%%%%%%%%%

clear all
home

f = 50;                              %waveform dominant frequency in Hz
D = 20;                              %receiver separation in meters should be < 40m
M = 40;                              %number of receivers
m = 0:M-1;                           %vector of indexes
c = 4000;                            %propagation velocity

k = (2*pi*f)/c;                      %wavenumber of the plane wave from the source
dir1 = input('Enter the first angle in the range -90:90.   '); %angle of arrival of 1st
wave
stheta_o1 = sin(dir1*pi/180);        %sine of angle of the 1st wave

dir2 = input('Enter the second angle in the range -90:90.   '); %angle of arrival of 2nd
wave
stheta_o2 = sin(dir2*pi/180);        %sine of angle of the 2nd wave


%a_m = ones(M,1);                     %rectangular window
a_m = 0.5 - 0.5*cos(2*pi*m/M);       %hanning window

stheta = sin((-90:90)*pi/180);       %search space

for v = 1:length(stheta)

   y1 = exp(i*k*m*D*(stheta(v)-stheta_o1));  %normalized array response of 1st wave
   y2 = exp(i*k*m*D*(stheta(v)-stheta_o2));  %normalized array response of 2nd wave
   Y = y1+y2;                        %application of the linear superposition principle

   bp(v) = abs(Y*a_m');              %absolute value of weighted array response
```

```
end

bpower = real(20*log10(bp/max(bp))); %beam power

plot(asin(stheta)*180/pi,bp./max(max(bp))), xlabel('\it incidence angle (degrees)'), ...
   ylabel('\it amplitude'), title('Rayleigh Resolution','Fontsize', 14)%plot of Magnitude
versus angle
%subplot(2,1,1),plot(asin(stheta)*180/pi,bp./max(max(bp))), xlabel('\it incidence angle
(degrees)'), ...
%   ylabel('\it normalized amplitude'), title('Rayleigh Resolution','Fontsize', 14) %plot
of Magnitude versus angle
grid;
%subplot(2,1,2),plot(asin(stheta)*180/pi,bpower), xlabel('\it incidence angle
(degrees)'), ...
%   ylabel('\it amplitude in dB')  %plot of Power versus angle
%grid;
```

A2. The following code was used to generate figure 3.5 which gives an illustration of Grating Lobes.

grat_lbs.m

```
%%%%%%%%%%%%%%%%%%%%%%%%%%%%%%%%%%%%%%%%%%%%%%%%%%%%%%%%%%%%%%%%%%%%%%%%%%%%%%%
%        Uniform Linear Array (ULA) - Illustration of GRATING LOBES        %
%                    © Lucky Moffat, 07/01/2004                           %
%%%%%%%%%%%%%%%%%%%%%%%%%%%%%%%%%%%%%%%%%%%%%%%%%%%%%%%%%%%%%%%%%%%%%%%%%%%%%%%

clear all
home

f = 50;                     %waveform frequency in Hz
d = [20,40,80,160];         %receiver separation in meters

%--------to avoid aliasing completely d should be <= 40m (i.e. the condition
%f <= (0.5 * c)/d should be satisfied)

M = [40,20,10,5];           %number of receivers in the array
c = 4000;                   %acoustic speed

k = (2*pi*f)/c;             %wavenumber of the plane wave from the source
dir = input('Enter theta in the range -90:90.   '); %direction of incident wavefront
stheta_o = sin(dir*pi/180); %sine of direction of incident wavefront

for i = 1:length(d)

    a_m = ones(M(i),1);     %rectangular window
    m = 0:M(i)-1;           %vector of indexes

    stheta = sin((-90:90)*pi/180); %sine of rotational direction

    for v = 1:length(stheta) %for each input direction calculate filter response

        Y = exp(j*k*m*d(i)*(stheta(v)-stheta_o)); %output of the beamformer
        bp(v) = abs(Y*a_m); %beam pattern

    end;

    bpower = real(20*log10(bp/max(bp))); %calculate beampower
    subplot(4,1,i),plot(asin(stheta)*180/pi,bp), title('Beam Pattern')
    grid;

end;
```

Note - The above script assumes the direction of propagation is known. Thus, it gives the user the option of selecting a preferred direction.

Appendix B

The Main Program

This appendix gives the main source code of the thesis which implements equation 14.

The source code is explained in section 3.2.

center_css.m

```
%%%%%%%%%%%%%%%%%%%%%%%%%%%%%%%%%%%%%%%%%%%%%%%%%%%%%%%%%%%%%%%%%%%%%%%%%%%%%%%%
%          Conventional beamforming for a Uniform Linear Array (ULA) of Seismic data          %
%                         © Lucky Moffat, 07/01/2004                                          %
%%%%%%%%%%%%%%%%%%%%%%%%%%%%%%%%%%%%%%%%%%%%%%%%%%%%%%%%%%%%%%%%%%%%%%%%%%%%%%%%
% Note - The program beamforms the whole diffraction curve

clear all
home

% ---------------------------INPUT DATA INFO -------------------------

rows = 700;                      % Number of time samples
cols = 1000;                     % Number of traces
sr = .0005;                      % Sample rate in seconds

% --------------------- PARAMETERS FOR WINDOWING ----------------------

t0 = 338;                        % time (in samples) of diffraction apex
aloc = 1;                        % trace # that locates the diffraction apex
seglen = 50;                     % segment length in meters
startwin = 100;                  % start of window in samples before theoretical
wsamps = 200;                    % length of window in samples
thevel = 4000;                   % aver. Vel. for calculation of theoretical
                                 %   diffraction hyperbola (m/s)
tracespace = 1;                  % trace spacing (m)

% --------------------- Some Calculations ------------------------------
t0t = t0*sr;                     % time of diffraction apex in seconds
seglens = seglen/tracespace;     % segment length in samples
numsegs = round(cols/seglens)    % number of segments
% ------------------------------------------------------------------

% ------------------------ GET THE DATA --------------------------------

fid = fopen('singscat_Oct11rm.bin');
[A,count] = fread(fid,[rows,cols],'float32');
count

% ------------- CALCULATE THE THEORETICAL DIFFRACTION MOVEOUT -----------

xb = 0;                          % x-value where the hyperbola begins
xo = 500;                        % x-value at normal incidence
```

```
x = xb-xo;                           % pre-allocate x

% ---- Compute diffraction moveout in samples
for i = 1:cols
    Dt(i) = t0+(t0t + (x*x)/(2*thevel*((thevel*t0t)/2)))/sr); % coincident source
                                                              % and scatterer
    x = x+tracespace;
end

% ------------------------- CALCULATE THE WINDOW ----------------------

% Top of window
segkount = 1;
kount = 1;

% ---- for each segment
while segkount < cols
    Ws(kount) = round(Dt(segkount)-startwin); % Start of window for each segment
    segkount = segkount+seglens;

    kount = kount+1;
end

trace = 1;

% ---- For each trace in a segment
for n = 1:numsegs
    for c = 1:seglens
        wtop(trace) = Ws(n);      % Start of the window for each trace in each segment
        trace = trace+1;
    end
end

% Bottom of the window for each trace
for t = 1:trace-1
    wbot(t) = wtop(t)+wsamps;
end

% ------------------------- APPLY THE WINDOW -------------------------

kountsamp = 1;
kountrace = 1;

for n = 1:numsegs
   for c = 1:seglens              % col
          b = wtop(kountrace);
        for k = 1:wsamps          % row
            W(k,c) = A(b,kountrace);
            kountsamp = kountsamp+1;
            b = b+1;
        end
        kountsamp = 1;
        kountrace = kountrace+1;
   end

%------------------------- BEAMFORM EACH SEGMENT ----------------------
    M = mean(mean(W));          % mean of each segment
    W = W - M;                  % bring signal to zero mean

    X = fft(W).';               % spectrum of each segment
 %X = X(:,1:wsamps/2);          % single sided spectrum

  K = zeros(seglens,1);         % initialize wavenumber vector

      for p = 1:seglens         % for every receiver


      kx = (-0.2+0.4*(p-1)/(seglens-1)); % trial wavenumbers

      a = exp((j*kx*tracespace*[0:seglens-1].'*[0:wsamps-1])/wsamps);   % ARF
```

106

```
    Y_k = X.*a;                % beam response, Y(k), in fourier domain
    %Y_n = abs(ifft(Y_k));     % beam response, Y(n), in the time domain

    B(p,:) = sum(Y_k.^2);      % average power value of the beam

    K(p) = kx;

  end

  bpower = real(10*log(bp/max(bp))); % beam power in dB

  subplot(5,4,n), plot(K,bpower)
  %title('Beam Power Spectrum'), ylabel('magnitude (dB)'), xlabel('wavenumber (kx)')
  axis([-0.2 0.2 -0.2 0])
  grid;

  if n <= (numsegs-1)
      disp('PRESS ANY KEY to go to the next segment')
       pause
  else
      disp('All segments exhausted, thank you!')
  end

end

%------------------------------ END OF PROGRAM --------------------------
```

Appendix C

Changes to the Main Program

C1. The following are changes made to *center_css.m* to create a new program

soffset_nc.m that implements the investigation in example **b** of section 4.2.2.

```
                      .
                      .
                      .
      -- rows = 696;     % number of time samples

      -- t0 = 390;       % time in samples of diffraction apex

      -- seglen = 50;    % segment length in meters

      -- wsamps = 100;   % length of window in samples

                      .
                      .
                      .
```

C2. The following are changes made to *center_css.m* to create a new program *end_css.m* that implements the investigation in example **c** of section 4.2.2.

```
                              .
                              .
                              .

    -- rows = 1100;    % number of time samples

    -- t0 = 342;       % time in samples of diffraction apex

    -- wsamps = 150; % length of window in samples

                              .
                              .
                              .
```

C3. The following are changes made to *center_css.m* to create a new program *scenter_nc.m* that implements the investigation in example **d** of section 4.2.2.

```
                              .
                              .
                              .

    -- rows = 1100;    % number of time samples

    -- t0 = 480;       % time in samples of diffraction apex

    -- wsamps = 150; % length of window in samples

                              .
                              .
                              .
```

C4. The following excerpt is from the program, *center_cssDecF10.m* that implements the decimation process explained in section 4.2.4 of chapter 4. The program is similar to the main one except for the addition of the interpolation process and the use of decimated data input.

```
                              .
                              .
                              .

% ------------------------- GET THE DATA ----------------------------
fid=fopen('singscat_Oct11rm_wind10.bin');
[A,count] = fread(fid,[rows,cols],'float32');
count;

A1 = interpft(A,1000,2);        % interpolation
A = A1;

% ------------- CALCULATE THE THEORETICAL DIFFRACTION MOVEOUT -----------
                              .
                              .
                              .
```

C5. Changes made to the main program to investigate the response of the beamformer to two scatterers. The following changes were made to create a new program called *twoscat_rm.m*:

```
                       .
                       .
                       .
-- t0 = 370;          % time in samples of diffraction apex

-- wsamps = 260;      % length of window in samples

-- startwin = 130;    % start of window in samples before theoretical

-- ps = 0;            % x-position of source from scatterers (coordinates: 500.5,0)

-- xo = 480;          % x-value at the apex of the hyperbola
                       .
                       .
                       .
-- Dt(i)= t0+((x*x)/(2*thevel*(t0t*thevel/2))+ps*(ps-
        x)/(thevel*(t0t*thevel/2)))/sr; % source not coincident (refer to eqn. 19)
                       .
                       .
                       .
```

Changes made to *twoscat_rm.m* to create a new program called *twoscatNC_rm.m*:

```
                       .
                       .
                       .
-- t0 = 350;          % time in samples of diffraction apex

-- wsamps = 350;      % length of window in samples

-- startwin = 175;    % start of window in samples before theoretical

-- ps = 50;           % x-position of source from scatterers (coordinates: 350,0)

-- xo = 420;          % x-value at the apex of the hyperbola
                       .
                       .
                       .
```